Electronic Theses and Dissertations

Theses, Dissertations, and Major Papers

10-30-2020

Wear of Bainite-transformed AISI 1045 Steel in Comparison with Nitriding and Boriding Treatments

Mingxiao Yang
University of Windsor

Follow this and additional works at: https://scholar.uwindsor.ca/etd

Wear of Bainite-transformed AISI 1045 Steel in Comparison with Nitriding and Boriding Treatments

By

Mingxiao Yang

A Thesis

Submitted to the Faculty of Graduate Studies
through the Department of Mechanical, Automotive & Materials Engineering
in Partial Fulfillment of the Requirements for
the Degree of Master of Applied Science
at the University of Windsor

Windsor, Ontario, Canada

2020

© 2020 Mingxiao Yang

Wear of Bainite-transformed AISI 1045 Steel in Comparison with Nitriding and Boriding Treatments

by

Mingxiao Yang

APPROVED BY:

_____
O. Jianu
Department of Mechanical, Automotive & Materials Engineering

_____
D. Green
Department of Mechanical, Automotive & Materials Engineering

_____
A. Alpas, Advisor
Department of Mechanical, Automotive & Materials Engineering

September 10, 2020

DECLARATION OF ORIGINALITY

I hereby certify that I am the sole author of this thesis and that no part of this thesis has been published or submitted for publication.

I certify that, to the best of my knowledge, my thesis does not infringe upon anyone's copyright nor violate any proprietary rights and that any ideas, techniques, quotations, or any other material from the work of other people included in my thesis, published or otherwise, are fully acknowledged in accordance with the standard referencing practices. Furthermore, to the extent that I have included copyrighted material that surpasses the bounds of fair dealing within the meaning of the Canada Copyright Act, I certify that I have obtained a written permission from the copyright owner(s) to include such material(s) in my thesis and have included copies of such copyright clearances to my appendix.

I declare that this is a true copy of my thesis, including any final revisions, as approved by my thesis committee and the Graduate Studies office, and that this thesis has not been submitted for a higher degree to any other University or Institution.

ABSTRACT

The purpose of this work is to develop a bainitic heat treatment procedure for wear reduction in a medium carbon steel and compare the efficiency of this heat treatment with gas nitriding or electrochemical boriding surface treatments.

Heat treatments were conducted on AISI 1045 steel blocks taken from an automotive component, namely an overrunning alternator decoupler (OAD) pulley bore using an induction heater. The samples were quenched in different quenching media of oil, melt salt and water. The hardness and microstructural transformation results were represented with cooling curves superimposed on the Continuous Cooling Transformation (CCT) diagram of the 1045 steel. The heat treated results indicate 820 °C induction heating for 2 minutes followed by 160 °C oil quenching for 15 seconds resulted in the lower bainitic and martensitic structures and the highest bainite percentage (~19.5 %). The sliding wear test was conducted with block-on-ring tribometer under dry, lubricated and humidity conditions. Volumetric wear loss was measured and calculated at different sliding distances. The relationship between the volumetric loss and working conditions showed that induction hardened steel followed by 160 °C oil quenching resulted in the lowest wear rate in both dry and lubricated condition due to the higher hardness and toughness of bainitic and martensitic structures compared to the untreated, nitrided and borided 1045 steel. In addition, it was found that the gas nitriding process produced the lowest surface roughness (0.35 - 0.37 μm) and the electrochemical boriding process produced the highest surface microhardness (1100 - 1300HV). The boric acid film was formed on the surface of borided steel after the SAP process (annealing at 750 °C followed by cooling in 40 % RH environment). It can be considered as a self-lubricated film to make the surface withstand sliding wear damage.

DEDICATION

To my beloved father and mother

ACKNOWLEDGEMENTS

Firstly, I would like to express my heartfelt gratitude to my supervisor Dr. A.T. Alpas for his enlightening guidance and valuable advice through the entire study process. Without his great patience and constant encouragement, the accomplishment of this thesis wouldn't have been possible. I am also deeply impressed by his strong sense of responsibility and professional dedication, which has not only taught me how to do academic research but also set a good example for my future work.

Secondly, I would appreciate that Dr. D.E. Green, and Dr. O.A. Jianu are willing to advise and guide this research. My special thanks to Dr. A. Abougharam and Mr. S. Bagherpour from Litens Automotive Group for providing the supports and insightful discussions that improved the industrial relevance of the research work. I am also grateful to Dr. G.K. Sireli from Istanbul Technical University for the boriding process and helpful suggestions.

Furthermore, I would like to thank all the researchers in the Tribology of Materials Research Center, especially Dr. M. Lou, Dr. G. Sun, Dr. Z. Yang and Mr. Z. Cui for their much appreciated support and help. Also, I wish to express thanks to Ms. S. Lackie from Great Lakes Institute for Environmental Research for her help in operating the SEM.

In the end, thank my family's support that makes the finish of this study possible.

TABLE OF CONTENTS

LIST OF TABLES

LIST OF FIGURES

LIST OF ABBREVIATIONS/SYMBOLS

OAD	Overrunning alternator decoupler
CL	Compound Layer
DZ	Diffusion Zone
WTW	Wear Track Width
WTD	Wear Track Depth
HV	Vickers Hardness
ASTM	American Society for Testing and Materials
ASM	American Society for Metals
AISI	American Iron and Steel Institute
OM	Optical Microscopy
SEM	Scanning Electron Microscopy
XRD	X-Ray Diffraction
EDS	Energy Dispersive X-ray Spectroscopy
CCR	Critical cooling rate
CCT	Continuous cooling transformation
TTT	Time-Temperature-Transformation
Ms	Martensite start temperature
Mf	Martensite finish temperature

Bs	Bainite start temperature
Bf	Bainite finish temperature
UB	Upper bainite
LB	Lower bainite
SAP	Short anneal process

CHAPTER 1

INTRODUCTION

As automotive industry's growing demand for better materials used in transmission applications, the carbon steels have been developed for better mechanical properties such as higher strength, more ductility etc. [1]. Based on the carbon percentages, there are three categories are divided from carbon steel used in automotive industry: low carbon ($C < 0.3\%$), medium carbon ($0.3\% < C < 0.6\%$) and high carbon steel ($C > 0.6\%$). Medium carbon steels are capable of being heat treating to improve the mechanical properties such as ductility, toughness, strength, hardness and tensile strength to meet a particular design purpose. Also the microstructures can be refined by quenching or tempering for developed toughness with good strength [1]. The components produced by the medium carbon steel such as cylinders, fly-wheels, crankshafts, gears, and camshafts due to the ductility and increased strength as well as improved tribological performance [2].

1.1 Motivation

AISI 1045 steel is a steel grade used for the body of overrunning alternator decoupler (OAD) pulley bore, which is a unique engine belt drive tuning device. AISI 1045 steel is preferred because of its global availability, ease of machinability and its ability to be flame or hot rolled or induction hardened condition to increase the hardness and wear resistance. However, in the automotive application, the sliding motion may occur between the two components produced by medium carbon 1045 steel and the ASTM A228 high carbon steel. ASTM A228 steel is most commonly used in a wide range of applications in terms of extension, helical compression and torsion springs, particularly in the finer wire diameters due to its ability to withstand high stresses under repeated loadings, high tensile strength, high hardness and elastic limit among wrought carbon steels. It is found that the ASTM A228 steel exhibits better wear performance and higher harness that lead to longer service life in the automotive application compared to AISI 1045 steel. Therefore, study is required to improve the ability of the 1045 steel to withstand sliding wear for matching the performance requirements of the surface properties in the automotive industry. It is

important to give the desired surface treatment procedures on the 1045 steel to improve the mechanical and tribological properties.

Currently, gas nitriding [3] is being applied to medium carbon steel to increase its wear resistance in this application. The process of gas nitriding is achieved by saturating the steel parts surface with available nitrogen (free nitrogen atoms) at the nitriding temperature. However, the industrial application of the gas nitriding process requires an additional handling and processing step which adds cost and time to the manufacturing process. Thus the development of a more cost-effective process for hardening the surface of 1045 steel particularly a bainitic heat treatment was envisaged.

The objective of heat treating 1045 carbon steel is to change the mechanical properties of steel, namely to increase its hardness, yield strength, without reducing its impact resistance and ductility. Induction surface hardening is a typical heat treatment method where only selected part or a working surface layer of the steel element is heated inductively and then immediately cooled by merging into a quenching medium, while the remaining parts of steel are practically not treated. The possible microstructures include lamellar pearlite, bainite, retained austenite and martensite phases can be obtained by induction hardened steel. Steels with pearlite offer high ductility but its strength is too low for some applications; steels with martensite offer good strength and hardness but tend to be too brittle. The steels with bainite can offer both the advantages of pearlite and martensite, in terms of higher strength, better ductility, good corrosion resistance, superior wear resistance, higher impact toughness, longer fatigue life, etc. The induction hardened steel can be introduced to improve the mechanical hardness, as well as wear resistance as required for particular applications with a combination of refined microstructures [4-5].

In addition, the thermochemical diffusion process called electrochemical boriding, which is similar to the gas nitriding process that is used to harden the surface of steel, has aroused a lot of interest according to numerous studies. The boride layer that is formed on the top surface due to the diffused boron atoms into the surface enhances the surface properties such as hardness and wear resistance of steel. Therefore, three surface

treatments, gas nitriding, electrochemical boriding and heat treated bainitic process will be applied to the 1045 steel to make the comparison of hardness and wear performance.

1.2 Research scope

The methodology of this study comprises of developing a bainitic transformed 1045 steel. The mechanical properties of the samples with different bainite percentages were measured and the heat treatment procedure that provided a high hardness along with good resistance to crack formation during the quenching stage of the heat treatment was selected for sample preparation used in tribological tests. These tests were conducted using a block-on ring tribometer under dry and lubricated sliding conditions and the results were compared with the same grade of steel subjected to the boronizing and gas nitriding treatments.

The study begins with a critical assessment of the literature review on carbon steel, induction hardening, microstructures transformed and sliding wear of steels. Chapter 2, describes the general understanding of the mechanism and transformation during heat treatment and wear mechanisms of steel including influences of temperature and environment. The principles of electrochemical boriding (boronizing) process were summarized as well.

The induction hardening and sliding wear experiments and detailed characterization procedures carried out thereafter to understand the mechanisms of wear in various bainitic and martensitic structures are described in Chapter 3. The results of the induction hardening followed by three different quenching media are presented in Chapter 4. In this chapter, the Continuous cooling transformation diagrams(CCT) diagram of 1045 steel is combined with continuous cooling curves along with surface hardness and the microstructures of steel. Chapter 5 discusses the results of the sliding wear experiments performed to investigate the tribolayer formation and wear mechanisms. The conclusions and recommendations for future work are presented in Chapter 6 and Chapter 7, respectively.

CHAPTER 2

LITERATURE SURVEY

2.1 Carbon steel

2.1.1 Definition and classification of carbon steel

Carbon steel can be classified into three categories according to its carbon content: low-carbon steel (or mild-carbon steel), medium-carbon steel and high-carbon steel [6]. Their carbon content and properties compare as follows [7-11]:

- Low-carbon steels that contain up to 0.30% C are usually relatively soft and have low strength. However, they have high ductility, making them excellent for machining, welding and low cost applications, and the hardness of the metal's surface can be improved by carburizing, a heat-treatment process. They cannot be hardened by martensitic phase transformation but this is usually achieved by cold work. Low carbon steel is usually made into flat-rolled sheets and strips, used for shipbuilding, wire, vehicle bodies and domestic appliances. It's widely used for fabrication and paneling because it can't be altered by heat treatment. Carbon steel with the lowest possible amount of carbon is called 'wrought iron', used for fencing, gates and railings, hard but not brittle.

- Medium-carbon steels are similar to low-carbon steels except that the carbon ranges from 0.30 to 0.60% and the manganese from 0.60 to 1.65%. Increasing the carbon content to approximately 0.5% with an accompanying increase in manganese allows medium carbon steels to be improved via heat treatment involving austenitizing followed by quenching and tempering, giving them bainitic and martensitic microstructures. The uses of medium carbon-manganese steels include shafts, axles, gears, crankshafts, rails, couplings and forgings.

- High-carbon steels also called tool steel, contain from 0.60 to 1.25% C with manganese contents ranging from 0.30 to 0.90%. They have the highest hardness and toughness of the carbon steels and the lowest ductility. High-carbon steels are very wear-resistant as a result of the fact that they are almost always hardened and

tempered. High carbon steel has a much better tensile strength, used to make cutting tools, blades, punches, dies, springs and high-strength wire.

- Ultrahigh-carbon steels are experimental alloys containing 1.25 to 2.0% C. These steels are thermomechanically processed to produce microstructures that consist of ultrafine, equiaxed grains of spherical, discontinuous proeutectoid carbide particles.

In addition, based on the iron-carbon phase diagram relevant to steels has a eutectoid point at 0.77% carbon content, and the steels are also classified by carbon content as hypoeutectoid (less than 0.77 wt% C) steel, eutectoid steel and hypereutectoid (more than 0.77 wt% C) steel. Their microstructures are different due to the difference in carbon content. Eutectoid steel consists of just the lamellar-pearlitic structure whereas hypoeutectoid steel has additionally ferrite, and hypereutectoid steel contains small grains (larger than the pearlite lamella) of cementite [6].

2.1.2 Carbon steel in automotive

The steels used in automotive applications should be easy to machine and wear resistant at the same time. To some extent these two requirements contradict each other thus a machinable steel will be selected and then hardened or surface treated to achieve the wear resistance required. In addition to these two requirements, dimensional changes should not exceed the design tolerances after treatment [12]. Accordingly, medium carbon steel used in the overrunning alternator decoupler studied in this work was selected for its global availability, machinability and its ability to be flame or induction hardened in the normalized or hot rolled condition to improve the surface hardness and wear resistance.

2.2 *Wear in the transmission* system of automotive

2.2.1 Overrunning alternator decoupler OAD in engine belt drive system

In modern internal combustion engines, the mechanical power is transmitted by the belt drive system, which consists of the assembly of one or more belt(s) with pulleys that

transmit mechanical power to accessories such as alternators, pumps, tensioner, etc. Technically the rotor of alternator has been mechanically linked together with the driving belt; which turns the alternator pulley and the rotor is bolted directly to the pulley.
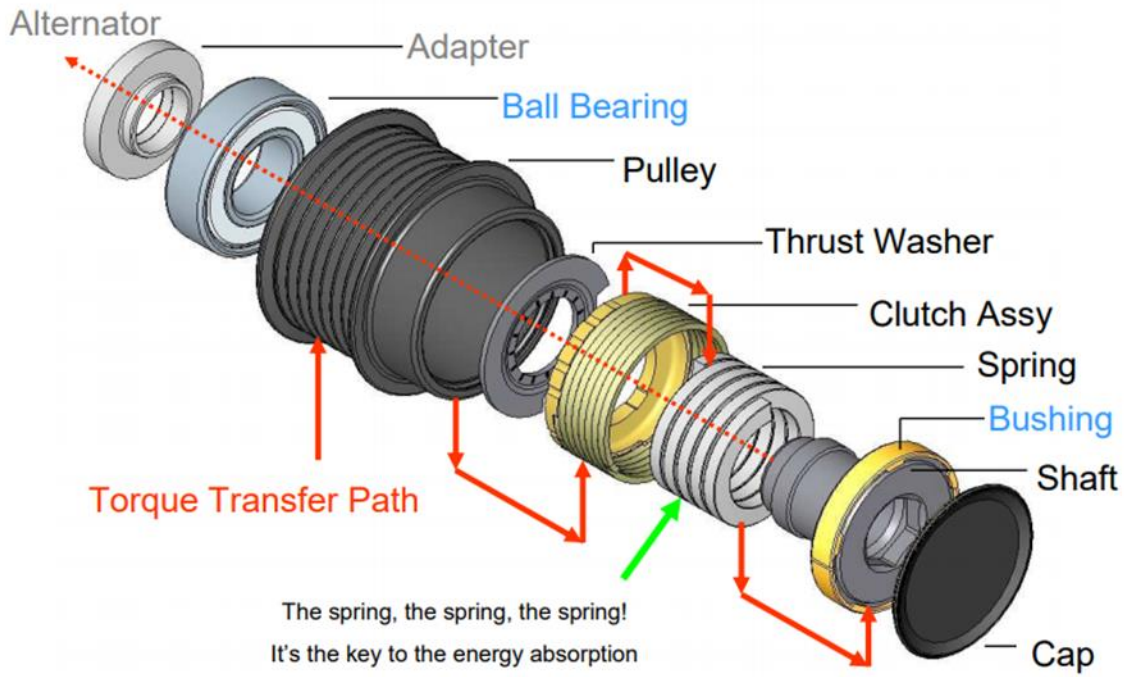
Figure 2.1. Schematic diagram of a typical OAD highlighting the major components including the bearing, pulley, clutch assembly, spring, thrust washer and bushing. Courtesy of Litens Automotive Group, Toronto, Ontario Canada.

The overrunning alternator decoupler (OAD) is a drive tuning device in an engine belt drive system that enables one direction rotation of the alternator. The OAD sits on the end of an alternator as a drive pulley, which fits on the rotor shaft. It will drive the alternator via the belt, freewheeling the alternator during engine deceleration. As shown in Figure 2.1, the OAD has a traditional drive belt pulley on the outside, but inside it has a one-way clutch and an absorber spring. A one-way clutch is often called an overrunning clutch, which locks up in one direction and freewheels in the opposite direction. Thus, the OAD's overrunning clutch locks up in the direction of normal alternator rotation, enabling the drive belt to spin the rotor. It also lets the rotor freewheel during sudden engine deceleration so the rotor will not drive the belt in the opposite direction. Freewheeling the rotor during

engine deceleration eliminates those belt-related issues such as slippage, wear and noise. Besides addressing these drive belt symptoms, an OAD may also improve engine efficiency.

2.2.2 Wear of OAD

Sliding wear is the progressive loss of material that results from two materials sliding against each other at the contact area under load. Sliding motion between the inner face of pulley bore and the clutch wire in OAD may cause severe mechanical wear and material transfer at the contact surfaces as shown in Figure 2.2, which may lead to reduced production efficiency, machine performance or even damage to the machine. For example, if the one-way clutch fails, the alternator pulley will freewheel in both directions, accompanying a no-charge condition and a dead battery.

(a)	(b)

Figure 2.2 Components of OAD, (a) pulley bore (Inner face made of medium carbon AISI 1045 steel), (b) clutch assembly (Clutch wire made of high carbon ASTM A228 steel).

The wear behaviour of steel is related to its microstructure, hardness and mechanical properties. While the pulley bore is made of medium carbon steel (AISI 1045 steel), and the clutch wire is made of high carbon steel (ASTM A228). According to the introduction in 2.1.1, the steel that contains higher percentage of carbon leads to better wear resistance and higher hardness compared with the medium carbon steel. In order to

improve the surface hardness and wear resistance of the pulley bore, different protective coatings and surface treatments are used in the AISI 1045 steel. Since the material surface controls the service life in many applications, a push for a more robust solution for increasing the surface properties while reducing the processing time would give automotive manufacturers an opportunity to reduce costs and production time.

2.2.3 Wear of 1045 steel

As AISI 1045 steel is commonly used in different industrial applications because of the wide range of mechanical properties, its wear performance of the material is still a unique challenge to be solved The wear mechanism of 1045 steel also involves adhesion, oxidation, plastic flow of material, strain hardening, generation of surface, sub-surface cracks and associated structural changes. The wear behaviour of 1045 steel was studied by many researchers according to its microstructure, hardness and mechanical properties, and a suitable surface modification is the main factor that contributes to improving tribological properties [149].

Odusote et al [150] investigated the effect of different quenching media on the mechanical properties of the medium carbon steel. The results indicated that water quenching resulted in increased tensile strength (852 MPa) and hardness (38 HRC) in comparison with the Palm oil (834 MPa and 34 HRC). Ikubanni et al [151] quenched the medium carbon steel in used engine oil, pap water and coconut water for improving the mechanical properties. It was observed that the surface hardness was greatly improved to 58 HRC by heating to 790° C and quenching in pap water, also the yield and ultimate tensile strength was better than the steel in the normalized condition. Karimbaev et al. [152] conducted the ultrasonic nanocrystal surface modification (UNSM) treatment on AISI 1045 steel in order to improve the tribological and mechanical characteristics, and the wear rate showed a reduction of about 11%.

8

2.3 Surface treatment for processing carbon steel

2.3.1 Gas nitriding

Nitriding is commonly used as a surface treatment to improve hardness, wear and corrosion resistance. Nitriding is processed in three environments, gas, liquid and plasma to produce a compound layer on top and diffusion zone beneath that. Currently gas nitriding [3] is being applied to medium carbon steel to increase the wear resistance and hardness because of the formation of nitride layers and the nitrogen following diffused into the material [14]. Gas nitriding consists of saturating the steel parts surface with nitrogen (free nitrogen atoms) at the nitriding temperature. The reaction of NH_3 disassociates into nitrogen (N) and hydrogen (H) happens when ammonia flows into the heated furnace:

$$2NH_3 \text{ (g)} \rightarrow N_2 \text{ (g)} + 3H_2 \text{ (g)}.$$
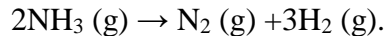
The nitride layer and following diffusion zone was created by nitrogen diffusing into the surface of the heated workpiece. Figure 2.3 shows the schematic cross-section of nitrided region which consists of a compound layer (CL) on the top and a diffusion zone (DZ) [15]. The compound layer is also called the white layer due to its color under the microscope after polishing and etching. This layer consists normally of γ' (Fe_4N) and ε ($Fe_{2-3}N$) intermetallics (apart from nitrides of alloying elements). In the subsurface region, the diffusion zone consists of needles of γ'-Fe_4N and α-Fe, due to the long-distance diffusion of nitrogen from the surface toward the core, which creates nitrogen gradients and higher hardness. Improvement of the wear resistance and corrosion resistance are generally owing to the compound layer, however, good fatigue resistance is ascribed to the diffusion zone [16]. However, the industrial application of gas nitriding process requires an additional handling and processing step which adds cost and time to the manufacturing process.
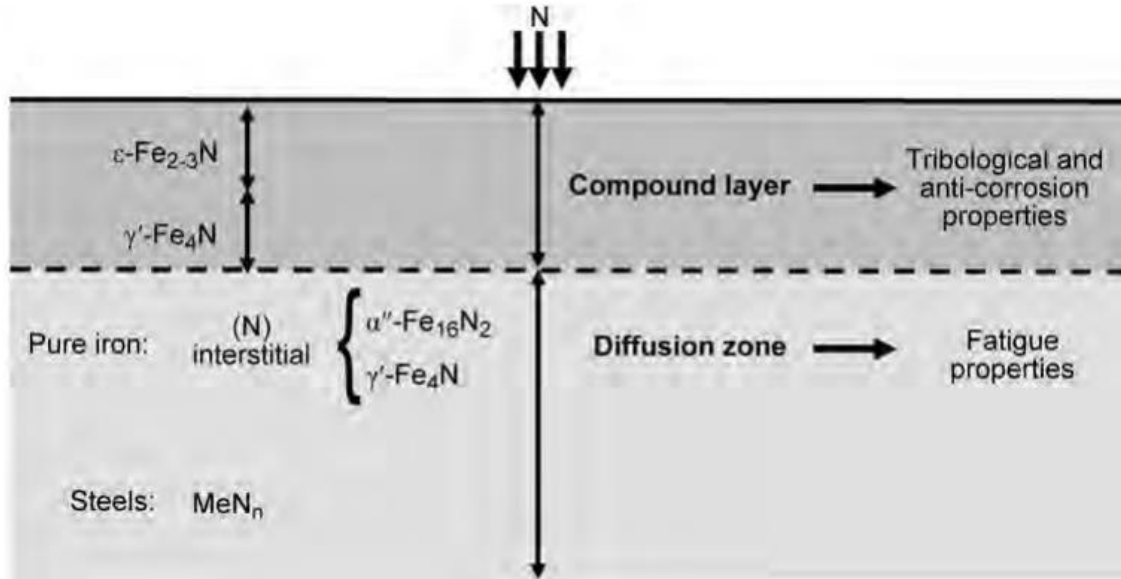
Figure 2.3 Schematic cross section of nitrided region of an iron-base ferritic specimen/component showing the compound layer and the diffusion zone with their (possible) constituents [15].

Applying nitriding process to the surface can both improve the hardness and the smoothness to the surface which leads to the reduction of wear and friction. The tribological behavior of nitrided steel was studied by various researchers who reported the nitriding process could improve wear performance (Burakowskietal., 1987; Karamis, 1991; and Bell and Sun, 1990). Podgornik et al. [153] observed that the nitriding process conducted at 5400 °C and in nitrogen-rich environment (75%H_2 - 25%N_2 gas mixture) led to the minors wear due to the improved substrate hardness and higher coating–substrate adhesion [154].

Kato et al. [155] established the wear map of gas nitrided 905M39, BS970, (EN41B) steel using a pin-on-disc tribometer under unlubricated conditions to determine the main regimes of the wear mechanism as shown in Figure 2.4. Only two essential wear regimes were identified, i.e. mild (oxidative) wear and severe(metallic) wear, and the mild wear region toward higher loads and sliding speeds was also extended by the gas nitriding.
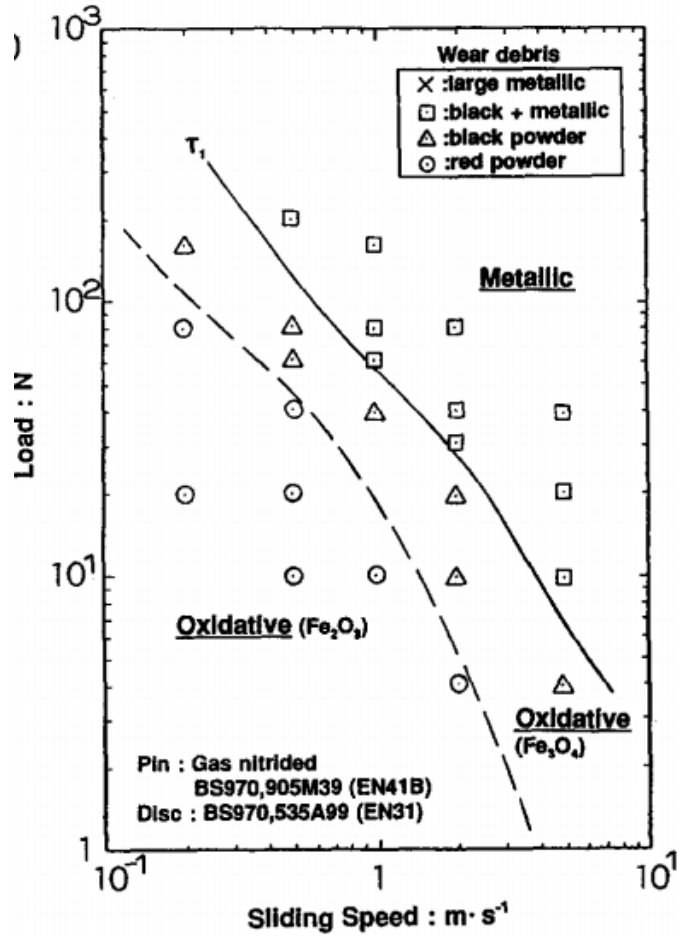
Figure 2.4. Wear mechanism maps for gas nitride BS970,905M39 (EN41B) steel [155].

2.3.2 Boriding

Boriding is a thermochemical surface hardening method which can be applied to a wide range of engineering components to improve their fatigue, corrosion, oxidation and wear resistance [17-18]. The process entails diffusion of boron atoms into the lattice of the parent metal and a hard interstitial boron compound is formed at the surface. The surface boride may be in the form of either a single phase or a double phase boride layer.
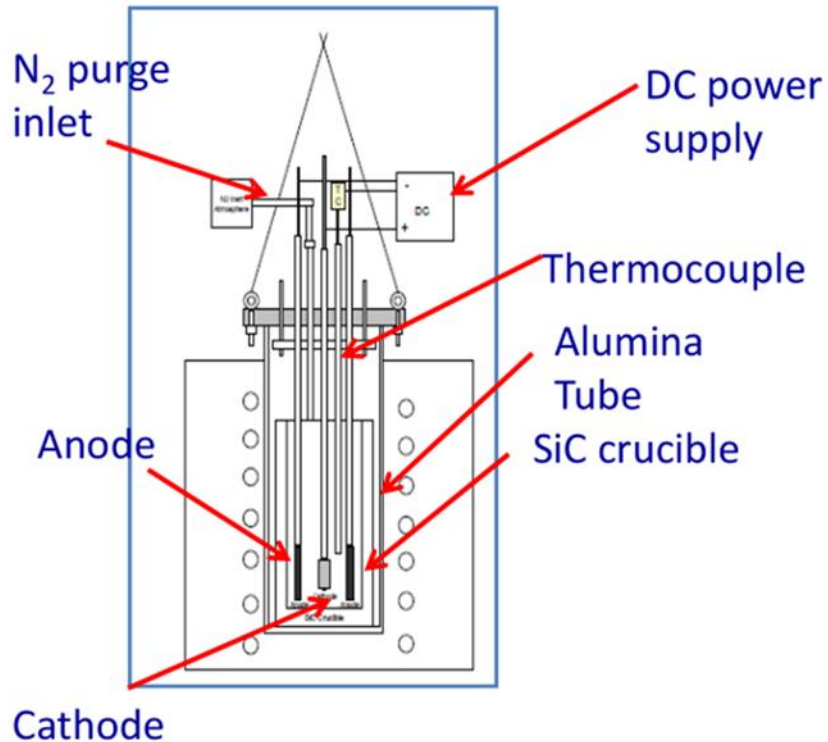
Figure 2.5 Schematic illustration of electrochemical cell included electric furnace, alumina tube, SiC crucible, cathode, thermocouple with SiC tube shield, N2 purge line, water cooled aluminum cap, aluminaplate, and DC power supply [23]

A schematic drawing of the electrochemical cell is given in Figure 2.5. The cell consists of a SiC crucible containing molten electrolyte. All of the boriding processes require high processing temperatures (typically 700 °C - 1000 °C). During electrochemical boriding, boron atoms are extracted from the electrolyte and then deposited onto the surface of steel substrates. Due to their small size and high mobility, these boron atoms diffuse into substrates, and some of them react with substrate atoms and form iron borides.
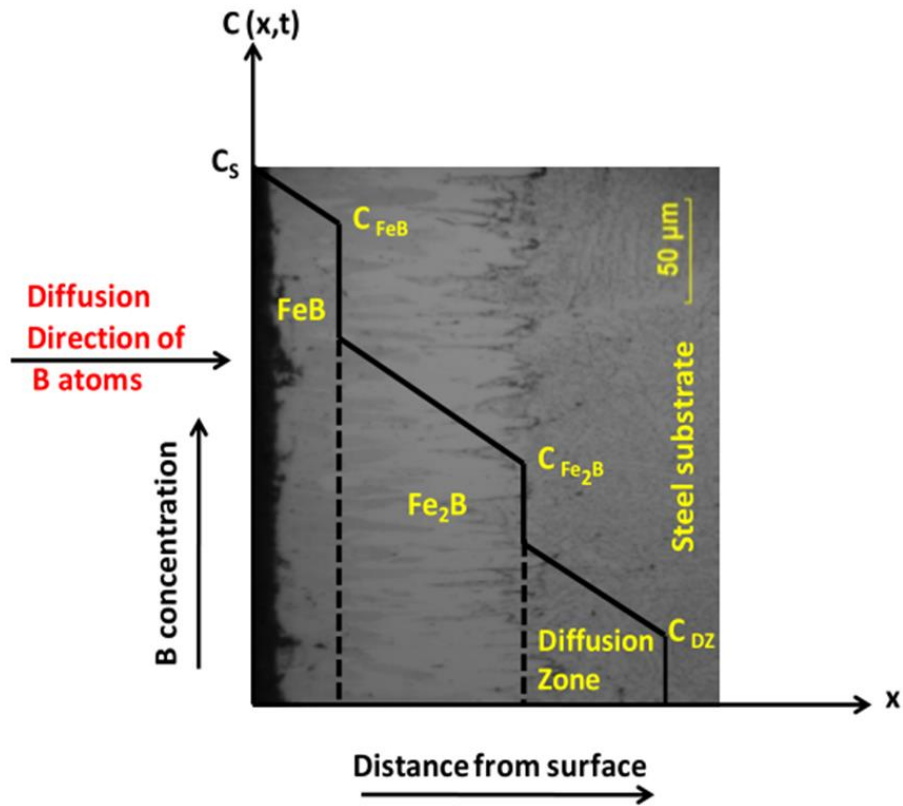
Figure 2.6 Schematic cross section of borided region of an iron-base ferritic specimen/component showing the FeB/Fe$_2$B and the diffusion zone with their (possible) constituents [24].

The borided layer and following diffusion zone was created by boron atoms diffusing into the surface of the heated workpiece. Figure 2.6 shows the schematic cross-section of borided region which consists of two types of iron borides based on the Fe-B phase diagram (Figure 2.7) and diffusion zone [13]. The outer layer consists of FeB with an orthorhombic crystal structure and the inner layer of Fe$_2$B with characteristic saw-tooth morphology having a tetragonal crystal structure. The dual-phase boride layers formed on steel surfaces exhibit high hardness, high abrasive wear resistance and excellent corrosion resistance [19]. The thickness of iron borides depends on the method of boriding treatment, temperature and time of process and their morphology is influenced by the alloying elements present in the substrate [20].
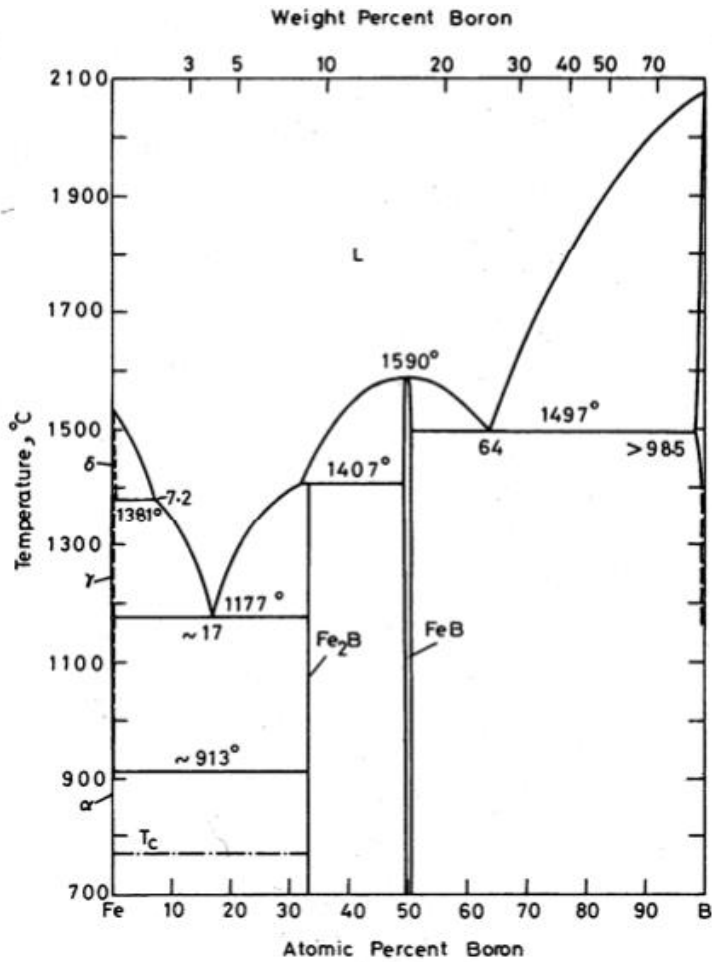
Figure 2.7 Equibrium Iron-Boron phase diagram [13]

However, the higher boron content phase (FeB) means the surface was studied by researchers and found not to be ideal for mechanical and tribological applications. First of all, despite being very hard, the FeB top layer is very brittle. Furthermore, since FeB and Fe_2B borides have different coefficients of thermal expansion, cracks often form at the FeB/Fe_2B interface while cooling down after the boriding treatment, high tensile stresses develop in the FeB phase while compressive stresses form in Fe_2B [21].

The properties of iron boride layers are superior to those formed by nitriding and carburizing, especially in terms of their extremely high hardness values (1600-2300 HV) compared to 650-900 HV for nitriding and carburizing [22]. The ability to withstand the main wear mechanisms such as adhesion, oxidation, abrasion, and surface fatigue was greatly improved because of the combination of a high surface hardness and a low

14

coefficient of friction of a boride layer [36]. Ibrahim and Melih [29] investigated the effect of the boriding process on the adhesion and wear properties of AISI H10 steel using a ball-on-disc tribometer under unlubricated conditions. Compared to the non-borided steel, the wear rate of the borided steel was found to be approximately five times lower attributed to the improved high hardness and coating–substrate adhesion due to the introduction of boriding process. Cárdenas et al. [36] conducted experiments on AISI H13 and D2 steels with a reciprocating wear test machine under dry conditions, and the wear rate of borided steels was found 13 times greater than that of the unborided surfaces. The wear mechanism for the borided surface was identified with plastic deformation and mild abrasive wear. In addition, cracking and spalling were observed on the unborided surfaces.

2.3.3 Heat treatment: Induction Hardening

The objective of heat treating 1045 carbon steel is to change its mechanical properties, namely to increase its hardness, yield strength, without reducing its impact resistance and ductility. Induction surface hardening is a typical heat treatment method where only the selected part or a working surface layer of the steel element is heated inductively and then immediately quenched by immersing it into a quenching medium, while the remaining parts of steel are practically not treated. As a consequence, a thin surface layer is obtained with improved values of hardness and microstructures [25-28].

There are two consecutive stages in the induction surface hardening process, i) heating process: the hardened element is heated inductively in as short a time as possible to the hardening temperature; ii) quenching process: the workpiece is immediately cooled by immersing it in a suitable quenchant after a short break for switching off and removing the inductor. The comparison of the cooling curves of various quenchants according to the temperature against cooling rate is shown in Figure 2.8. Quenching is using to control the cooling rate to obtain the desired microstructures and hardness [30]. The hardness and hardenability are affected by a number of factors, for example the austenitized microstructure and the cooling rate of the quenching medium. Also a complete understanding of the quenching principles and the appropriate selection of a quenchant are required in the heat treatment design.
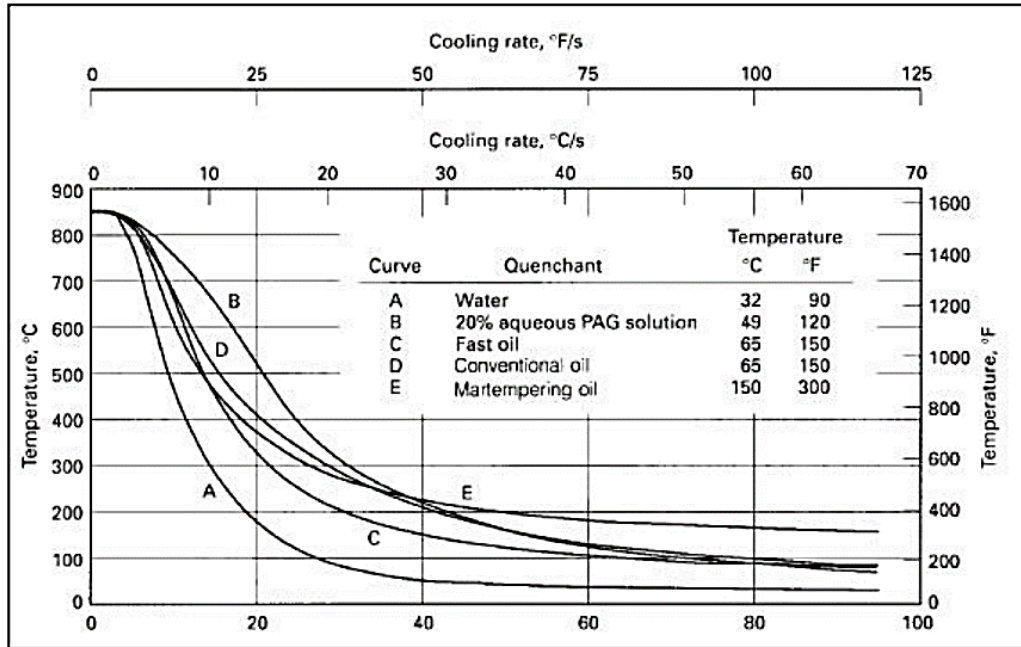
Figure 2.8 Effect of selected quenchants on the cooling curves of a 25.4 mm diameter steel bar. All quenching flowing at 0.5 m/s [30]

The quenching process is consisted of three stages: the vapor blanket stage, the boiling stage, and the convection stage.

1. The vapor blanket stage: when the heated samples are quenched from the austenitizing temperature, a thin vapor pocket is created on the surface of the sample due to the heat could easily evaporate the quenching medium. The conduction and radiation through the vapor blanket becomes the dominate mechanism of heat transfer owing to the poor conductivity of the vapor pocket. Not all quenching medium, such as oil, cause vapor pocket.

2. The boiling stage: the quenchant is directly contacted with the surface of the workpiece after the vapor pocket collapses, which results to the onset of boiling.

3. The convection stage: the surface temperature of the workpiece is reduced by the continuous cooling to below the boiling temperature of the quenchant. The heat convection between the quenchants and the surface of workpiece becomes the dominate method of heat transfer. The cooling rate at this stage is the lowest due to different cooling characteristics, various quenching mediums are used.

16

The procedures of heat treatment are normally designed based on the Iron-Carbon phase diagram [32] as shown in Figure 2.9, which provides the information about the microstructures of steel under thermodynamic equilibrium conditions, for example, the microstructures at the end of equilibrium cooling [31]. It is important to inductively heat the sample to a temperature significantly higher than the traditional austenization temperature Ac3 for completely austenization. The preferred bainitic and martensitic microstructures are achieved by rapidly cooling (quenching) workpieces into various quenching medium. Formation of the various metallographic microstructures are affected by the different cooling rates.
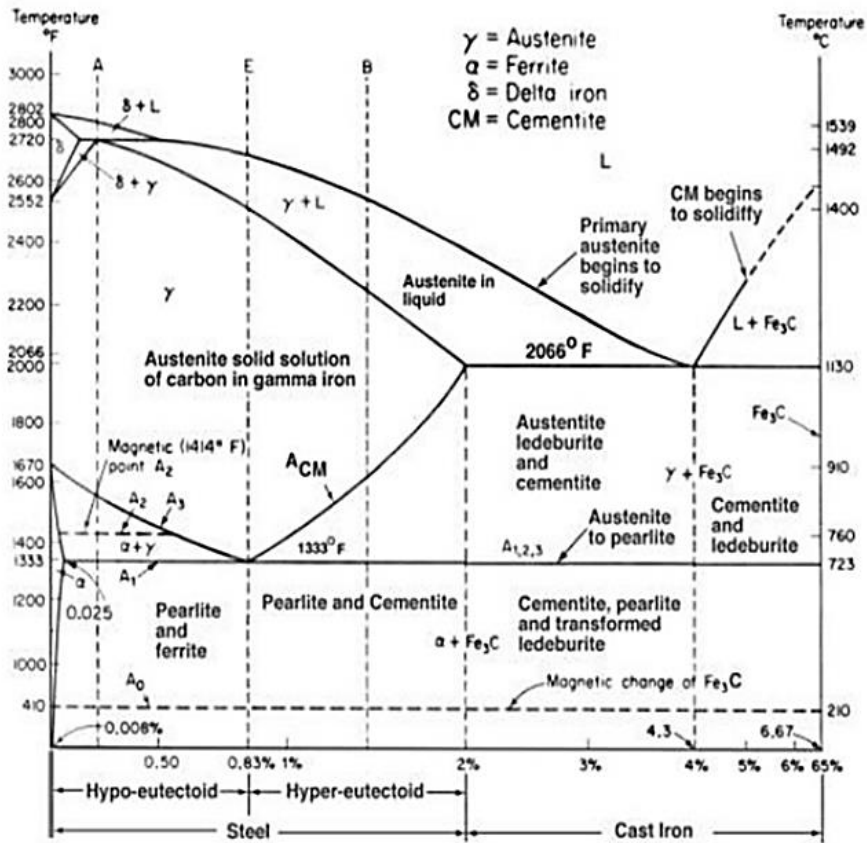
Figure 2.9 Equibrium Iron-Carbon phase diagram [32]

Induction heating provides a method to precisely heat treat electrically conductive materials. There is no contact between the material to be heat treated and the power source.

17

The short heating period aids in austenite grain size control, resulting in improved mechanical properties of the hardened component. There is minimal distortion and decarburization as a result of the short time between heating and quenching. The induction processing is ideal for axisymmetric parts however complex parts can also be heat treated. Chemical composition changes are absent in the induction hardening process compared with the other case hardening operations such as carburizing or nitriding [31].

2.4 Austenite transformations

In industrial application, equilibrium cooling is different from the cooling curves used for heat treatments. At most, the equilibrium cooling can be generally assimilated only at a very slow cooling in the furnace. The Fe-C phase diagram cannot be regarded to predict the microstructures after the heat treatment when cooling curves are different from equilibrium cooling.
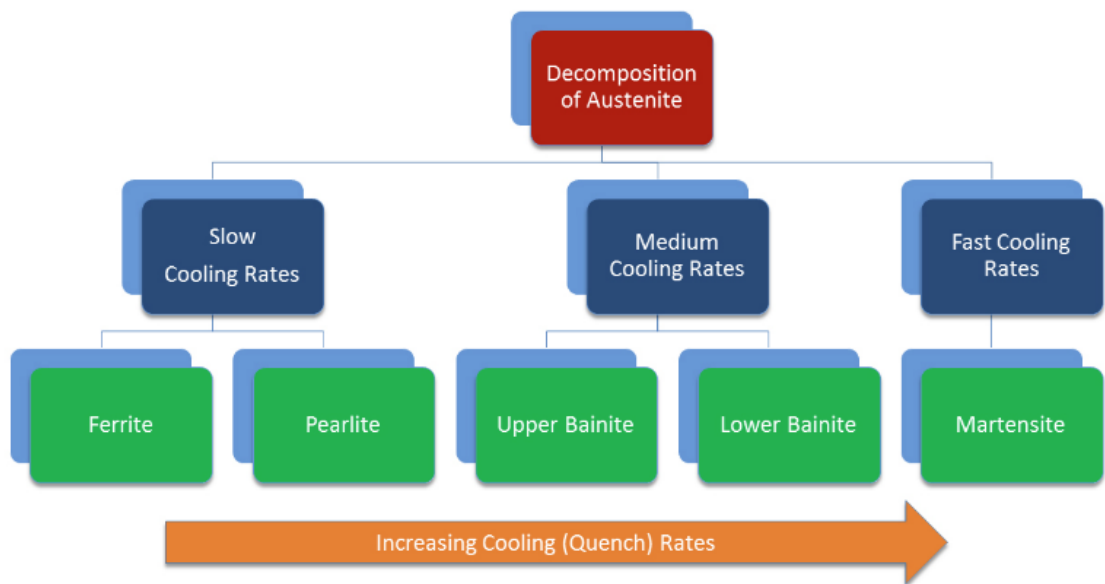
Figure 2.10: The decomposition of austenite as a function of cooling rate [33]

Figure 2.10 [33] illustrates how cooling rates can be varied to obtain microstructures. The two types of diagrams: the isothermal transformation diagrams (TTT) and the continuous cooling diagrams (CCT) were established to predict the austenite

transformations under conditions of non-equilibrium and the microstructure at the end of the heat treatment in relation to cooling curves [34]. According to the cooling curve, austenite can transform:

- Structures known in typical Fe-C phase diagram: ferrite, pearlite, and cementite;
- New structures are not present on the Fe-C phase diagram: bainite and martensite.

2.4.1 Time-Temperature-Transformation (TTT) Diagram

The austenitized steel cooled at a constant temperature below the austenite region will transform to some transformation phases such as pearlite or bainite. This transformation can be summarized by plotting the amount of austenite transformed against the corresponding elapsed time at constant temperature. The information for a given steel is provided by a series of such curves (each curve determined at a different temperature) can be understood through a single diagram called a Time-Temperature-Transformation (TTT) diagram, also called the Isothermal Transformation (IT) diagram.

Figure 2.11 shows a typical TTT diagram for a general hypoeutectoid steel (C < 0.77%), where A_3 is the upper critical temperature (point), below which ferrite starts to form as a result of ejection from austenite in the hypoeutectoid alloys; A_1 is lower critical temperature (point) of the austenite-to-pearlite eutectoid transformation. Below this temperature austenite does not exist; Ms and Mf are the start and finish temperatures of the transition from austenite to martensite. The TTT diagram can be thought of as a relationship between specific microstructure which is defined by the cooling curve and constant temperature and time. This allows estimates to be made regarding how the steel will respond to any mode of cooling from austenite [33-34]. The position of the transformation zone is defined by start and finish curves.
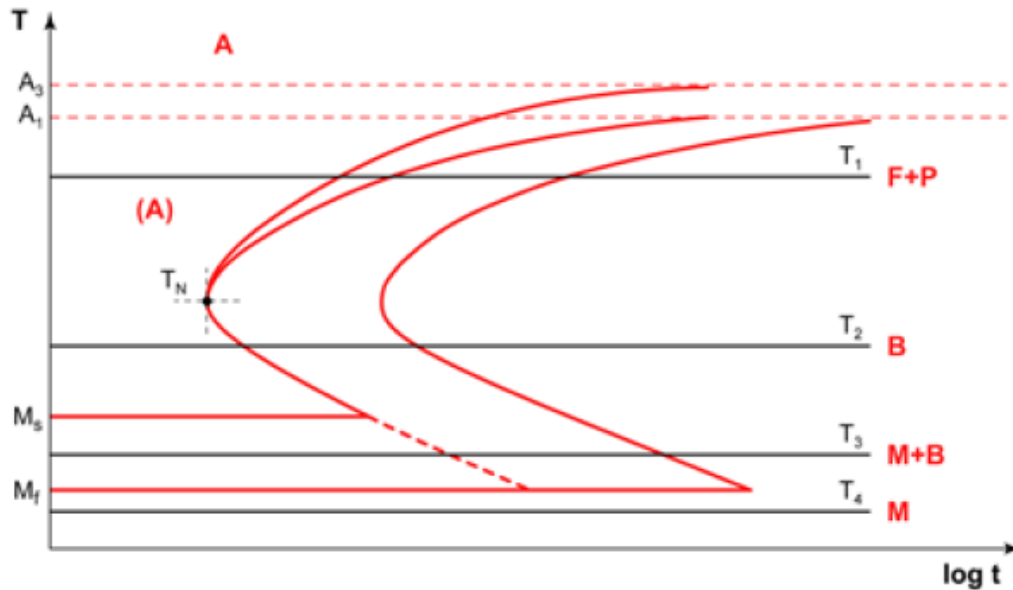
Figure 2.11 Typical TTT curve for a generic hypoeutectoid steel (C < 0.77%) [34].

The upper critical temperature (point) A3 is the end temperature of austenite transformation in the hypoeutectoid steel, all ferrite and pearlite in the hypoeutectoid steel transform into austenite. The lower critical temperature (point) A1 is the temperature which austenite begins to form in the eutectoid steel (including hypoeutectoid steel and hypereutectoid steel). The specific temperature is 727°C and also called the eutectoid point. As shown in Figure 2.11, the microstructures of four isothermal cooling curves on the TTT diagram are consisted of:

- At the end of T_1: ferritic-pearlitic microstructure;
- At the end of T_2, bainitec microstructure;
- At the end of T_3, martensitic-bainitic microstructure;
- At the end of T_4, martensitic microstructure.

2.4.2 Continuous Cooling Transformation (CCT) Diagram

CCT diagram shows the microstructures transformed at different cooling rates. They provide the information in selecting quenching medium with quick enough quenching speeds resulted in the high cooling rates to form martensitic and bainitic microstructures. The essential difference between TTT diagrams and CCT diagrams is that TTT diagrams

20

examine the progress of transformation as a function of time, at a constant temperature, whereas CCT diagrams at a changing temperature. In CCT diagrams, the transformations of austenite are shifted to lower temperatures and longer times. The CCT diagrams allow the prediction of microstructure and hardness, which is not possible using a TTT curve [35,46].

Figure 2.12 illustrates the transformation during the continuous cooling of the hypoeutectoid steel (C < 0.77%). The cooling curves are very different with related to the isothermal cooling. The temperature changes continuously from the austenitization temperature to room temperature, according to different cooling curves that become increasingly abrupt [34]. The curves indicated with V_s and V_i, also in this case represent two limit conditions: V_s is the slowest cooling rate that forms only the martensitic microstructure; V_i is the fastest cooling rate that forms only ferrite and pearlite.

As shown in Figure 2.12, the microstructures of four isothermal cooling curves on the CCT diagram are consisted of:

- At the end of T_1: ferrite, pearlite;
- At the end of T_2, ferrite, pearlite, bainite, and martensite;
- At the end of T_3, ferrite, bainite, and martensite;
- At the end of T_4, martensite.

According to the research, the addition of alloying elements including carbon, results in a delay in the austenite transformation and an increase of the mean grain size. In conclusion, the more the amount of alloying elements, the more moved down and right are T.T.T. and C.C.T. diagrams, and allowing complete transformation to martensite at a lower cooling rate. Similar effects are caused by increasing the austenitization time and the austenitization temperature [34,47].
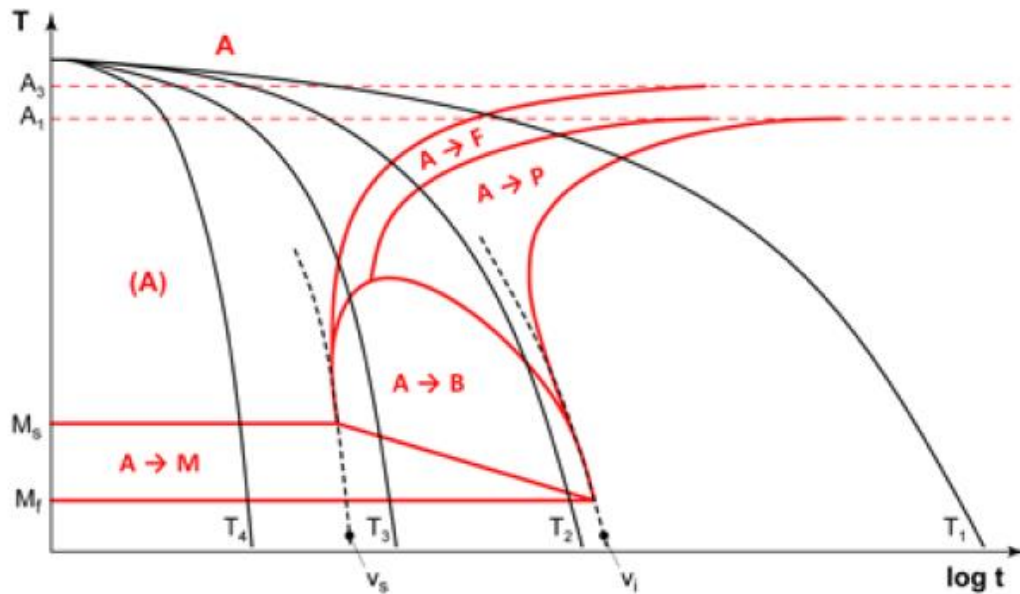
Figure 2.12 Continuous Cooling Transformation (CCT) diagram of a generic hypoeutectoid steel (C < 0.77%) [34].

2.4.3 Microstructures Produced During Cooling

The Fe-C phase diagram and T.T.T. or C.C.T. diagrams emphasize how steel may consist of different microstructures due to the chemical composition and the cooling methods. The microstructures of steel refer to austenite transformation mechanisms can be classified as follows [34]:

- Microstructures such as pearlite, ferrite, cementitite or bainite, which are formed by austenite transformation through nucleation and growth mechanisms due to carbon diffusion;
- Microstructure such as martensite, which is formed from austenite for instant transformation without carbon to diffusion.

The ferrite, pearlite, and cementite are often classified as equilibrium microstructures and bainite and martensite as non-equilibrium microstructures.

22

2.4.3.1 Pearlite

Pearlite is usually formed due to the slow cooling rate. It is a lamellar (or layered) structure that is composed of two different phases: ferrite and cementite. The pearlite exists as grains, also called "colonies"; within each colony the layers are oriented in essentially the same direction, which varies from one colony to another. The thick light layers are the ferrite phase, and the cementite is formed as lamellar plates in the ferrite matrix. Many cementite layers are so thin that adjacent phase boundaries are very close together and are indistinguishable at low magnification. Mechanically, pearlite has properties intermediate between the soft, ductile ferrite and the hard, brittle cementite [34]. Pearlite can be found in the microstructure of a quenched part when the austenization process was not complete.
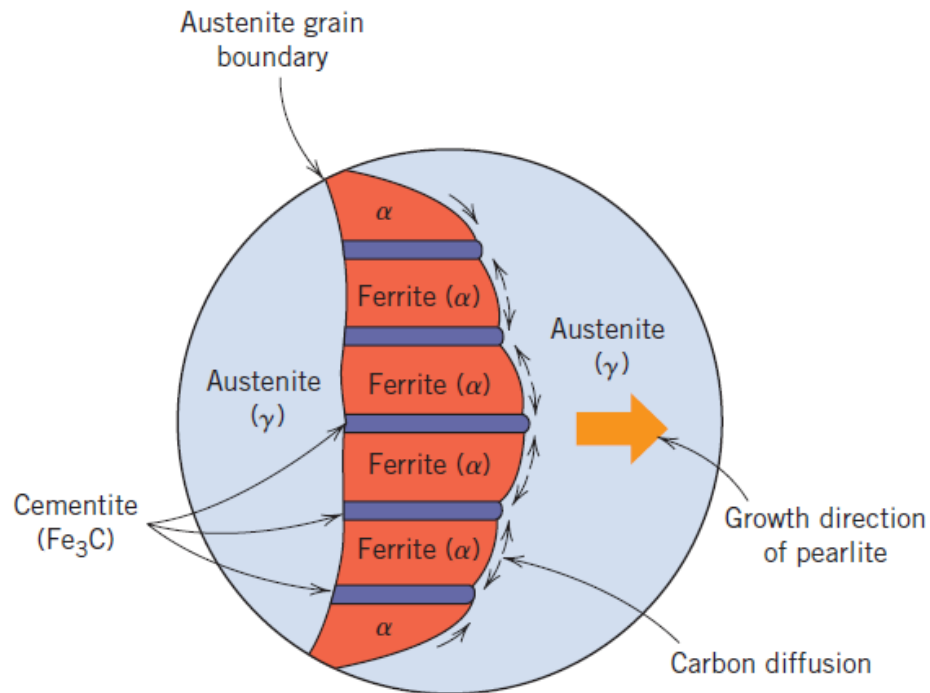
Figure 2.13 Schematic representation of the formation of pearlite from austenite; direction of carbon diffusion indicated by arrows [34].

Figure 2.13 illustrates schematically the microstructural changes that accompany this eutectoid reaction; the directions of carbon diffusion are indicated by arrows. Carbon

atoms diffuse away from the ferrite regions and to the cementite layers, as the pearlite extends from the grain boundary into the unreacted austenite grain. The layered pearlite forms because carbon atoms need diffuse only minimal distances with the formation of this structure [34].

2.4.3.2 Bainite

Bainite is a very fine structure consisting of ferrite and cementite phases, both with an acicular morphology formed at temperatures between 250°C and 550°C, and thus diffusional processes are involved in its formation. The transformation of austenite into bainite occurs through nucleation and growth and is governed by the diffusion of carbon. In relation to the transformation temperature, it is referred to as upper bainite (400°C - 550°C) and lower bainite (250°C - 400°C). At these temperatures the rate of carbon diffusion is less than what occurs during the pearlitic transformation and sharp laths of ferrite surrounded by acicular plates of cementite form from austenite grain boundary [34].

Figure 2.14 shows a schematic representation of the nucleation and growth mechanisms of bainite. For Upper bainite, both laths of α-phase and acicular plates of Fe_3C phase are oriented in the same direction. For lower bainite, the mobility of carbon is further limited and the laths of ferrite are finer than the case of upper bainite, and plates of iron carbide (Fe_3C) tilted at approximately 60° with respect to the axis [34].

Bainite forms as needles or plates, depending on the temperature of the transformation; the microstructural details of bainite can be observed under an optical light microscope as dark etching, acicular aggregates, or dark needles, which are ferrite platelets either with or without slim carbides (can be cementite or carbides); or ferrite platelets either with or without retained austenite sandwiched in between. Bainite ferrite platelets are lath or lenticular plate like structures. With increasing carbon content, bainite morphology changes from lath like to plate-like [37]. Figure 2.15 shows the correlation between the isothermal transformation temperature of the bainitic microstructure and the Vickers hardness. The ferrite of bainite is harder than ferrite of pearlite due to the high density of the dislocations. As a result, the hardness of bainite is greater than the hardness of pearlite and is between 300 and 650 HV [34].

24
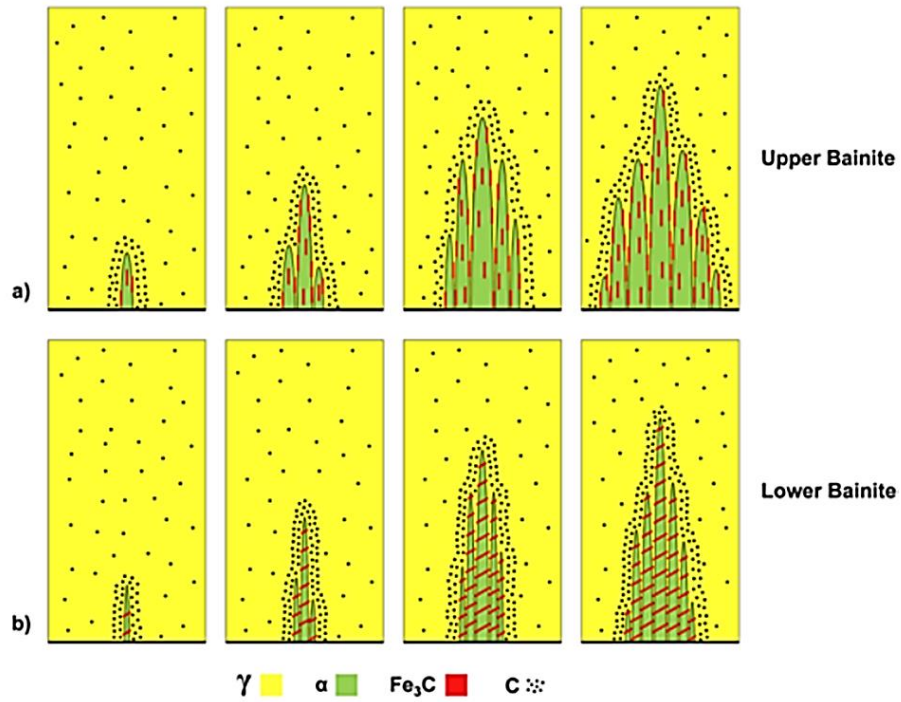
Figure 2.14 Schematic representation of nucleation and growth mechanisms of bainite: (a) upper bainite; (b) lower bainite [34].
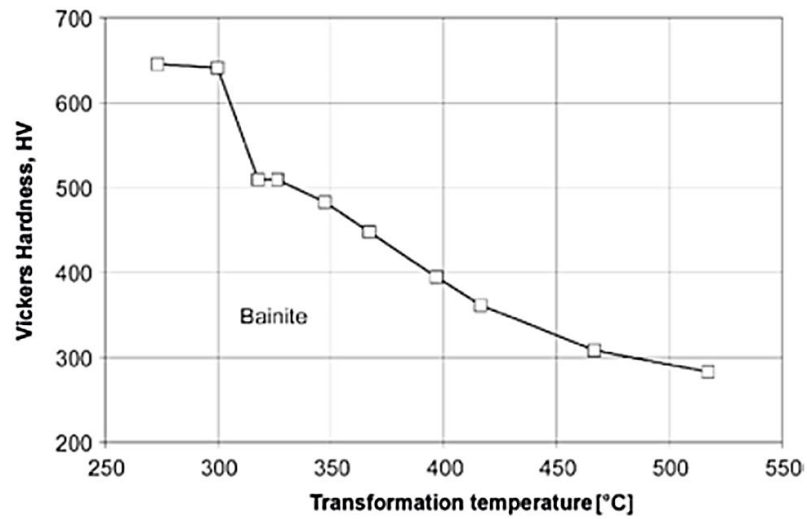
Figure 2.15 Correlation between the isothermal transformation temperature of the bainitic microstructure and the Vickers hardness [37]

2.4.3.3 Martensite

Martensite is obtained by instantaneous transformation of the austenite lattice below the Ms temperature, which varies greatly with composition. The transformation from austenite to martensite occurs without diffusion phenomena and is due to a rapid cooling when the cooling rate is higher than the cooling curve on the C.C.T. diagrams. This microstructure has a body-centered tetragonal lattice (B.C.T.). Since carbon does not diffuse during the transformation, the phase is actually a supersaturated solution of carbon in ferrite. Martensite has an acicular morphology, for carbon contents lower than 0.6%, the microstructure is formed of lath (lath martensite); however, if the carbon content is greater than 1%, the microstructure is formed of plates (plate martensite); lastly, if the carbon content is between 0.6% and 1%, the microstructure is mixed. In both cases, the acicular microstructure of martensite consists of lath or plates arranged according to an equilateral triangle shape [34].
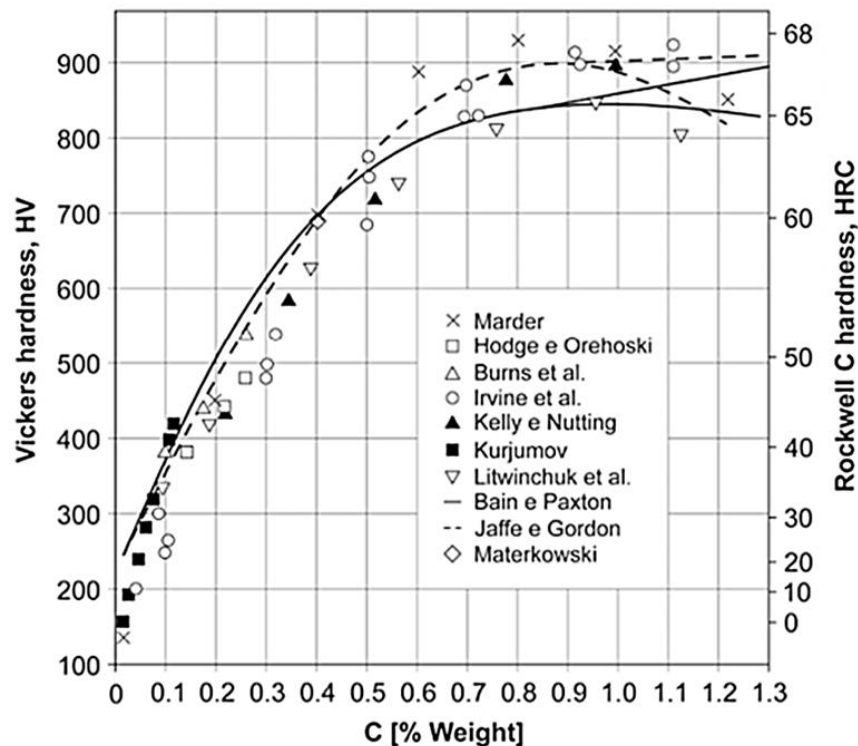
Figure 2.16 The effect of carbon content on the hardness of as-quenched martensite [38].

26

The hardness of martensite is therefore only a function of the carbon content and is between 400 and 800 HV as is shown in Figure 2.16. The only way to change hardness of the martensitic microstructure is to change the carbon content. The martensitic microstructure has always the same hardness for the same type of steel [34]. The martensite formation mechanism is one in which a shear stress moves iron atoms cooperatively and almost simultaneously from their original sites in the austenite structure to the nearest available site in the final structure. On the T.T.T. and C.C.T. diagrams, there is a martensite start temperature and a martensite finish temperature, M_s and M_f. It should be noted that there is a volume increase when transforming austenite to martensite [39-41].

2.4.3.4 Retainted austenite

Austenite that does not transform to martensite upon quenching is called retained austenite (RA). As indicated by the T.T.T. and C.C.T. diagrams of ductile iron, the M_f temperature is always below room temperature. Thus, there is always a certain amount of residual or retained austenite found at room temperature after quenching. The amount of retained austenite is a function of the carbon content, alloy content (especially nickel and manganese), quenchant temperature and subsequent thermal and/or mechanical treatments. In practical manufacturing processes, the excessive amount of retained austenite may result in premature wear or spalling of the surface of the engineering components [42-45].

2.5 Tribological behaviour

Wear, a physical and chemical process of material damage and removal, broadly includes four distinct processes, all of which involve the removal of material from the surface [48]. A typical wear-system involves (a) contact between at least two materials; (b) force; (c) relative movement between the two materials and finally, (d) the environment. According to the motion, wear processes could be identified as sliding wear, rolling wear, oscillation wear, impact wear and erosive wear. Related to the interfacial element, wear processes are called dry or lubricated, or 2-body and 3-body wear [49]. The topic of wear

is a huge subject, so the aim of the review presented here is to focus on the specific subject of sliding mechanism that has been studied in detail in the following chapters.

2.5.1 sliding wear

Sliding wear can be defined as a relative motion taking place in surface and subsurface regions under a certain normal load, sliding speed, atmosphere composition etc. The surfaces could be metallic or nonmetallic, and lubricated or unlubricated. The damage phenomenon may occur by surface grooving due to penetration of hard asperities, oxide particles during sliding or by plastic deformation [49]. Figure 2.17 illustrates a curve plotting of mass loss against sliding distance (or time). The accommodation process of surfaces in contact can be observed in the initial period, and a direct relation between wear and time is established in the second period, where the wear rate featuring the tribological system behavior can be calculated for the mild wear where equilibrium conditions are reached. Finally, after a certain operation time, the failure of sliding components may occur in the third period [50].

In sliding contact, wear can occur due to adhesion, surface fatigue, tribochemical reaction and abrasion. The wear mechanisms are determined by many factors such as the properties of the solid body, the type of contact and counterbody, the interfacial elements and also the loading conditions [49]. The wear rate value is also associated with the wear mechanism especially in a lower scale. The life operation of machine components is determined by the wear mechanism in the steady-state regime or by reaching a high wear rate or friction coefficient levels [50].

Wear of sliding surfaces are dominated by three main factors, mechanical stresses, temperature, and oxidation phenomena. Figure 2.18 illustrates the different wear mechanisms which occur during sliding wear dominated the changing of the surface. Figure 2.16(a) shows that adhesive junctions are built on clean mating surfaces due to the material detached or transferred. Surface fatigue can lead to the sheet-like wear particles formed during repeated plastic formation by a harder counterbody as shown in Figure 2.16(b). As shown in Figure 2.16(c), the cracking of brittle materials such as ceramics is formed due to the Surface traction in sliding contact. Loose wear particles, as the result of

28

cracking of surface films formed by tribochemical reactions, can act abrasively if they are harder than the base materials [49].
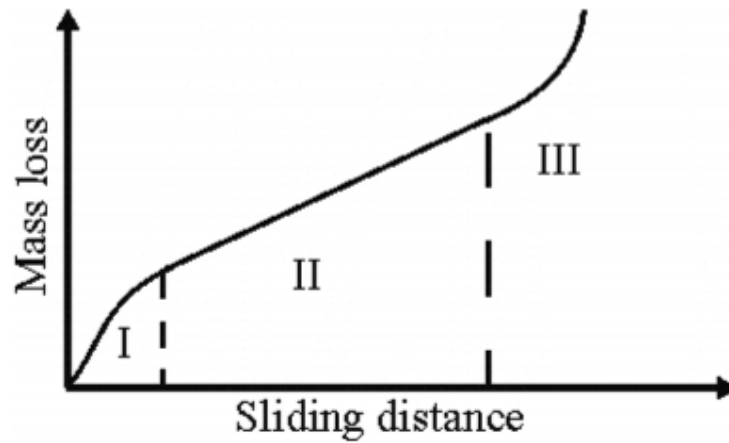
Figure 2.17 Typical plot of mass loss against sliding distance [50].
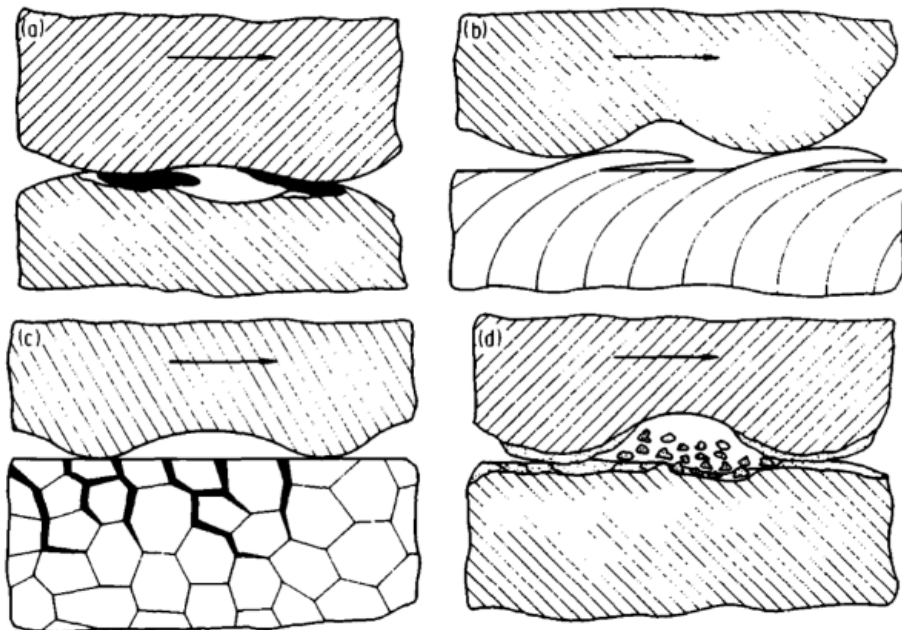
Figure 2.18 Mechanisms of wear during sliding contact a) adhesive junctions, material transfer and grooving, (b) surface fatigue due to repeated plastic deformation on ductile solids, (c) surface fatigue results in cracking on brittle solids and (d) tribochemical reaction and cracking of reaction films [49].

2.5.2 Mild and Severe Wear

The two main wear mechanisms in the sliding wear of steels were investigated by Archard and Hirst in 1956, a mild wear and a severe wear. After the running-in regime has finished, these two wear mechanisms result in the mass loss in steady-state regime. The terms of mild wear and severe wear are used to describe conditions on the either side of the transition [49-50].

Mild wear is caused by the oxides formation on sliding surfaces as a result of high temperatures achieved by friction heating. The oxide layer decreases the frictional resistance because of its low shear strength. Mild wear usually is associated with low wear rate, smooth surface, a steady friction trace and usually occurs at low loads and velocities. Also the formation of fine wear particles (debris) occurs during mild wear. On the other hand, severe wear is characterized by adhesion, plastic deformation, formation of junctions, transfer and back-transfer of materials. Later, material transferred becomes wear particles, leading to roughening of the surfaces of the sliding pair and in a coefficient of wear at least one to three orders of magnitude greater than that in mild wear. Severe wear occurs in high contact surface temperatures with the mechanical damage accompanied by high load and velocity. Difference between the mild wear and the severe wear is the change in magnitude of the wear rates with load, sliding velocity, and/or sliding distance [49-51].

2.5.3 Sliding Wear Mechanisms

Wear during sliding is a function of the state of the stresses generated by contact between two sliding elements. The researchers Lim and Ashby [51] identified and described four broad classes of wear mechanisms that cause loss of material from the sliding surfaces:

Seizure: When two surfaces touch, the localized pressure on the asperity contacts causes plastic indentation, large-scale mass flow, and metallic transfer following a period of severe wear or immediately upon contact under high load [51]. The temperature increase caused by high relative velocity between the sliding surfaces may reach the melting point of one or both sliding surfaces. If melting of surfaces occurs, it causes a decrease in the

coefficient of friction and an increase in wear rate as the strength of metal drops rapidly [51, 52],

Melt wear: At higher velocity (10 - 100 m/s) the coefficient of friction drops to very low values because a film of liquid metal forms at the sliding interface giving "melt lubrication". As the temperatures increased so high that oxidation is competed with local melting as the dominant wear mechanism in the inert atmospheres.

Oxidation Wear: Surface oxidation has been stimulated by the frictional heating associated with the range of sliding velocities. It is distinguished by two regimes, mild and severe surface oxidation. The distinction between these two surface oxidations lies in the sliding velocity, normal load, area of covered surfaces, thickness, and strength of the layers [51, 55-57]. When the sliding speed exceeds l m/s with a light load, or in case of lower speed with higher loads, the mild surface oxidation occurs but the oxide film is characterized as thin, brittle and patchy. However, at higher velocities (more than 10 m/s for steel), the surface totally covered by the thicker and more continuous oxide film which is called severe surface oxidation. During this regime, heavily frictional heating causes oxide melt and flow on the oxide-coated surfaces. The tribological functions of oxides formed during oxidation wear are listed as follows:

- Oxide films prevent the metallic contact between sliding surfaces.
- Oxide films serve as a supplementary and effective lubricant.
- Owing to their high mechanical properties, oxide films have a shield (protecting) action, significantly reducing the operating stresses in subsurface layers [54].

Delamination wear: This mechanism is based on the plastic deformation at the subsurface results in the void and crack formations. The following joining of cracks by shear deformation reached the surface and its propagation to surface may lead to the flake like sheet debris which causes ultimate failure of the surface. The adhesive and ploughing actions cause normal and tangential forces transmitted through contact points from one surface to the other during sliding. When the sliding velocities are below about 0.1 m/s, the metal surface is deformed and sheared by the frictional force along its sliding direction

while the surface heating is negligible. The four mechanisms of delamination wear are listed as follows:

- Plastic deformation of the surface.
- Crack nucleation at the sub-surface due to plastic deformation.
- Crack propagation from these nucleated cracks due to plastic deformation.
- Creation of loose wear sheets.
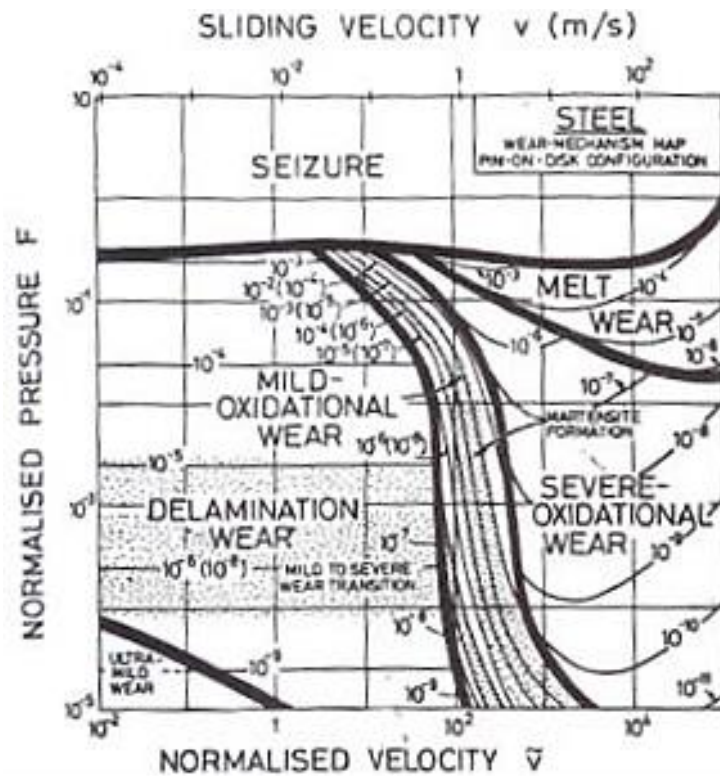
Figure 2.19 The wear-mechanism map for a steel [51].

The empirical wear-mechanism map for steel is established under a range of normalized velocity and normalized pressure (normal load) as shown in Figure 2.19. It can be regarded as a summary of the wear behaviour of dry sliding on steel. Also the wear rate and the regime of dominance of each of a number of competing mechanisms of wear can be founded on the wear map. Contours of constant normalised wear rates are superimposed on fields showing the regimes of dominances of different wear mechanisms. There are discontinuities in the contours when they cross the field boundaries into the regimes of

severe-oxidational wear and melt wear. The shaded regions indicate a transition between mild and severe wear [51].

2.6 Wear behavior of steel microstructures

The wear performance of steels can be affected by a number of factors such as wear conditions of its microstructure and environment. Also the extent of work hardening and deformation of the surface regions have the influence in material removal. The researchers have tried to correlate the microstructures and bulk hardness of steel against wear resistance as shown in Figure 2.20, since there is no exact relationship between the variables [58-59].
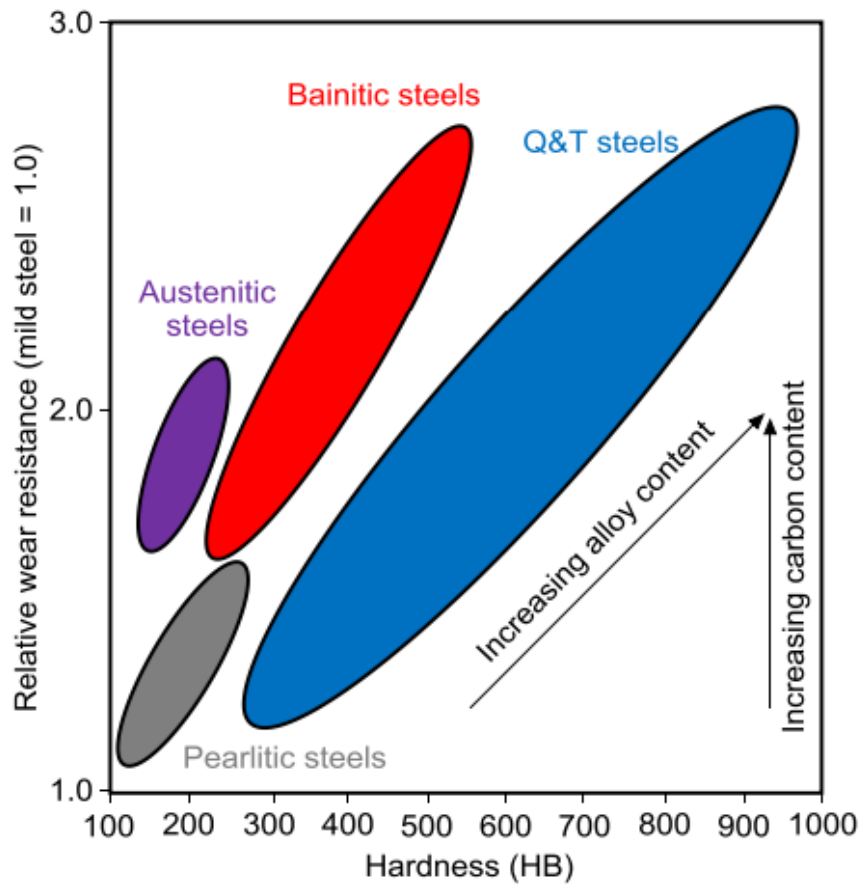
Figure 2.20 Effect of microstructure and bulk hardness on relative wear resistance compared to mild steel [63].

Hardness and toughness are quite often used in the field of wear resistance as the criteria for judging surface treatment, where the hardness can reduce the extent of penetration of abrasive particles and the toughness can inhibit crack formation and material detachment during the sliding. Figure 2.20 illustrates that steels with similar hardness have different microstructures and also vary in their wear resistance. Because of the higher strain hardening capacity and ductility of austenite, it exhibits a higher abrasion resistance compared to bainitic and pearlitic structures at equivalent hardness. In steels with less than l.0% carbon, bainite shows higher wear resistance than quenched and tempered microstructures, annealed structures and spheroidized structures, all at the same hardness level. Martensite is less ductile leading to greater material removal during sliding [60]. In addition, a tough work-hardened layer on the worn surface can be formed in austenitic steels during sliding which can resist further damage [61]. Because of the decreased lath thickness of bainitic ferrite and the lower amount of retained austenite, the wear resistance of the austempered sample is improved due to the increased hardness and acceptable toughness [62-63].

2.6.1 Ferritic-pearlitic steels

Ferritic-pearlitic microstructure is the morphology of the iron carbide in steel which plays an important role in wear resistance. The pearlite colonies are dispersed as hard phases in the softer ferritic matrix, thus the penetration and subsequent material removal are hindered during the wear. The deformation in ferrite is also constrained by pearlite which reduces the rate of material removal. Figure 2.21 shows the wear mechanisms of hard particle in ferritic-pearlitic steels, where the work hardening is caused by the indentation of hard particles in the nearsurface due to the plastic deformation of the soft ferrite phase [63].

Many studies have pointed that pearlite exhibits better wear resistance than spheroidal carbides due to the lamellar structure at similar hardness [64-65]. The lamellae in pearlite act as barriers to the moving abrasive particles, which required for more energy to deform and fracture lamellar carbide [66]. Lamellar pearlite shows better wear resistance

compared with tempered martensite containing fine carbides and spheroidised carbide [67-68]. However, the performance of pearlite varies with the size of the abrasive particles.
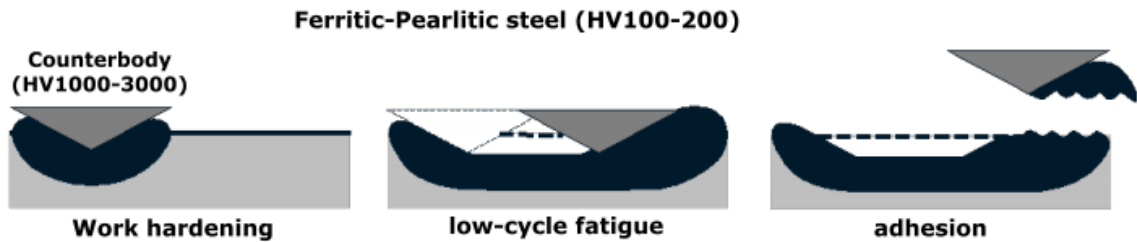
Figure 2.21 Schematic hard particle wear mechanisms in ferritic-pearlitic steels [63].

Previous researches indicate that the reduction of the pearlite interlamellar spacing in steels can increase resistance to sliding wear [69-71]. However, the interlamellar spacing is inversely related to the wear resistance with the carbon content in hypoeutectoid pearlitic steels. In hypereutectoid steels, the continuous network of cementite cannot be plastically deformed during abrasion at the prior austenite grain boundaries, where the brittle fracture can generate cracks along those boundaries. This could be responsible for the saturation of wear resistance in hypereutectoid steels.

2.6.2 Martensitic steels

Martensite is identified as the structure that shows better wear resistance compared to ferrite, pearlite and bainite due to its high hardness according to a number of investigations [72-74]. Figure 2.22 shows the wear mechanisms of hard particle in martensitic steels. The soft, deformable phase cannot be observed owing to its very high hardness. The formation of micro-cracks is caused by upon indentation of hard particles into the surface of martensitic steel. A wear particle can be cut lose after several adjacent micro-cracks link up. However, high carbon martensitic steel (C ~ 0.65 -1.2 wt%) has been found to exhibit higher wear rates compared to low carbon (C ~ 0.16 - 0.37 wt%) martensites owing to relatively low toughness [75].

35

Martensitic steel (HV300-600)

Counterbody
(HV1000-3000)

cracking   cutting
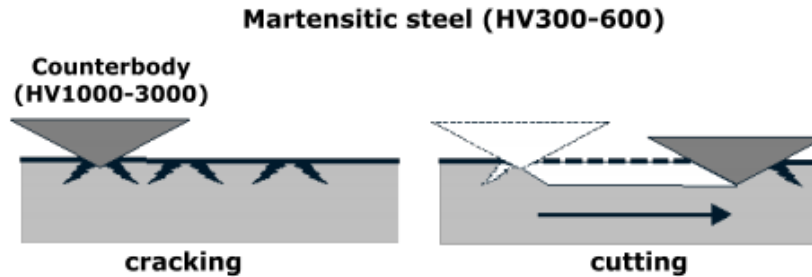
Figure 2.22. Schematic hard particle wear mechanisms in martensitic steels [63].

Figure 2.23 illustrates the hardness of ferritic-pearlitic and martensitic microstructures against the weight loss of wear under the same test conditions. In ferritic-pearlitic steel, increasing the hardness leads to a minor improvement of wear resistance. In contrast, the hardness increase in a martensitic microstructure results in substantial gains in wear resistance. This difference is found as the consequence of different wear mechanisms acting in both steels as shown in Figure 2.21 and Figure 2.22 [63].

The structure of ferrite and martensite exhibit better wear resistance compared with ferrite and pearlite mixture during dry sand rubber wheel testing, because of its higher volume fraction of martensite [76]. In order to raise the resistance against crack-based wear mechanism, three methods could be used:

1. Increasing the steel hardness raises the elastic limit stress of the material reducing the formation of cracks.
2. Refining the microstructure obstructs the propagation of existing cracks, in particular, increasing the number of large angle grain boundaries.
3. Embedding ultra-hard special carbide phases in the martensitic matrix can carry the highest contact stresses without fracturing.
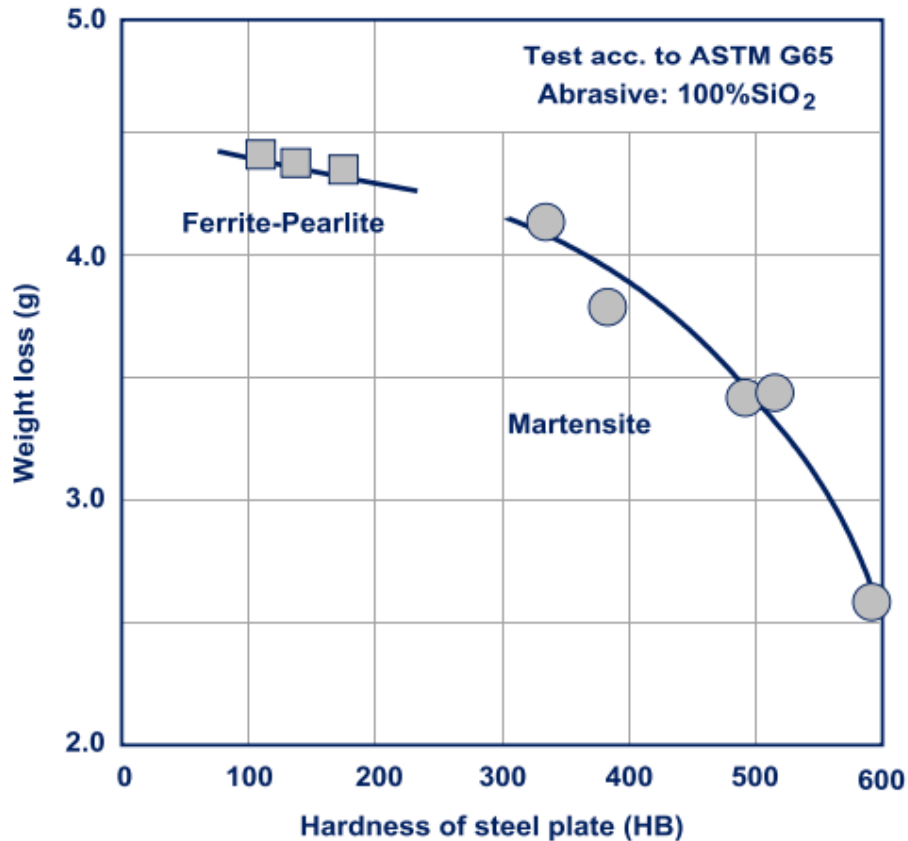
Figure 2.23 Relationship between hardness, microstructure and weight loss in rubber wheel test [63].

2.6.3 Bainitic steels

The wear performance of bainitic steels is still a controversial issue. Richardson firstly pointed that bainitic steels show better wear resistance than other microstructures at similar hardness and composition [77]. Xu and Kennon investigated two-body abrasion tests on plain carbon steels over a wide range of compositions (0.10 - 1.4 wt% C) and microstructures, and bainite exhibited the highest wear resistance followed by tempered martensite and rest of the annealed structures for C <1.0 wt%. Spheroidised structures are demonstrated to show the lowest wear resistance [78]. Hurricks [79] carried out experiments on the abrasion resistance in lower bainite owing to its hardness and ductility. The number of studies have shown bainite having a small advantage over martensite in wear resistance at a similar hardness [80-83] due to lower plastic deformation and high

toughness caused by either a higher fraction of small carbides or retained austenite. However, those effects are both related to the type of austempering treatment and composition of the steel. Under sufficiently high pressure the retained austenite transforms to fresh martensite and this transformation increases wear resistance.

Since the mixture of martensite and bainite provide excellent impact toughness as well as high ductility, higher yield, and tensile strengths [76] than fully martensitic steels, the bainitic steels have been increasingly popular. The toughness of bainitic steels is improved by undergoing continuous cooling processes [84]. The mechanical properties of bainitic steel are determined by, the morphology of the microstructure, the formation of fine or coarse bainite and the way it is distributed throughout the microstructure It has been found that the strength and hardness of the bainitic structure comes from the thin plates of the bainitic ferrite [85-87]. For instance, Caballero investigated the lath-like upper bainite, consisting of thin and long parallel ferrite laths were found to have higher impact toughness than granular bainite [88]. At the nanoscale, the high strength and toughness of the slender and tiny bainitic ferrite plates separated by thin films of retained austenite due to the high dislocation density and other defects in the bainite [88].

2.7 Parameters that affect wear behaviour

2.7.1 Bulk hardness

Hardness is the resistance to mechanical indentation, such as in a hardness test point making an indentation of various depths in samples. Wear resistance is the ability to reduce or resist material loss from abrasive or adhesive wear. Hardness is usually regarded as the criteria for judging wear resistance of materials. Figure 2.24 shows a linear relationship between relative wear resistance and Vickers hardness with pure annealed, cold worked and heat treated steels in wear tests, and the following equation is [89-92]:

$$\varepsilon = bH \qquad (1)$$

ε is the relative wear resistance, H is the Vickers hardness and b is a constant of proportionality. Moreover, they proposed that the wear-resistance depends strongly on the physical and mechanical properties of the abrasive, consistent with other work [93,94]. This relationship does not hold good for work-hardenend metals and alloys [95].
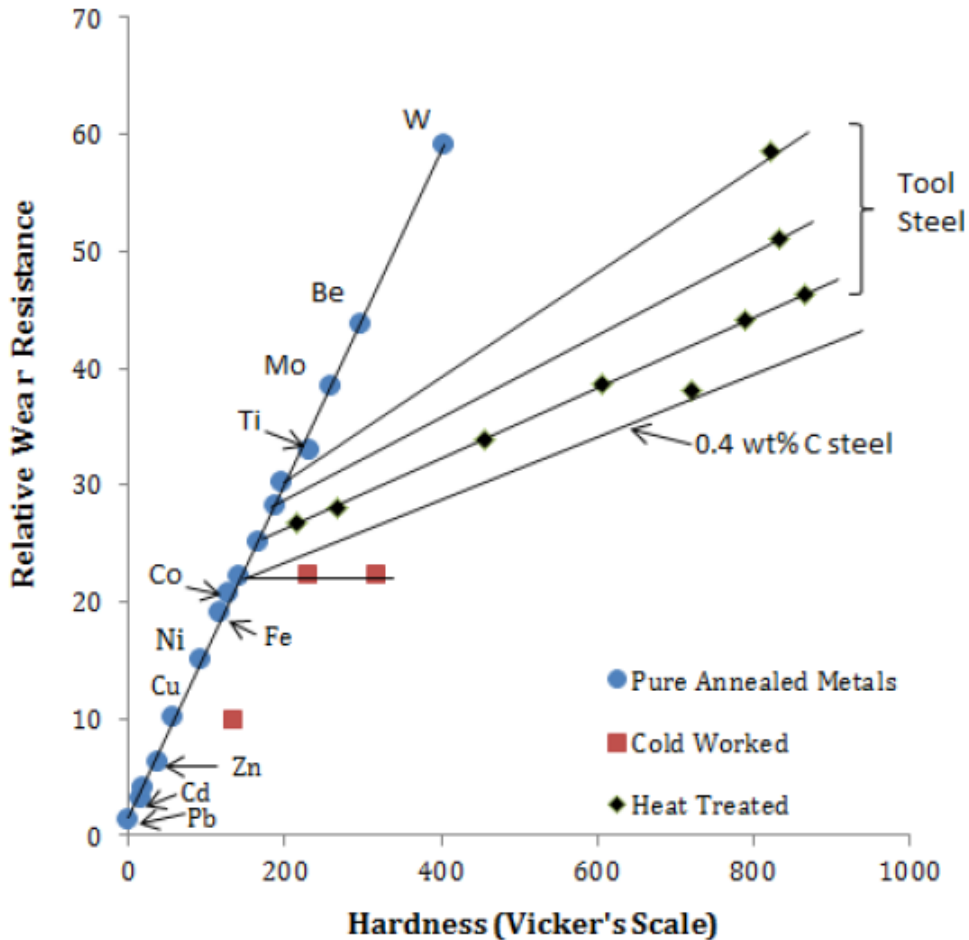
Figure 2.24 Relative wear resistance as a function of initial bulk hardness with pure annealed, cold worked and heat treated steels follow a linear relationship [91].

In general, the wear resistance of steel does depend on its hardness, but also on the microstructure features and toughness [96]. A number of studies have shown that when the steel has same composition, the harder the steel, the greater the wear resistance because the harder steel matrix does a better job of holding on to the carbides. Whereas, when the steel has a different composition, the more carbides are included the better wear resistance of steels [96-99]. For example, a non-linear relationship between wear resistance and bulk

hardness was observed in a tumbler-based impact-abrasion test, where the microstructure and toughness also affect the wear resistance [100]. According to these studies, the hardness does have a certain effect on the wear resistance but does not guarantee a better resistance to wear.

2.7.2 Temperature

Researches on the influence of temperature on the wear behavior are usually studied as two aspects: (a) the effect of the ambient temperature during wear, and (b) increase in temperature due to plastic deformation of worn surface by friction heat. Generally, the wear rate and coefficient of friction (COF) are typically found to decrease as the temperature increased over a relatively transition temperature. Also the wear rate of medium carbon and stainless steels is found to decrease over an order of magnitude with a decrease in the COF of approximately 20%–30% [101-102]. Most of the heat generated at high strain rate remains within the deformed metal with the small time of contact between an individual grit and the substrate. As a consequence, the deformed worn surface is transient thermal softened due to the hardness reinforced by grit.

In general terms, the mechanical and metallurgical properties such as strength and ductility of the sliding surfaces could be modified by the increasing temperature. Moreover, the precipitation, strain ageing, and recrystallization are also caused by the varied behaviour accompanied with the structural changes [104]. Hurricks [105-106] carried out the oxidation changed from logarithmic to parabolic growth during the transition and the growing predominance of Fe_3O_4 within the oxide film (rather than α Fe_2O_3 which was thought to be the dominant oxide below the transition temperature). The role of iron oxides on the oxidational wear were studied by Lou et al. [103] who used a reciprocating tribometer to conduct the dry and lubricated sliding tests on carbon steel. It was observed the formation of different types of iron oxides within the sliding contact surfaces may contribute to the improved wear properties. Fe_3O_4 layers were considered as protective layers due to their strong adhesion to the sliding surface, and when Fe_3O_4 became the dominant constituent of the tribolayers, a reduction in wear loss was found. However, Fe_2O_3 layers may be removed more easily from the surface leading to abrasive wear

40

because of the debris particles [156-159]. Kayaba and Iwabuchi [102] simulated the reduction in wear and COF with increasing temperature with the change in oxide from α-Fe_2O_3 to Fe_3O_4. The formation of Fe_3O_4 due to the reduction of wear rates and COF with elevated temperatures can be considered act as a better solid lubricant adhere and more strongly to the surface than α Fe_2O_3 [107-108].

2.7.3 Lubricant

Lubricants introduced to effectively reduce friction between surfaces during the sliding contact which ultimately reduces the heat generated when the surfaces move. It can be classified into three different types as liquid such as oil, semisolid (greases), and solids such as graphite, molybdenum disulfide, boron nitride etc. The lubrication regimes are distinguished as three major categories: boundary, hydrodynamic and mixed:

Boundary lubrication typically occurs in applications with slow movement and/or high loads such as conveyor chains or gear boxes. In this regime, opposing surfaces that previously were in full contact with each other at rest are now starting to move. To prevent wear within this regime, lubricants are specifically formulated to form a low-friction, protective layer on the wear surface. Hydrodynamic lubrication involves the separation of two contacting surfaces using hydraulic forces. This typically occurs in rotating equipment, inside the journal bearings that support rotating shafts. Mixed lubrication is a transitional regime situated between boundary and hydrodynamic lubrication, sharing characteristics of both. Typically, mixed lubrication can occur during the startup of rotational equipment, as the shafts gain rotational speed from a full stop. It also can occur between surfaces where low loads and high speeds are encountered, such as when reciprocating pistons slide against piston walls. With this transitional regime, wear protection depends on both the lubricant viscosity as well as the additives within the formulation [109-110].

The operating conditions such as speed, loads, pressures and temperatures must be considered in order to obtain the better wear performance. But it is also important to choose the right lubricant for the application to control friction and wear. An inappropriate lubricant may result in significant friction, wear and even equipment failure. Meanwhile, a

proper choice of lubricant can lead to process efficiency increased and the life of components extended, and also oil consumption reduced in the automotive industry.

2.7.4 Environment

The wear rate varies with different atmosphere and moisture content of the environment. Under the air condition, the iron-rich oxidized tribolayers formed on the surfaces of the samples are easy to spall. Yen and Ishihara [112] investigated the effects of humidity on the friction and wear. Saravanan [111] investigated wear mechanisms in commercial purity argon tested which results in a more stable and homogeneous layer formed on the surface compared to the material tested under an oxygen atmosphere. Brainard and Buckley [113] conducted the wear tests under a range of pressure from 10^{-6} to 10^{-7} Torr. Gravie [114] performed dry sliding wear experiments in the vacuum and air environments, with different humidity levels. Goto and Uchijo [115] revealed the relationship between the wear behaviour and relative humidity (RH).

CHAPTER 3

EXPERIMENTAL DESIGN AND PROCEDURES

3.1 Experimental Materials

3.1.1 1045 steel

1045 steel is a family of AISI steel grades, as specified by the American Iron and Steel Institute (AISI). The 1045 steel in the as received condition shows hypoeutectoid phases, pearlite embedded in a proeutectoid ferrite matrix. The chemical composition of the 1045 steel used in this research is described in Table 3.1. It is a steel with good weldability, good balance between strength and ductility, and can be hardened through of the thermal treatments.

1045 steel is a medium carbon steel, which is widely used in industry for structural, tooling and advanced automotive parts. This grade is used for applications requiring more strength and wear resistance than can be obtained from low carbon mild steels. Examples of applications for 1045 steel include hydraulic rams, rail clip, shafts, gears and medium to higher strength threaded fasteners. 1045 steel is generally not recommended for critical applications, particularly those where high strength is required in combination with ductility or toughness. The steel needs to have a high surface hardness to obtain the necessary wear resistance. Therefore, flame or surface treatments, such as induction hardening is a very important process for achieving a suitable surface hardness for wear resistance applications (Lakthin, 1979). Moreover, the gas nitriding and electrochemical boriding processes can also be used to case harden 1045 steel.

Table 3.1 Typical chemical compositions (wt%) of AISI 1045 steel [116].

Element	C	Si	Mn	P	S	Cr	Ni	Fe
Weight %	0.49	0.20	0.81	0.013	0.022	0.17	0.10	Balance

3.1.2 Surface treated 1045 steel and geometry

Currently gas nitriding is being applied to medium carbon steel to increase the hardness and the wear resistance in automotive applications. Also an alternative surface hardening method called as "CRTD-Bor" (Cathodic Reduction and Thermal Diffusion based Boriding) was introduced for heavy-duty applications of medium carbon steel [117]. The main idea behind these treatments is to increase the surface hardness, as well as wear resistance hence these parts can have longer service lives. But these two surface treatments require an additional handling and processing step which adds cost and time to the manufacturing process. In this study, the gas nitrided and electrochemically borided 1045 steel were tested with the normalized and heat treated 1045 steel to compare their tribological behaviour.

Normalized and gas nitrided 1045 steel samples used in this study were obtained from Litens automotive company, and electrochemical borided 1045 steel samples were prepared at the Istanbul Technical University. The wear samples were prepared as steel blocks with the dimensions of 10 mm×10 mm ×5 mm, as shown in Figure 3.1(a), and all wear tests were conducted on the same flat surface (no corner or edge effects).
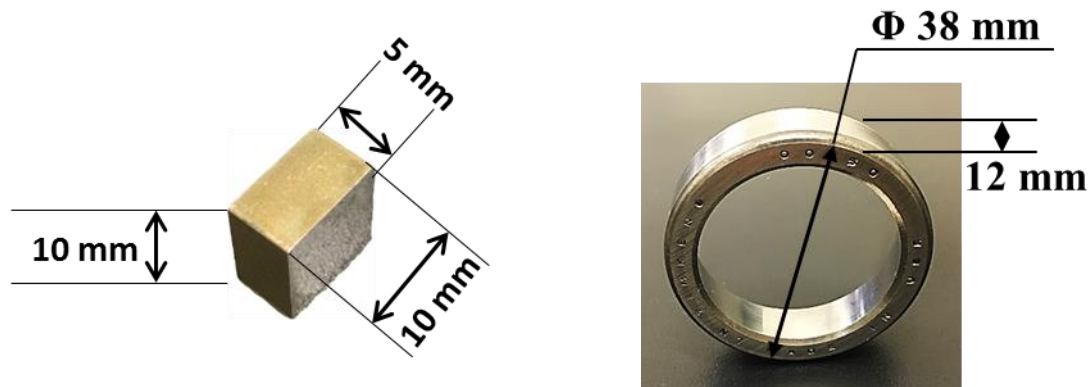
(a) The dimensions of 1045 steel block sample   (b) The dimensions of 52100 steel ring

Figure 3.1 Photographs of (a) as received 1045 steel, (b) 52100 steel samples with dimensions.

AISI 52100 grade steel is a high-carbon chromium bearing steel which was used as counterface material in this study as shown in Figure 3.1(b). 52100 bearing steel is a special steel with features of high wear resistance and rolling fatigue strength [118]. The as received 52100 steel shows hypereutectoid phases consisting of austenite grains with proeutectoid cementite. The chemical composition of the 52100 steel used in this research is given in Table 3.2 [119]. The 52100 steel was purchased in the form of bearing cages from Timkens with an outer diameter of 38 mm and a thickness of 12 mm, and was used as the counterface material against the 1045 steel blocks.

Table 3.2 Typical chemical compositions (wt%) of AISI 52100 steel [119].

Element	C	Si	Mn	P	S	Cr	Fe
Weight %	0.98-1.10	0.15-0.35	0.25-0.45	0.025	0.025	1.30-1.60	Balance

3.2 Induction hardening procedures

3.2.1 Heat treatment design

The objective of heat treating 1045 carbon steel is to increase the surface hardness and wear resistance of steel without the growth of cracks and without reducing its ductility. Induction surface hardening used for this purpose is a type of heat treatment method where only a working surface layer of the steel element or its selected part is heated inductively and then immediately cooled by immersing it into a quenching medium or by spraying. The short heating period aids in austenite grain size control, resulting in improved mechanical properties of the hardened component. There is minimal distortion and decarburization as a result of the short time between heating and quenching. As a result, a thin surface layer with required values of hardness and microstructure is obtained [120-124].

The heat treatment process was designed according to the continuous cooling transformation (CCT) diagrams with cooling curves as shown in Figure 3.2 [127]. This diagram shows the austenite transformations and the microstructures obtained at the end of heat treatments. For the continuous cooling of a steel, there exists a critical quenching rate (Vs), which represents the minimum rate of quenching that produces a 100% martensitic structure. For AISI 1045 steel, the critical quenching rate is 117.72 °C/s [125]. The quenched steel with high percentage of martensite is extremely hard but normally too brittle for practical uses. The internal stresses arising during quenching processes may cause cracks on the sample surfaces.

The temperature of heating and quenching also were determined by and A_{c3}, Bs and Ms temperature. A_{c3} is the critical temperature at which the ferrite phase is completely transformed into austenite by the heating process (heating temperature over A_{c3}). Bainite and martensite are achieved through an isothermal phase transformation process, and the highest isothermal temperature that allows bainite and martensite to be achieved, called Bs and Ms temperatures, usually are obtained through experiments for a given specific steel. The equations used here were determined by Trzaska [126] and are described as:

$$A_{c3} = 925 - 219\sqrt{\%C} - 17\%Ni + 39\%Si + 45\%V + 13\%Mo + 16\%Cr - 7\%Mn \quad (2)$$

$$B_s = 771 - 231.5\%C - 31\%Ni - 15\%Cr - 55\%Mo - 23\%Si - 69\%Mn - 58.5\%Cr \quad (3)$$

$$M_s = 541 - 401\%C - 18\%Ni - 15\%Cr - 17\%Mo - 10.5\%Si - 36\%Mn - 14\%Cr \quad (4)$$

According to equation (1), (2) and (3), the 1045 steel A_{c3}, Bs/Ms are obtained:

$$A_{c3} = 925 - 219 \times \sqrt{0.49} - 17 \times 0.1 + 13 \times 0.2 - 16 \times 0.03 + 16 \times 0.17 + 36$$
$$\times 0.81 = 785°C \ (1445°F)$$

$$1045M_s = 541 - 401 \times 0.49 - 36 \times 0.81 - 10.5 \times 0.2 - 14 \times 0.17 - 17 \times 0.03$$
$$- 18 \times 0.1 = 328°C \ (622°F)$$

$$1045B_s = 771 - 231.5 \times 0.49 - 69 \times 0.81 - 23 \times 0.2 - 58.5 \times 0.17 - 55 \times 0.03$$
$$- 31 \times 0.1 = 546°C \ (1015°F)$$
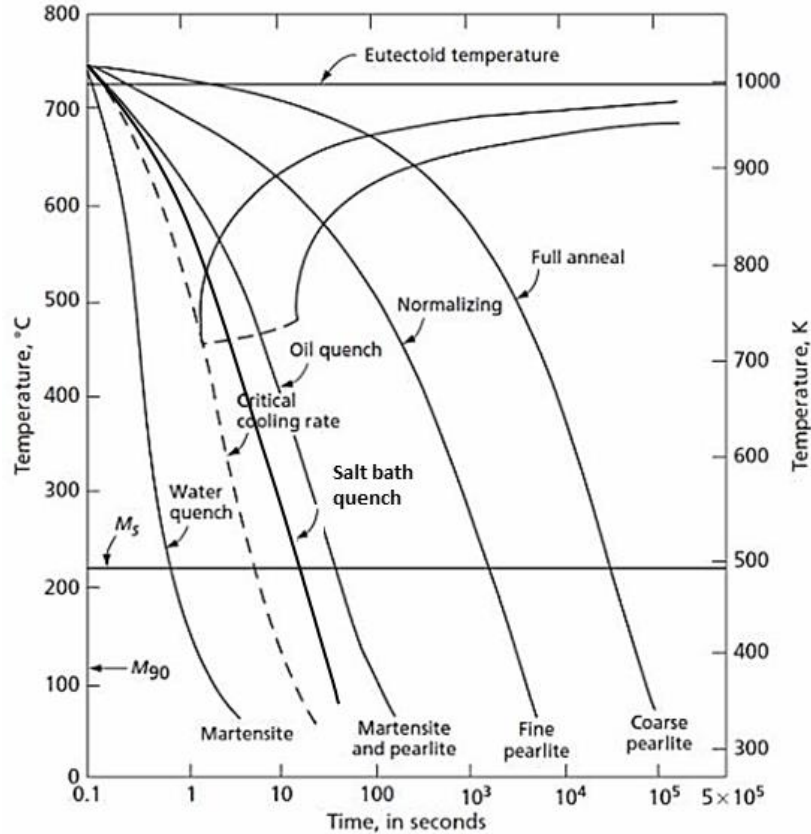
Figure 3.2 Typical Continuous cooling transformation diagrams(CCT) with cooling curves [127].

In order to obtain a uniform austenite microstructure. It is necessary to heat the samples to a temperature significantly higher than the traditional austenization temperature Ac_3. Also hardening relies primarily on the phase transformation resulting in the formation of a hard martensitic and bainitic layer. Therefore, the AISI 1045 steel will be heated over 785 °C for complete austenization, and the quenching cooling rate should allow the cooling curve through both bainitic and martensitic phases based on Bs (546 °C) and Ms (328 °C) temperatures.

3.2.2 Induction hardening procedures

Induction hardening processing of all the samples was carried out with a heat induction tool (High Power Bolt Buster) as shown in Figure 3.3. The details of the induction heater are: voltage: 110V, power: 1.8KW, frequency: 50-70KHz, current: 16A,

heating rate: 13.5ºC /s. Induction hardening furnace had a single-turn scanning induction coil. The induction coil had an internal diameter of 25.4 mm (1 in) and a face width of 6.35 mm (0.25 in). Figure 3.3(b) shows the induction coil set-up, and Figure 3.4 shows the Scilogex digital hotplate with Scilogex PT1000 Sensor (to control the medium temperature) to heat the sample to the target temperature. The coupling distance between the sample and the induction coil varied from 5.2 mm (0.205 in) to 1.7 mm (0.067 in) during the hardening process. The induction surface hardening process consisted of two consecutive stages with a short break between them. First the hardened component was heated inductively as quick as possible to 820 °C. Then, after a short break necessary for switching off and removing the inductor, the element was immediately cooled by the following quenchants: water, quenching oil (Super Quenchall Quench Oil) and a salt bath (40% NaOH + 60% KOH) that were maintained at temperatures of 60 °C, 160 °C, 280 °C, respectively. Table 3.3 summarizes the quenching media and time, temperature conditions used for induction hardening of 1045.

Table 3.3. Quenching media and conditions of temperature and time.

Quenching medium	Temperature (°C)	Quenching time (s)
Water	60	10
Salt bath (40% NaOH+60% KOH)	280	10
Quench oil	160	15

The detailed processing parameters of induction hardening as mentioned above are shown in Figure 3.5, and the heat treatment cycle curves are plotted based on the designed process of induction hardening as shown in Figure 3.6. The as-received AISI 1045 steel samples were heated using induction heating method up to an austenite temperature of 820ºC, held at this temperature of 120s, then immediately quenched in the following modes: i) water at 60 °C, ii) a salt bath composed of 60% KOH and 40% NaOH at 280 °C and iii) quenching oil at 160 °C holding for 10-15 seconds. After quenching the samples were air cooled to room temperature.

(a)   (b)
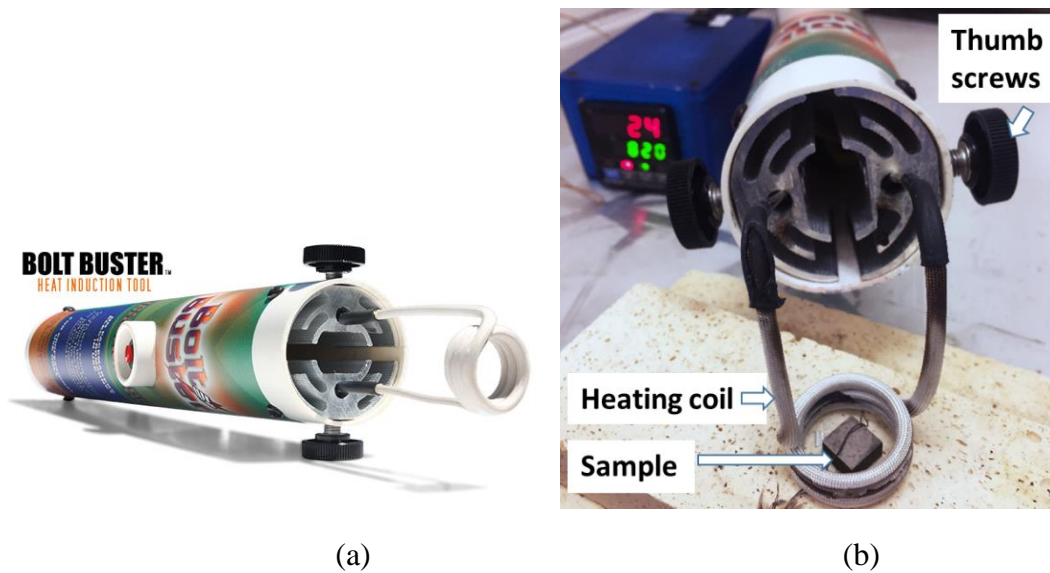
Figure 3.3 Induction heating tool – Bolt Buster, (a) overall view, (b) heating set-up.
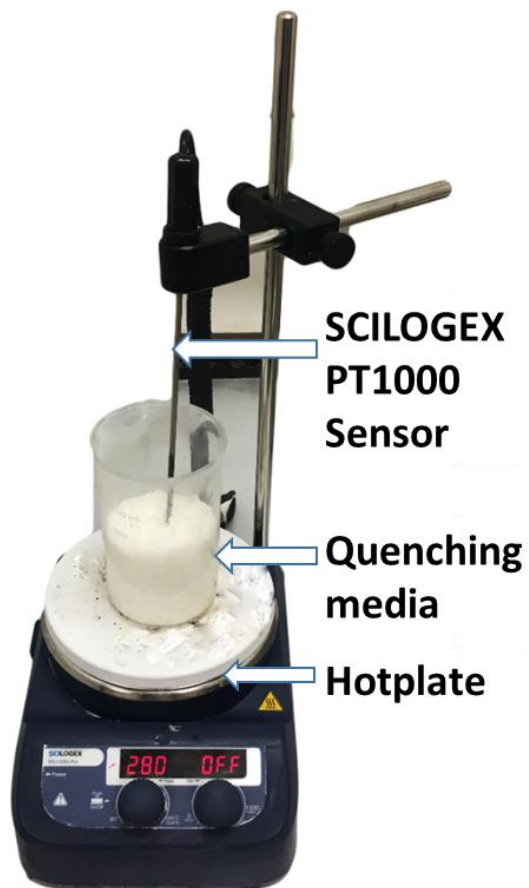
Figure 3.4 Heating set-up: Scilogex digital hotplate with Scilogex PT1000 Sensor.
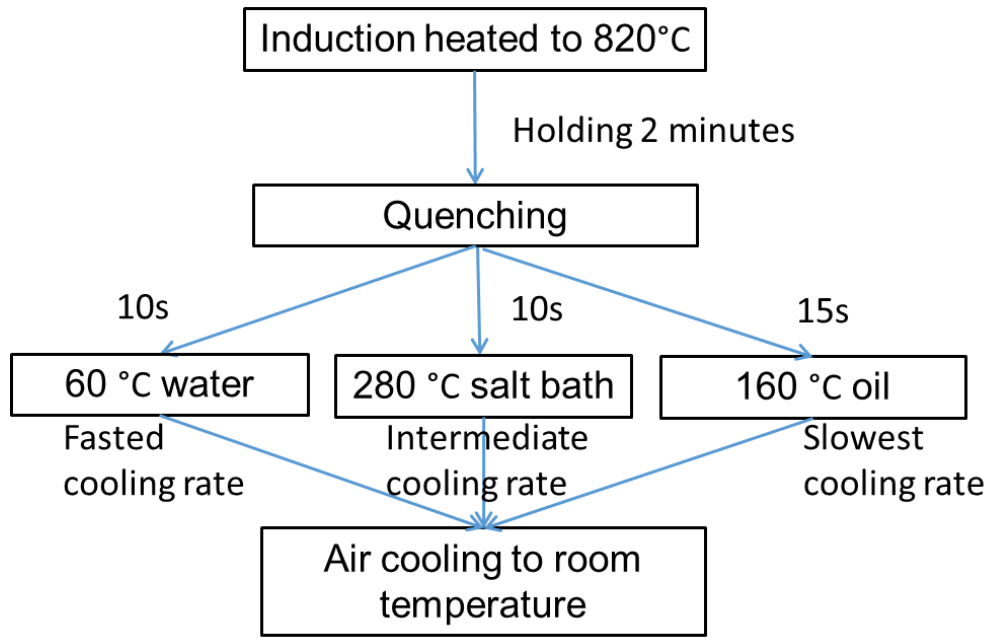
Figure 3.5 Heat treatment process.
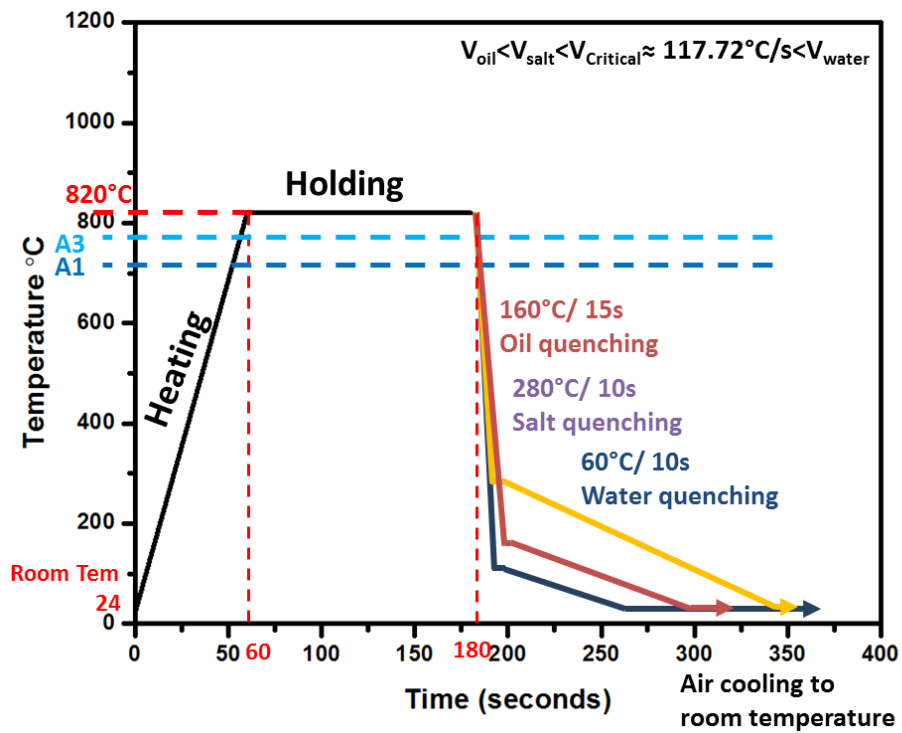
Figure 3.6 Heat treatment cycle curves of 1045 steel.

3.3 Tribological test

3.3.1 Dry and lubricated sliding wear tests

The Block-on-ring test is a widely used technique that evaluates the sliding wear behaviour of materials under controlled conditions and allows reliable ranking of material couples for specific tribological applications. Figure 3.7 illustrates a schematic diagram of the block-on-ring wear test apparatus.
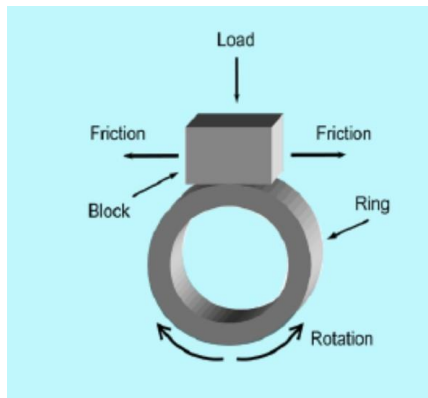
Figure 3.7: Schematic illustration of block-on-ring wear test apparatus.

In this study, the sliding wear tests were performed on untreated, heat-treated, gas nitrided and electrochemical borided 1045 steel blocks against AISI 52100 steel ring at dry and lubricated conditions using a block-on-ring tribometer as shown in Figure 3.8. The surfaces of block samples and counterface were ultrasonically cleaned using ethanol before each wear test. To realize a sliding speed of 1 m/s, the rotational speed was fixed at 500 RPM. Thereafter, the ring and the samples were fixed in the tribometer. The weights were placed on the tray and fixed carefully. The sliding wear tests were performed at a constant load of 44.48 N with six different sliding distances, i.e., 500 m, 1,000 m, 3,000 m, 5,000 m, 10,000 m, 15,000 m at room temperature under dry and lubricated conditions.

The lubricated tests were performed with the two types of grease-like lubricants: Peerless LLG (a calcium sulphonate complex thickened grease) and Krytox (perfluoropolyether (PFPE) grease), both are widely applied in automotive and industrial equipment such as bearings and chassis due to their oxidation stability, wear resistance,

rust protection and excellent load carrying ability. Figure 3.8(a) shows the steel ring is completely covered by the lubricants before the lubricated sliding wear start, and at the end of the test the condition between block sample and ring is presented in Figure 3.9(b). The lubricants were provided by Litens automotive company.

(a)   (b)
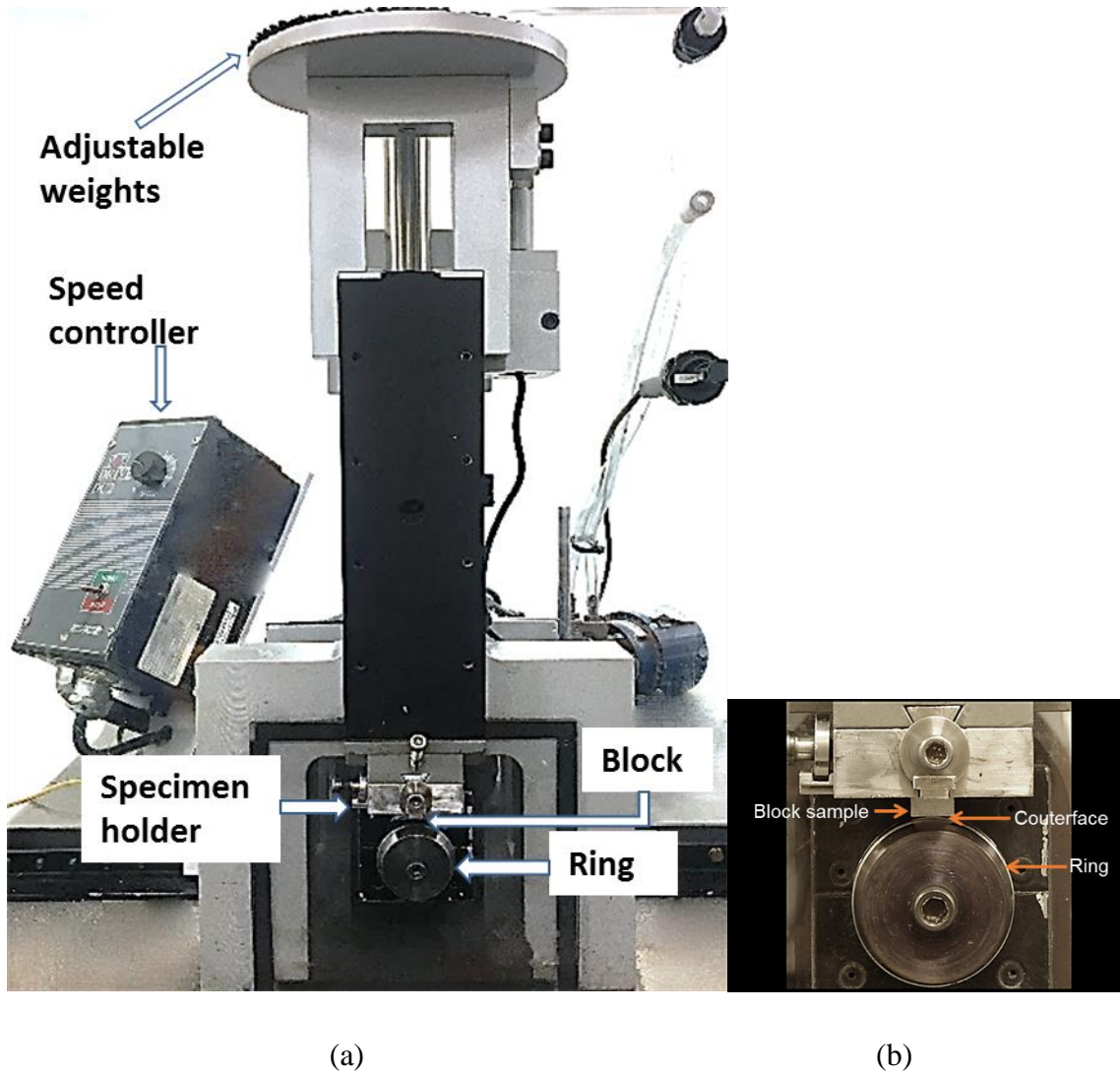
Figure 3.8 (a) Block-on-ring tribological machine (b) Enlarged figure showing the block-on-ring configuration
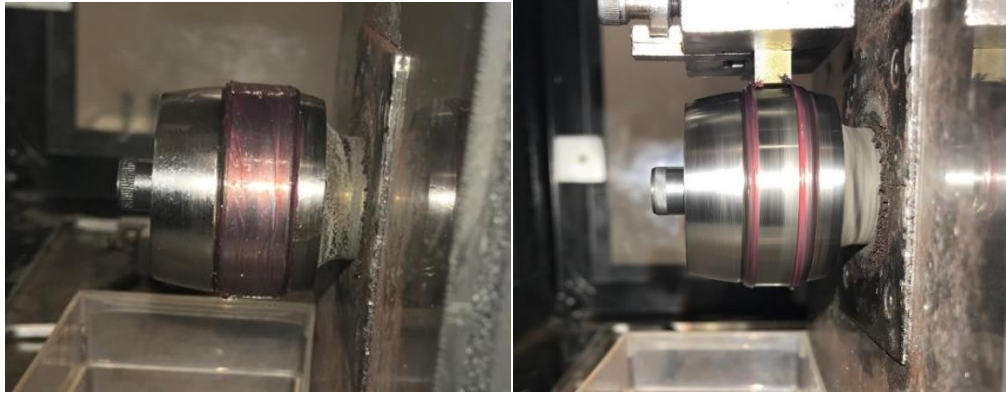
<div align="center">(a)   (b)</div>

Figure 3.9 Lubricant applied in the block-on-ring sliding wear test, (a) before the test, (b) after the test.

3.3.2 Humidity sliding wear test

The humidity sliding wear tests were designed for examining the influence of the environmental humidity present during sliding wear test caused the boric acid film generated, which resulted in the increase of the wear resistance. The boric acid film (H_3BO_3) was expected to be generated due to the spontaneous reaction between the boron oxide and relative humidity in the environment.

Erdemir et al. [129] conducted the 800 °C annealing process on the B_4C substrates to produce the B_2O_3 surfaces and wear tests in 40 %-50 % relative humidity (RH). The results suggested that the formation of a boric acid (H_3BO_3) film on B_2O_3 surfaces can greatly reduce the friction coefficients as low as 0.03 to sliding metallic and ceramic interfaces. Sanchez et al. [128] studied the effect of relative humidity on the self-lubricating properties of a thin film of boric acid film, and they applied the short annealing process (SAP) at 750 °C for 5 min and cooled to room temperature in 20 %-85 % relative humidity (RH) on AISI 316L steel to form a compact boric acid film. The results showed the best RH condition for the formation of H_3BO_3 film for 316 L steel is 60% RH.

According to the researches mentioned above, there are two criteria required to form boric acid film: one is a sufficiently high temperature (over 750°C) for oxidation to

generate the formation of boron oxide (B_2O_3); the other is appropriate relative humidity (over 40%) to create the environment for generation of (H_3BO_3) film.

Therefore, part of borided samples were heat treated with a short annealing process (SAP) and cooled in the controlled RH before the wear test to form a boric acid film. The borided samples were firstly cleaned to remove impurities remaining from the boriding process, and then heated with SAP in a conventional furnace at 750°C for 5 minutes in open air. After the SAP, the samples were cooled to room temperature in a controlled moisture chamber at 40% RH. Humidity wear tests were also performed on the block-on ring tribometer with borided blocks against 52100 rings in a controlled moisture chamber as shown in Figure 3.10. The wear tests were conducted at a speed of 1 m/s and a constant load of 44.48 N at room humidity of 25% (RH) after 1000 m sliding distance.
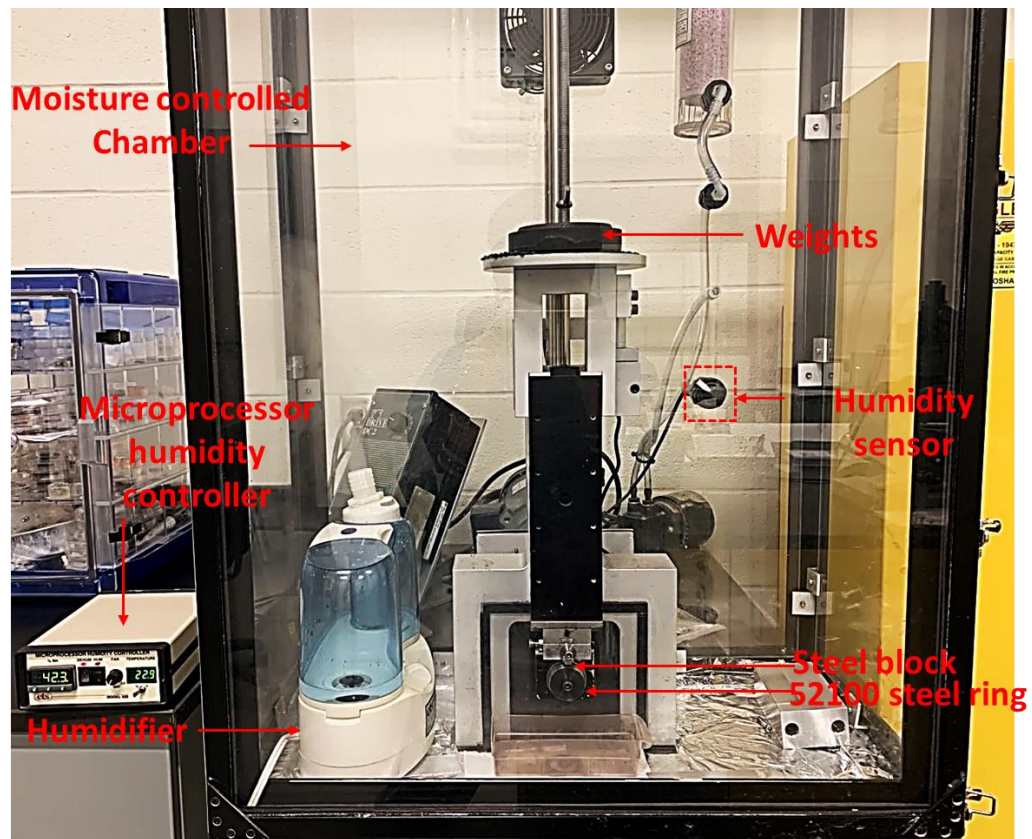
Figure 3.10 Block-on-ring tribometer with humidity controller.

3.3.3 Wear rate

The wear volume loss is the main critical factor to present the wear resistance of metal material. Weighing mass loss was applied to the calculation of the wear rates for significant amount of wear loss. Before and after each test, an analytical balance with an accuracy of 0.1 mg was fixed to measure the mass of the samples. After removing the loose debris from the worn surfaces in an ultrasonic cleaner with ethanol, the mass of the worn samples was measured. Then the wear in mass loss (M) was converted to volume loss (V) using the density (ρ) of the material according to the equation:

$$V = \frac{M}{\rho} \tag{5}$$

For mass losses less than 0.1 g, for example lubricated wear loss, volumetric wear losses were measured using optical profilometer (WYKO NT-1100). Optical profilometry calculations were employed to determine the material removal rates in the composites according to the reference [130]. The amount of material removal associated with the groove formations along the wear track were detected in this way. The worn area was calculated using optical profilometry observations, with four readings from each image (Figure 3.11), where the area beneath the reference line was calculated to be the worn area. An average of 24 readings (from six different regions of the wear track) were taken as the worn area A_{ij} and was multiplied by the perimeter of the wear track, which gives the volumetric wear loss V according to the equation (6) [36]:

$$V = \frac{2}{n}\pi Rw \left[\sum_{i=1}^{n} \sum_{j=1}^{k} Aij \right] \tag{6}$$

where, k is the number of grooves per section and n=24: the number of different sections along the wear track from which measurements were made.
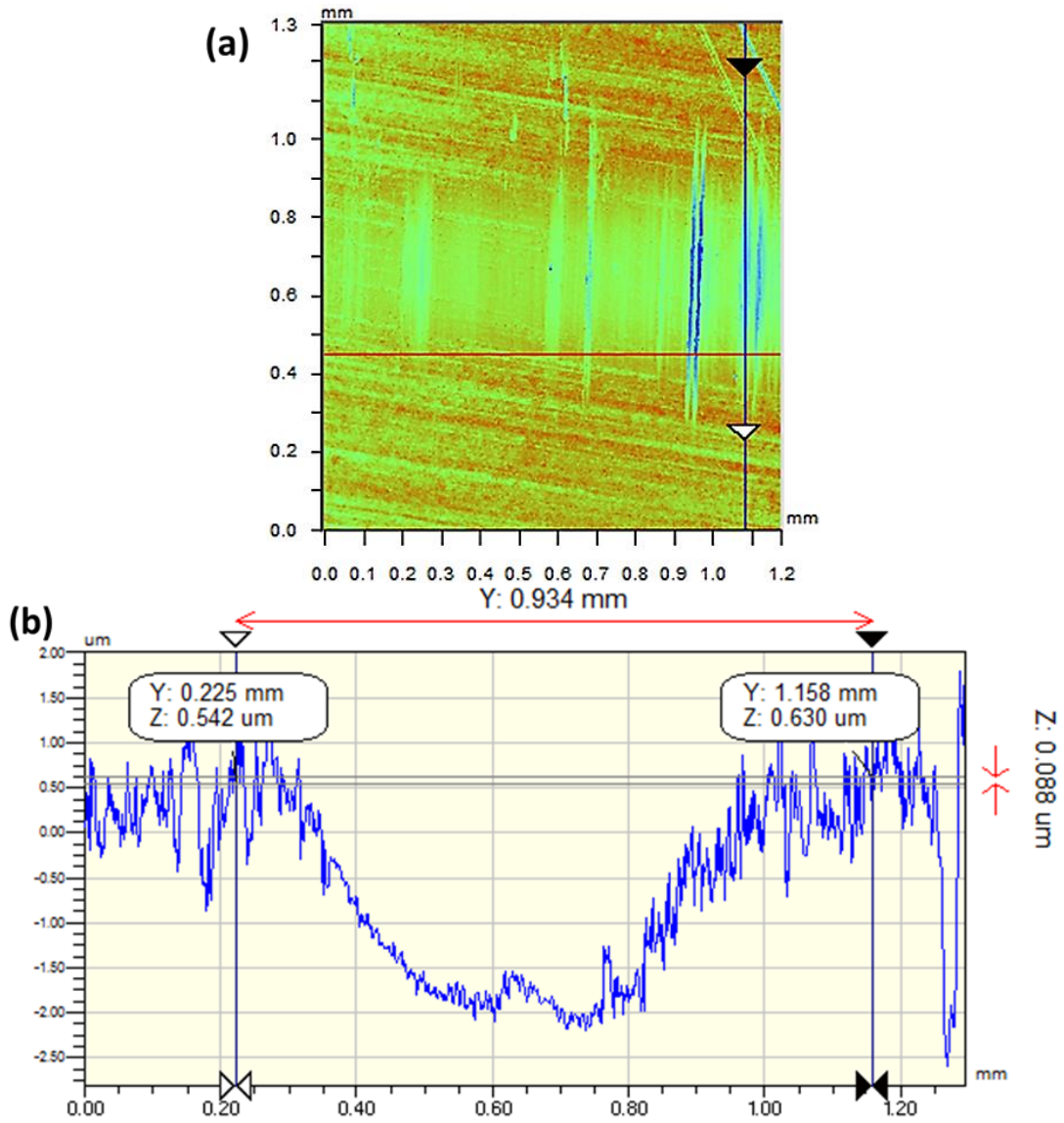
Figure 3.11 Optical profilometry image (a) and Y profile (b) for worn surface of 1045 steel block samples after sliding wear test, (b) Y file.3.4 Material characterizations

Finally, the volumetric wear rate (W) was calculated from the slopes of the volumetric loss (V) vs. sliding distance (S) curves. The following equations show the methods of calculating the volume loss and the wear rate:

$$W = \frac{V}{S} \tag{7}$$

According to Archard's law [131], the wear rate (W) is related to the applied load (P), the wear coefficient K and the hardness of the material (H):

$$W = \frac{KP}{H} \tag{8}$$

The wear coefficients of samples in different conditions were calculated based on this equation.

3.4.1 Optical metallography

The cross-sections of untreated and surface treated 1045 steel before and after sliding wear tests were prepared for optical microscopy observation to reveal microstructures by polishing and etching. After mounting in plastic, ground on a series of SiC papers (240, 400, 600, 800, 1200 grit), they were polished with 1.0μm and 0.5μm Al_2O_3 powder on a Buehler polisher, and then etched by 4% Nital solution (ethanol + nitric acid) for around 10s. All of the surfaces to be examined were polished to a mirror finish and then cleaned with water and 95% ethanol liquid before and after etching. All of the optical microscopy work was performed using a ZEISS Axio Vert. A1 microscope with the magnification in the range ×50-×500. There are four possible illumination modes available in the ZEISS Axio Vert. A1 microscope: bright field, dark field, Differential Interference Contrast (DIC), and fluorescence contrast in reflected light. For microstructural characterization of 1045 steel, the method of reflected light bright field is the most appropriate illumination to analyze the microstructures of etched surfaces.

Related software, The ImageJ Software was used to isolate and measure the area percentage of bainite, martensite or retained austenite phases in the different microstructures. The determination of area percentage was based on color difference. The bainite content was also measured by the contrast differences between the martensite and other colored areas. Thus the threshold setting was especially important for obtaining an accurate result. Because there is a strong contrast difference between the bainite and the matrix, this content is readily calculated. Figure 3.12 shows the detailed steps in

determining the bainite content of an etched sample using ImageJ software. The threshold was adjusted by two sliders, the upper slider adjusted the minimum threshold value and the lower one adjusted the maximum as shown in Figure 3.12(b). The bainitic area will be selected while the minimum to move a fixed-width thresholding window across the range of gray values.
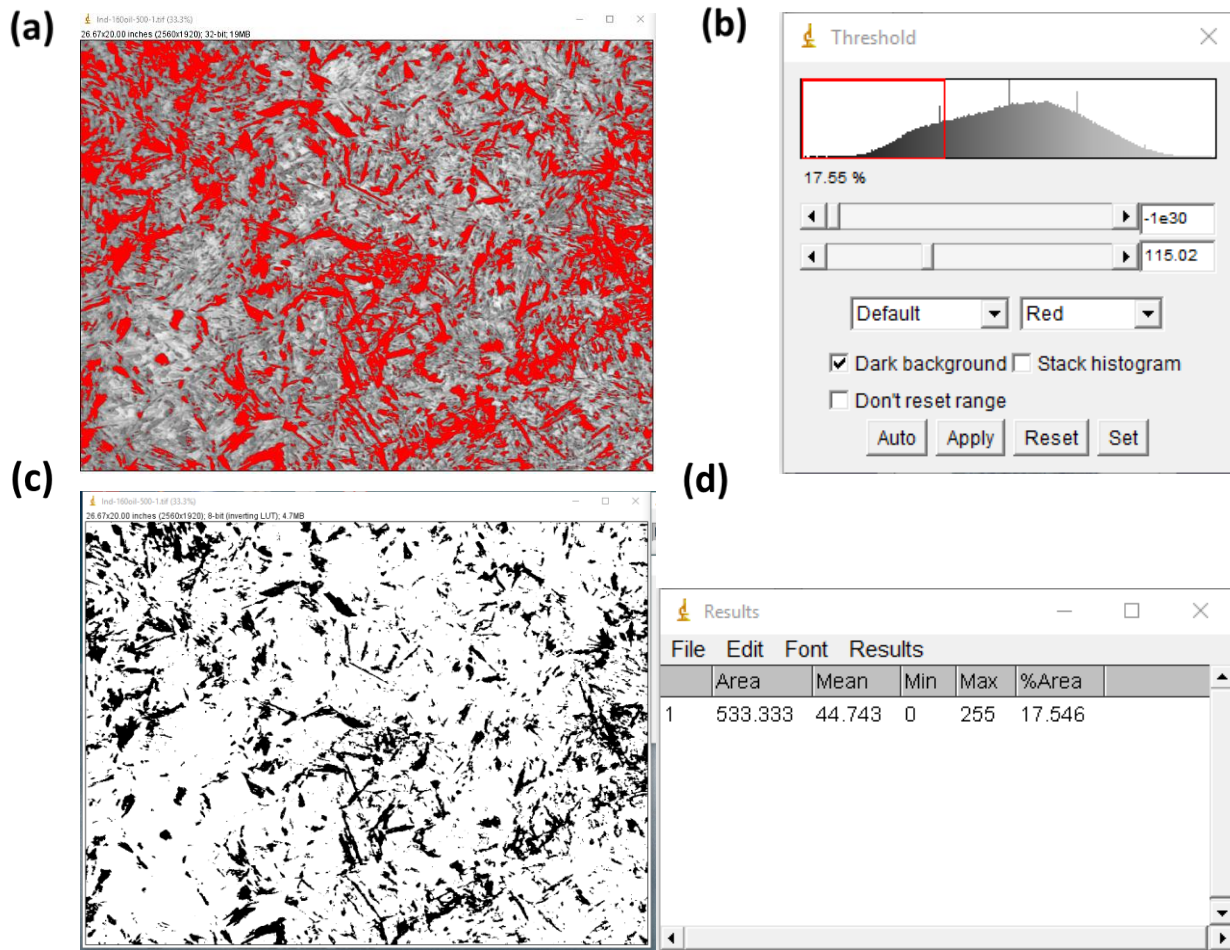
Figure 3.12 Steps showing how to determine phase content in ImgeJ (a) adjust the type of the image from bright field to the 32-bit and then select the colour of Bainite (dark); (b)Adjust threshold   to segment the image into features of bainite and other microstructures;(c) Measure the selected area (d)Measurement results of selected area.

3.4.2 Scanning Electron Microscopy (SEM)

The details of surface and subsurface microstructures as well as worn surface morphologies were investigated using a FEI Quanta 200 FEG scanning electron

58

microscope (SEM) equipped with an energy-dispersive X-ray EDAX (SiLi Detector) spectrometer. The system is structured with a single user interface window that allows for flexible and versatile analysis. This interface allows switching between the SEM image mode and the EDS analysis mode easily. EDS was used on the wear tracks to quantitatively assess the composition at selected locations.

3.4.3 Surface Roughness Measurements

The surface roughness values and the outlines of the worn surface were carried out using a non-contact, optical surface profilometer (WYKO NT-1100), which provides high resolution and 3D surface measurement capability, from sub-nanometer roughness to millimeter-high. The WYKO profilometer as shown in Figure 3.13 measures the profile of a solid surface using the principle of optical interferometry.

Figure 3.13: Optical surface profilometer (WYKO NT-1100) for roughness measurement

There are two methods for the measurement, Phase-Shift Interferometry (PSI) and the Vertical Scanning Interferometry (VSI) mode. In the present study the roughness of the surface was measured using the VSI mode instead of the PSI mode due to the rough surfaces of samples. The important parameters of surface texture are listed in the following:

S_a is the average roughness serving as a good general indication of smoothness, S_q is the root mean square height of the roughness, S_z is the ten-point height, S_k is the core-roughness depth, S_{pk} is the reduced peak height, S_{vk} is the reduced valley depth, M_{r1} and M_{r2} are the peak and valley material component obtained from the bearing ratio plot. The parameters analyzed in this study were measured at five different places and averaged out.

3.4.4 Micro-hardness Test

The micro-hardness was measured using a Buehler Micromet II micro-Hardness tester with a load of 50 gf (0.49 N) as shown in Figure 3.14. It was equipped with an optical microscope and measuring tools. With the microscope the indentation can be applied at specific desired points or phase, such as the compound layer and the pearlite or bainite phase in the matrix.

Figure 3.14 Buehler Micromet II micro-Hardness tester

The Vickers Diamond Pyramid microhardness value is the applied load (kgf) divided by the surface area of the indentation (mm^2) using equation (8):

$$HV = 1.854 \frac{P}{d^2} \tag{9}$$

Where HV=Vickers hardness; P=Load in kgf; d=Arithmetic mean of the two diagonals in mm. The dwell time is 12 s, and each hardness data is the average of seven measurements of the surface. The distance between the two adjacent indentations was more than three times the length of the indentation diagonal.

3.4.5 Oxide phase analyses

The composition of oxide phases formed on worn surfaces due to the thermal oxidation during sliding tests was determined using a light scattering Raman micro-spectrometer (Horiba) equipped with a 50 mW Nd-YAG 141 solid state laser (532.0 nm excitation line) and a ×50 objective lens of the spectrometer having a laser spot diameter of 1 μm and focused on the wear track. Raman spectroscopy is a spectroscopic technique commonly used to identify the molecules by featuring a number of peaks, showing the intensity and wavelength position of the Raman scattered light. Each peak corresponds to a specific molecular bond vibration, including individual bonds and groups of bonds.

CHAPTER 4

HEAT TREATMENT RESULTS AND ANALYSES

4.1 Overview

In this chapter, results are presented for the microstructural observation and characterization of the gas nitrided, electrochemical borided and induction hardened 1045 steel using light optical microscopy (OM) and scanning electron microscopy (SEM). The qualitative and quantitative analysis were obtained from optical micrographs for bainite and the software image analysis. The results of surface roughness and surface microhardness of the induction hardened, nitrided and borided layers were also studied by using Vickers hardness tester and optical surface profilometery, as well as the cross-sectional hardness gradient and measurements for compound layer thickness and diffusion zone depth of the surface treated 1045 steel were obtained.

4.2 Optical metallography of induction hardened 1045 steel

4.2.1 Optical microstructures of heat treated and quenched samples

The optical microstructure of the as received 1045 steel before the heat treatment is shown in Figure 4.1, and primarily consists of a dark lamellar pearlite matrix surrounding bright ferrite grains. The size of the grains varies between 10 and 30 μm and the volume fractions of pearlite and ferrite is 60 % and 40 %, respectively. A series of images from Figure 4.2 to 4.4 show the optical micrographs of the induction hardened samples quenched in different media including salt bath, quenching oil and water. There are two images at 500x and 1000x magnifications that are presented for each sample. The lower magnification image is useful in understanding the overall phase distribution, while the higher magnification image is required to observe the detailed microstructure.

It can be seen from Figure 4.2(a) and Figure 4.3(a) that the microstructures of the samples quenched from 820 °C into a 280 °C salt bath and 160 °C quenching oil holding for 10 s. and 15 s consisted of martensite, retained austenite and a certain amount of dispersed bainite. The obtained microstructures are close to the prediction of CCT phase

diagram of 1045 steel since two new phases, namely bainite and martensite, were generated after quenching. Thus, it can be inferred that the cooling rates under these conditions were slower than the critical quenching rate of AISI 1045 steel. The bainite became dark after etching because the bainite/cementite interfaces were easily attacked by the etchant (5% Nital) used. The new phases were martensite which appeared to be lighter after etching because of the absence of carbide precipitates and white retained austenite. It is difficult to distinguish between bainite and martensite laths under the optical microscope, even though the bainite laths would be thicker, shorter, segmented and the edges have a feathery or saw-type profile. On the other hand, the martensite needles are much longer, narrower and have a smooth profile edge [132].
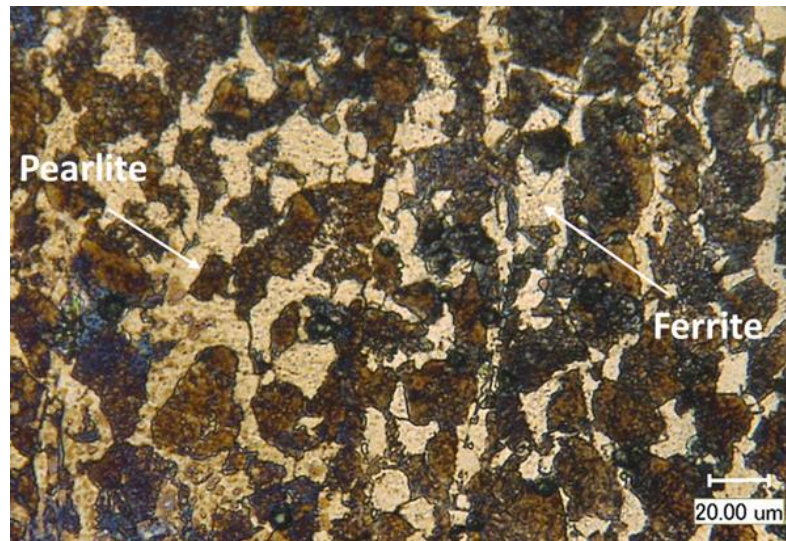
Figure 4.1 Optical micrograph of the untreated normalized 1045 steel.

After an isothermal holding time of 10 seconds in molten salt, some typical lath-like upper bainitic plates formed as shown in Figure 4.2(b). Upper bainite appears as broad, lath-like sheaves, and the lower bainite appears as the narrow, needle-like sheaves as shown in Figure 4.3(b). It can be seen that upper bainite and lower bainite mixed structures were formed in the oil quenched sample. Around this narrow transitional isothermal temperature range (250°C - 550°C), the mixed phases or microstructures may provide the desired mechanical properties for the steels heat treated this way. The start of nucleation of primary bainite grain was observed on the austenite grain boundaries. Parallel plates of ferrite often

occur in large groups, which represent the first stage of bainite formation. This final microstructure is called feathery bainite due to the appearance of ferrite plates [132].

Figure 4.4 shows that the microstructure of the sample quenched in water at 60 °C consisted of martensite and retained austenite. It can be assumed that the higher cooling rate due to in water resulted in the formation of acicular martensite, and reduction of the proportion of bainite. The water quenched sample was expected to present the higher hardness and better wear resistance among the heat treated samples due to the highest fraction of martensite. However, surface cracks were detected on this sample surface as shown in Figure 4.5 due to the high cooling rate, which causes thermal stress applied on the surface.
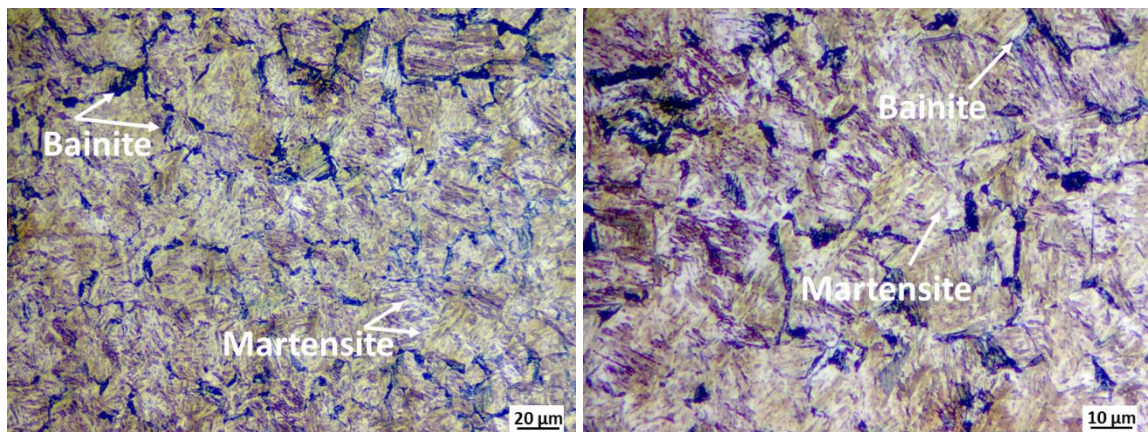
(a)   (b)

Figure 4.2 Optical micrographs (bright field illumination) of induction hardened sample quenched in 280 °C salt bath, (a) 500 X, (b) 1000 X (dark phase: bainite; lighter phase: martensite).
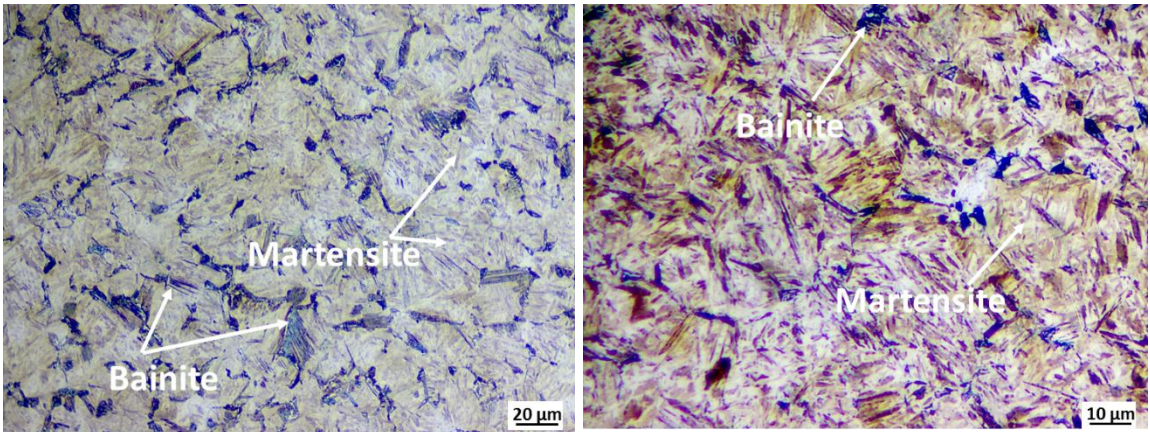
(a)   (b)

Figure 4.3 Optical micrographs (bright field illumination) of induction hardened sample quenched in 160 °C quenching oil, (a) 500 X, (b) 1000 X (dark phase: bainite; lighter phase: martensite).
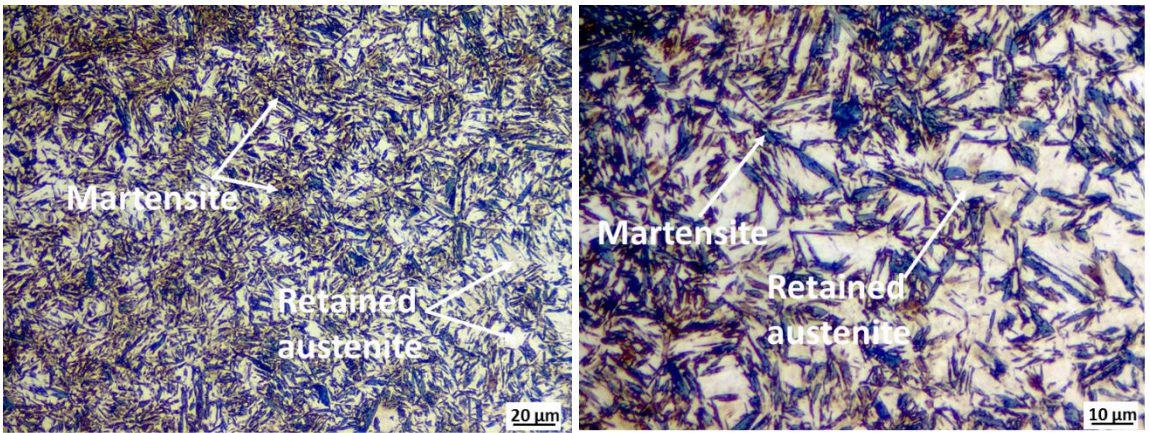
(a)   (b)

Figure 4.4 Optical micrographs (bright field illumination) of induction hardened sample quenched in 60 °C water, (a) 500 X, (b) 1000 X (dark phase: martensite; white phase: retained austenite).

65

Figure 4.5 Quenching cracks formed on the 60 °C water quenched 1045 steel.

4.2.2 Quantitative Analysis of Bainite content

The bainite phase amount, and shape may affect the wear properties. The lath-like, needle-like bainite were isolated on optical microstructures and measured using ImageJ software based on the contrast differences between the bainite, martensite or retained austenite phases in the different microstructures. Figures 4.6(a) and 4.7(a) show oil quenched sample and salt quenched sample for comparison. Both the samples were examined at 1000X magnification since this magnification image is useful in determining the bainite distribution according to the colour of the etched microstructure. The area fractions (bainite content) were obtained from the black and white pictures on the Figure 4.6(b) and 4.7(b). Ten images were used for each sample and an average value has been calculated. The results showed 13.4±1.3 % bainite in the microstructure of the sample quenched in salt bath at 280 °C, whereas the microstructure of the sample quenched in oil at 160 °C contained more bainite content at 19.5±1.5 %. The difference between the bainite content is due to the difference in cooling rate resulting from the quenching media. Under a lower quenching temperature (160 °C), the transformation of bainite starts earlier which results in a higher fraction of bainite since the cooling rate is a little higher than that in the 280 °C. Moreover, the area fractions of ferrite and retained austenite were also measured from the images, the salt quenched sample contained ferrite and retained austenite at content 7.7±1.0 % while more ferritic and austenitic structures were observed in the oil quenched sample around 8.6±1.1 %. The rest of area fractions were measured as martensite

content, the oil quenched sample contained 71.9±1.2 % martensitic structures while the content was obtained at 76.2±1.2 % in salt quenched sample.
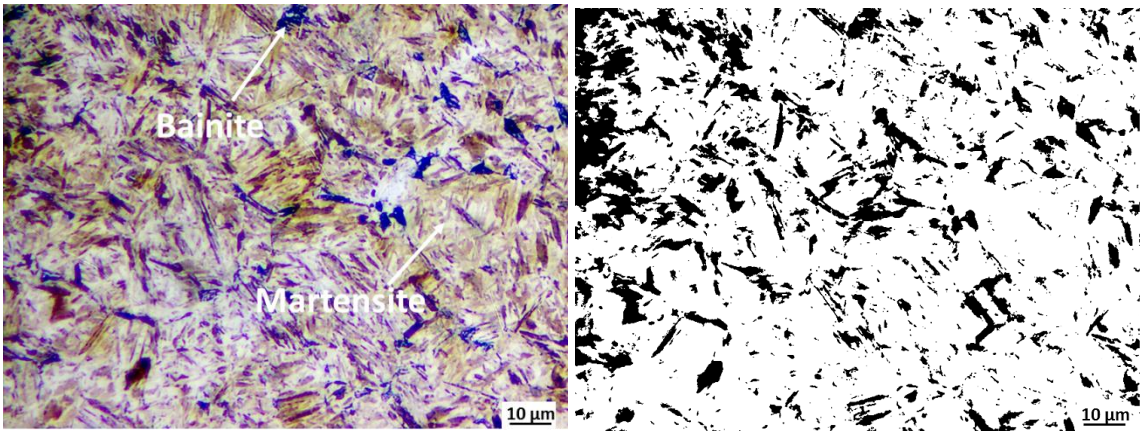
(a) Optical micrograph　　　　　　　　(b) After Image J software processing

Figure 4.6: Metallography of oil quenched samples, 1000X (a) optical micrograph, (b) after Image J software processing in (a) calculated average bainite content: 19.5 %.
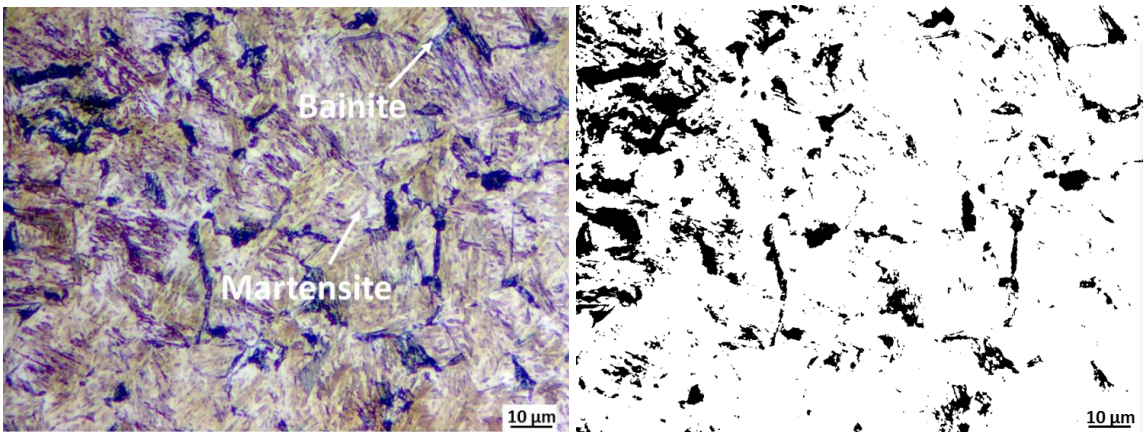
(a) Optical micrograph　　　　　　　　(b) After Image J software processing

Figure 4.7: Metallography of salt quenched samples, 1000X (a) optical micrograph, (b) after Image J software processing in (a) calculated average bainite content: 13.4 %.

4.3 Scanning electron micrographs of 1045 steel

4.3.1 Microstructures of heat treated and quenched samples

Figure 4.8 shows the typical microstructure of untreated 1045 steel consisting of pearlite and ferrite. The large grey areas are pro-eutectoid ferrite. Regions having the alternating light and dark lamellar structure are pearlite; the dark and light layers in the pearlite correspond, respectively, to ferrite and cementite phases. During etching of the surface prior to examination, the ferrite phase was preferentially dissolved; thus, the pearlite appears in topographical relief with cementite layers being elevated above the ferrite layers. Many cementite layers are so thin that adjacent phase boundaries are so close together that they are indistinguishable at this magnification.
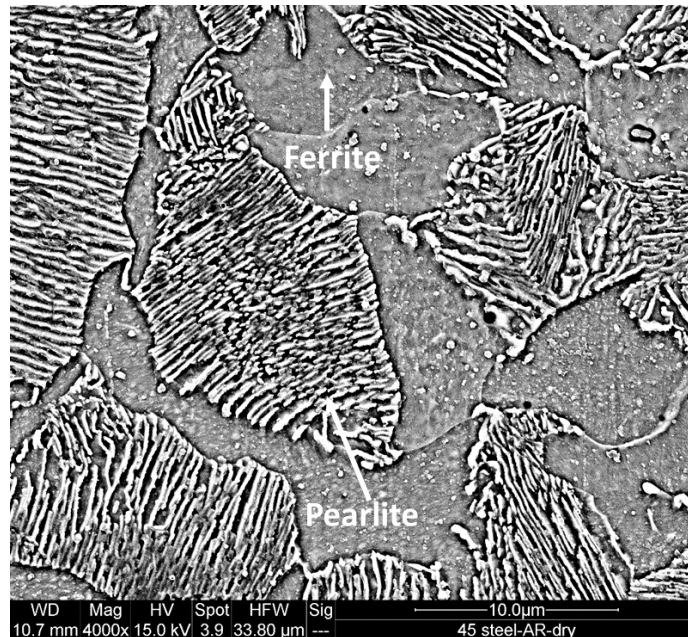
Figure 4.8 The SEM micrograph of initial ferrite-pearlite structure of AISI 1045 steel.

The bainitic microstructure can be better distinguished from other microstructures under SEM with larger magnification, and Figure 4.9 and 4.10 show the SEM micrographs of the induction hardened samples quenched in oil and salt bath. The typical microstructures of the mixed lower bainite-martensite and the upper bainite-martensite are observed respectively. The lower bainite consisted of tiny rod like white carbides aligned at an angle or along the direction of growth of ferrite grains.

68

It can be seen from Figure 4.9 that the lower bainite in mixed microstructures of lower bainite-martensite appears in narrow feathery form, but Figure 4.10 shows the upper bainite as broad, lath-like sheaves. The upper and lower bainite formed in different morphologies due to the different mechanisms based on which growth and nucleation occur at different temperatures. The growth of the upper bainite can be described as the movement of a low coherent ferrite/austenite interface which necessitates some degree of self-diffusion and leads to rather immobility of the interface [133]. Upper bainite is obtained when carbon migrates relatively rapidly into the residual austenite grains, before the carbides have an opportunity to precipitate. On the contrary, in the case of the lower bainite the propagation of a more coherent interface becomes possible and therefore, little or no self-diffusion required. This results in more rapid movement of the interface [134]. The formation of lower bainite caused by the carbon enrichment of the austenite because of the upper bainite transformation, therefore the mixed microstructure of upper and lower bainite is possible to form.
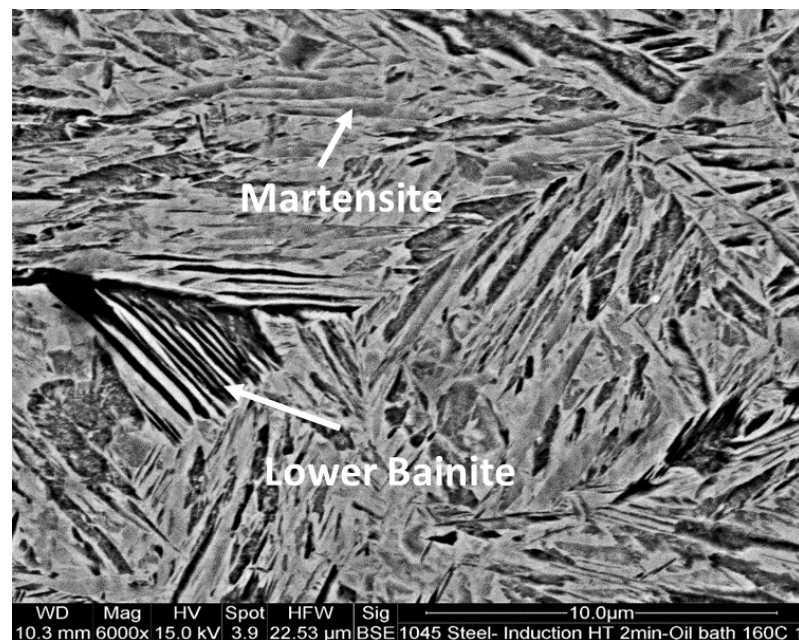
Figure 4.9 The SEM micrograph of induction hardened sample quenched in 160°C oil
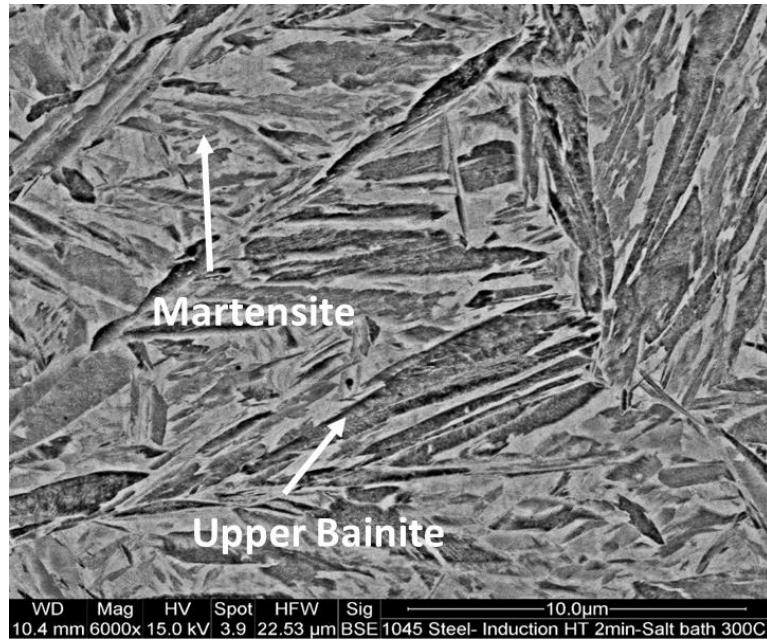
Figure 4.10 The SEM micrograph of induction hardened sample quenched in 280 °C salt bath.

4.3.1 Cross-sectional metallography

The typical cross-sectional micromorphology of the heat treated and quenched steel taken following the oil quenching and salt quenching are presented in Figure 4.11 and 4.12 respectively. There is no obvious heat affected zone (HAZ) to be found, and it can be observed that the micromorphology of the heat treated layer is uniform from the top surface to the core, which consists of the bainite, martensite and retained austenite. There is no obvious difference between the microstructures on the cross-sectional surface and that on the top surface which were discussed at section 4.3.1, where the oil quenched sample was consisted of feathery lower bainite and martensite, whereas the salt quenched sample was consisted of lath-like upper bainite and martensite.

The gas nitrided and borided samples were used as reference materials for their wear resistance in comparison with bainitic structures, and their cross-sectional microstructures taken under SEM are shown in Figures 4.13 and Figure 4.14 respectively. The microstructure of the nitrided subsurface is generally composed of a thin compound layer (CL) with a diffusion zone (DZ) underneath. Good wear resistance is usually ascribed

to the compound layer and the hardened diffusion zone [16]. Figure 4.13 shows CL and a porosity layer on the top and the microstructures of ferrite and pearlite containing nitrogen precipitations in the diffusion zone. The diffusion zone consists of an interstitial solution of nitrogen in the α-iron lattice and fine coherent and semicoherent nitride precipitates formed due to the strong interaction of nitrogen with the alloying elements present in the alloy [15]. It can be seen in Figure 4.13(a) the nitriding process did not cause any changes in the size or percentage of the pearlite and ferrite phases. Based on image analyses, the thickness of the compound layer was determined as 9 μm, while that of the nitrided layer was measured as around 150 μm.

Figure 4.14 shows the micrographs of the cross section of borided AISI 1045 steel, which reveal a typical microstructure of boride coatings with a multi-phase structure and flat morphology. There are four different zones can be observed in the borided region, i) the outermost zone is a FeB phase with high boron content; ii) the second zone which is dominated by Fe_2B phase; iii) a third zone is the region below the boride layers, which is called the diffusion zone., iv) the fourth region is the steel substrate, which is not affected by boron diffusion. It has been observed that the hardened depth of the continuously borided needles is not as the uniform as nitrided layer. The case depth of the continuously pack borided needles was found in the range of 65 - 90 μm. Even some of the borided teeth went into the substrate as much as 90 μm deep, the average thickness of the single phase Fe_2B layer was about 75 μm.
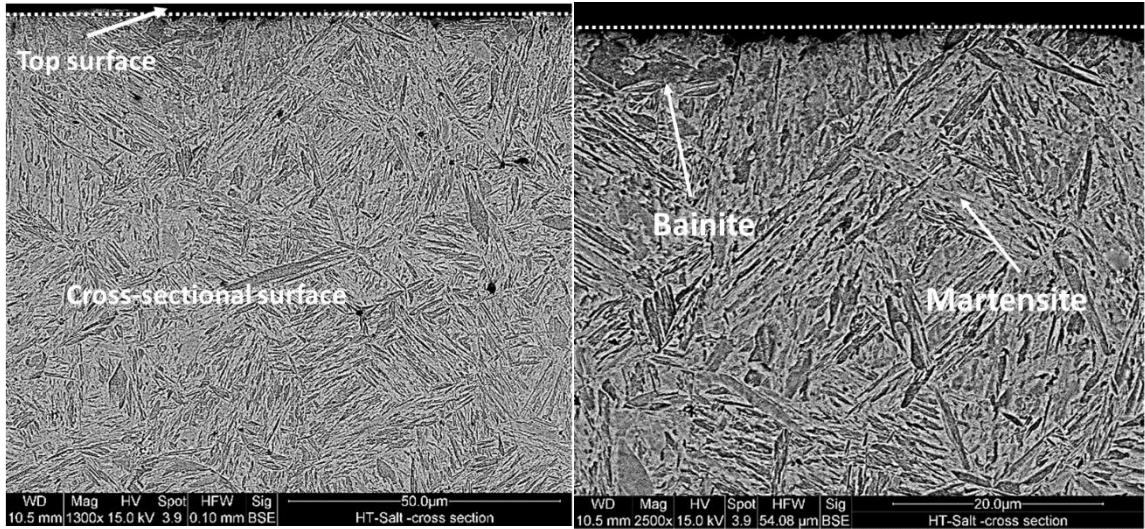
Figure 4.11: Typical backscattered electron (BSE) images of the cross-sectional view of induction hardened sample quenched in 280°C salt, (a) 1200X, (b) 2500X.
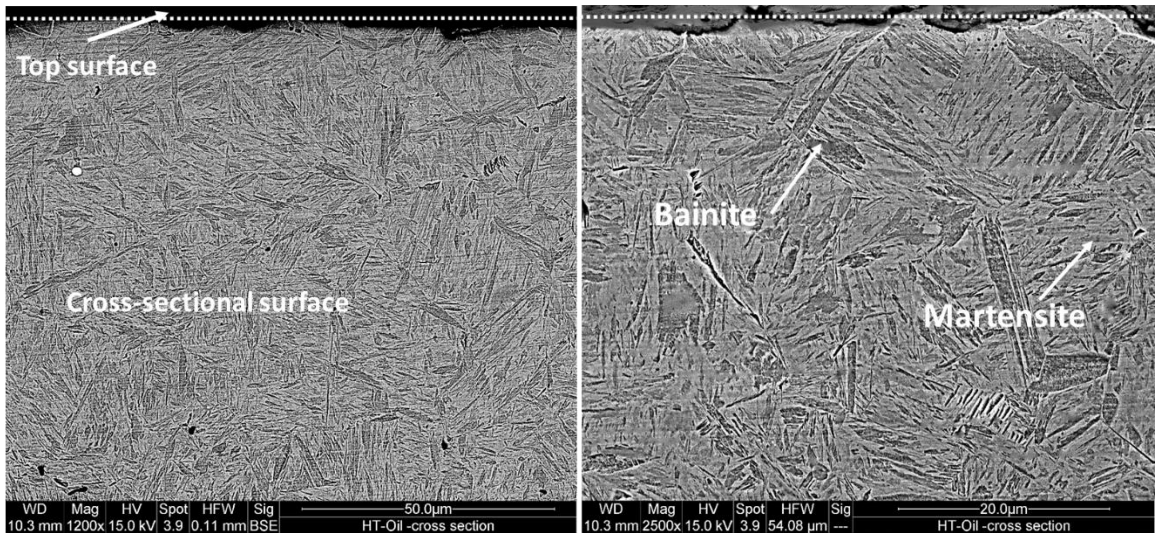
Figure 4.12: Typical backscattered electron (BSE) images of the cross-sectional view of induction hardened sample quenched in 160°C oil, (a) 1200X, (b) 2500X.
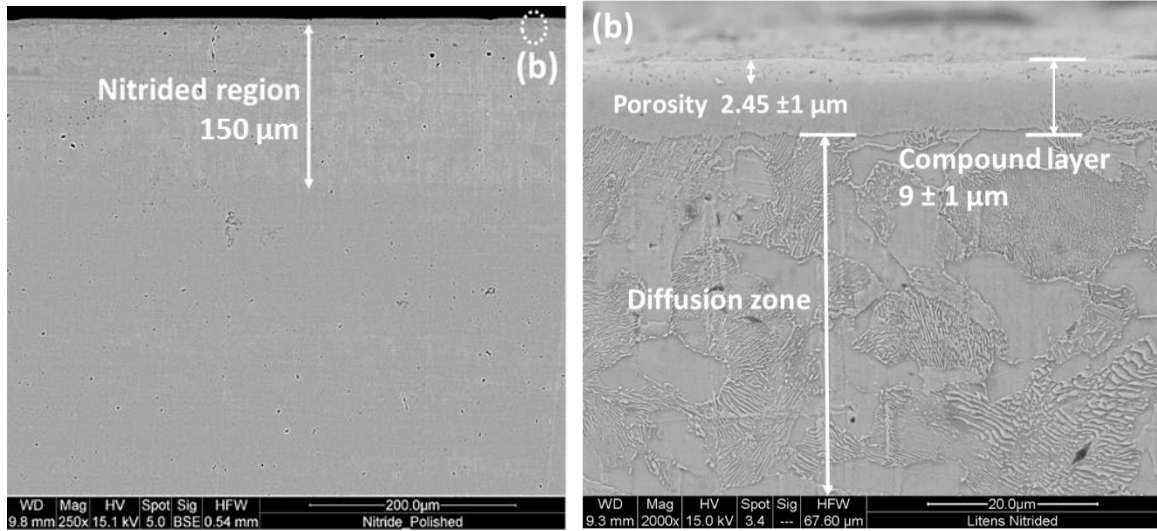
(a)   (b)

Figure 4.13 Typical backscattered electron (BSE) images of the cross-sectional view of nitrided 1045 steel. (b) High magnification of the region marked as (b) in (a) showing the composition of nitrided layer.
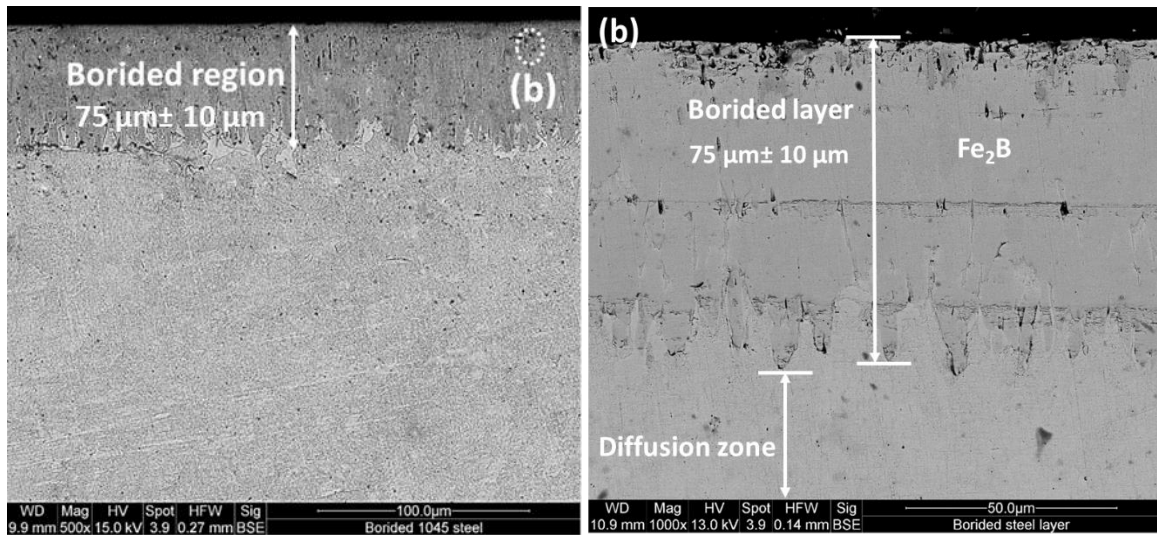
(a)   (b)

Figure 4.14 Typical backscattered electron (BSE) images of the cross-sectional view of borided 1045 steel. (b) High magnification of the region marked as (b) in (a) showing the composition of borided layer.

4.3 Hardness of 1045 steel

The Vickers microhardness of as-received and three types of surface treated 1045 steel were measured. The microhardness measurements are presented in two sections, namely measurements of the surface hardness and measurements of cross-sections to help establish the hardness gradient of the hardened region by heat treatment, gas nitriding and electrochemical boriding.

4.3.1 Microhardness measurements of hardened surface

The Vickers hardness values taken from the surfaces of as-received (untreated), induction hardened samples (using different quenching media) and nitrided, borided samples are shown in Figure 4.15. According to the descriptions in previous section 4.3.2 associated with the depth of nitride and borided layers, it should be noted that the dimensions of the indenter have to be shorter than the thickness of the layers in order to obtain the precise microhardness. Therefore, the relatively low loads 50 gf was applied to measure the hardness. The hardness is also influenced by the specific surface topography and phase content of the area of indentation.

The as-received sample showed the lowest hardness value at 242.64 HV, whereas the higher hardness was achieved on the surface treated samples. The sample quenched in water at 60 °C showed the highest hardness value (553.02 HV) compared with the samples quenched in salt bath and oil. The surface hardness value of the samples quenched in oil (520.72 HV) was similar to that of the samples quenched in salt bath (530.18 HV). This was consistent with the observations on the microstructures of these heat-treated samples that consisted of different percentages of bainite. The hardness values can indicate the phase transformation status, since the hardness measured is directly related to the volume or quantity of bainitic and martensitic microstructures transformed. The standard deviation for induction hardened samples is higher than that of non-heat treated and nitride samples due to mixture of martensitic and bainitic microstructure.

The electrochemical boriding process produced the highest surface microhardness of 1155 HV, followed by induction hardened and quenched samples, and then the nitrided

sample. As it is well known, the hardness of the material is of great importance in resisting the action of sliding forces during wear testing, these high hardness levels were expected to result in a better wear performance in the following sliding tests. However, the microhardness of the gas nitrided sample was increased to 418 HV which is still lower compared to other surface treated samples. The untreated sample with ferritic/pearlitic microstructure shows the lowest hardness of 242 HV which increased to over 500 HV after induction hardened with upper and lower bainitic and martensitic microstructures.
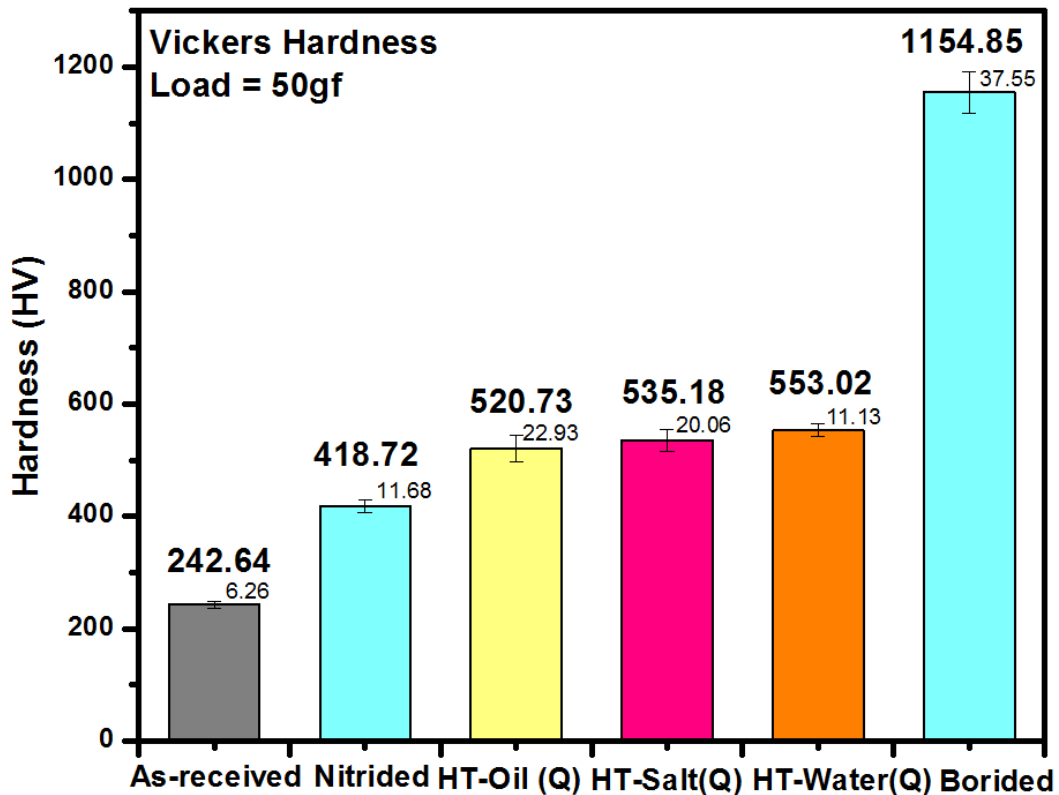
Figure 4.15: Surface microhardness of untreated, borided, nitrided and induction hardened 1045 steel measured by 50 gf on the surface.

4.3.2 Microhardness of cross-sections

As mentioned previously, the cross-sectional measurements were made in order to plot the hardness gradient which can help to define the boundaries of the hardended layer and diffusion zone for nitrided and borided samples. Two measures were used to determine the extent of the diffusion zone namely microhardness and metallography. The results of

through-thickness microhardness distributions are shown in Figures 4.16 to 4.18 for induction heat treated (160 °C oil quenched), nitrided and borided 1045 steel as plotted using Origin Pro software. The hardness depth is derived from the curve representing the hardness over distance from the surface by measuring the distance from the surface to the calculated hardness limit.

A similar microhardness gradient is seen for nitrided and borided cross-sectional surface with the increasing of the distance from the surface, the hardness reduced. For the steel treated by boriding, the maximum hardness value corresponds to the borided layer reached 1310 HV and 72 μm thick Fe_2B borided layer was formed. The hardness of nitrided sample reached 426 HV at the compound layer and a 161 μm thick nitrided layer was formed on the surface. It can be clearly seen that the depth of the diffusion zone measured by metallography (dashed line in plots) is smaller than that determined by microhardness. The possible reason is that the distributions of nitrogen and boron atom in α-Fe is not visible using optical metallography but can increase the hardness in the diffusion zone.

For the steel heat treated at 820 °C for 2 minutes followed by 160 °C oil cooling, the maximum hardness reached 564 HV and tended to fluctuate and exhibited a plateau after 200 μm at 540 HV. There is no obvious change in hardness values as well as the constant microstructures since the heat treated effect is fairly uniform in these small samples.
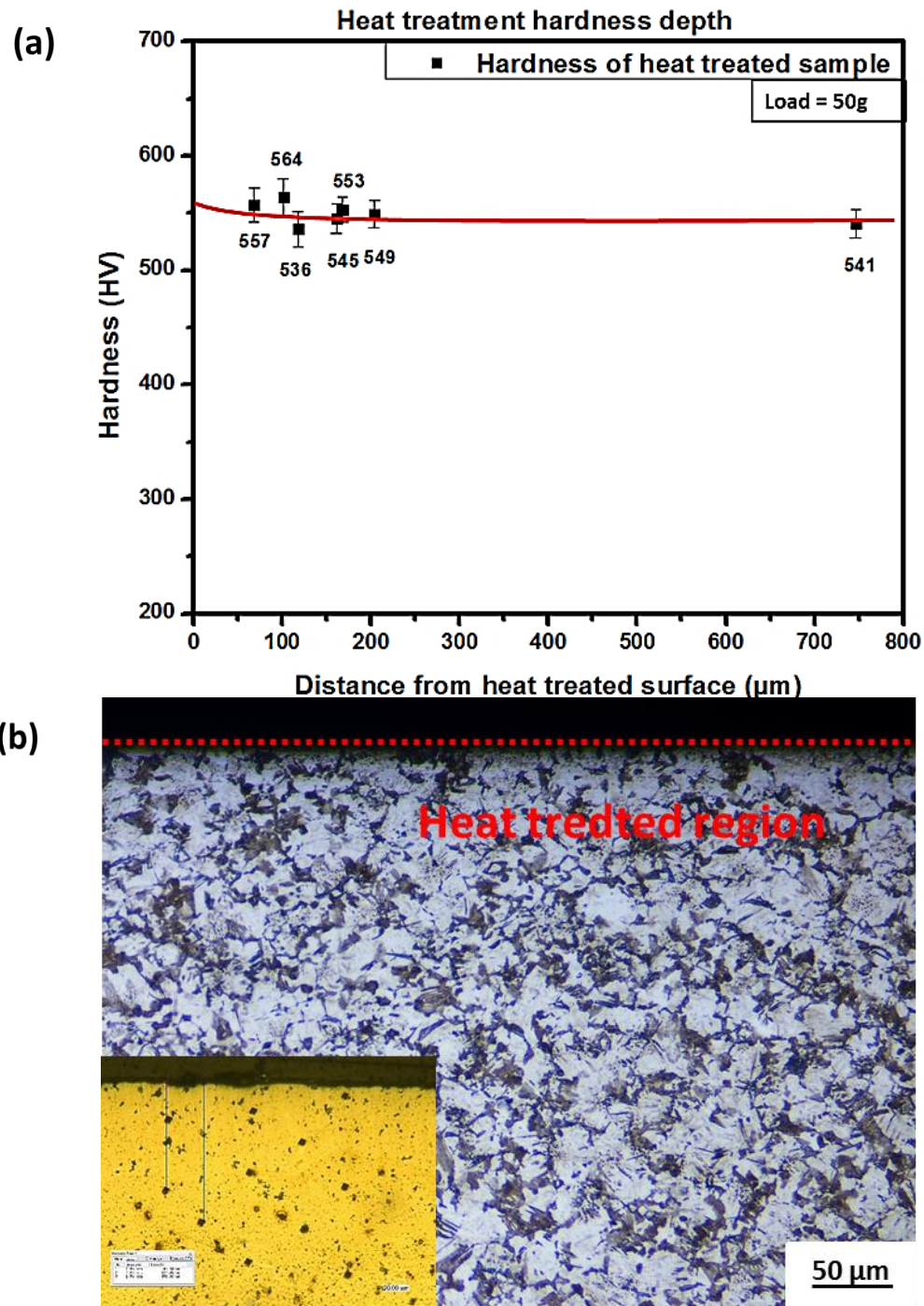
Figure 4.16 Relationship between the microhardness and distance from the induction heat treated (160 °C oil quenched) surface, (a) cross-sectional microhardness distribution, (b) metallography of induction heat treated region.
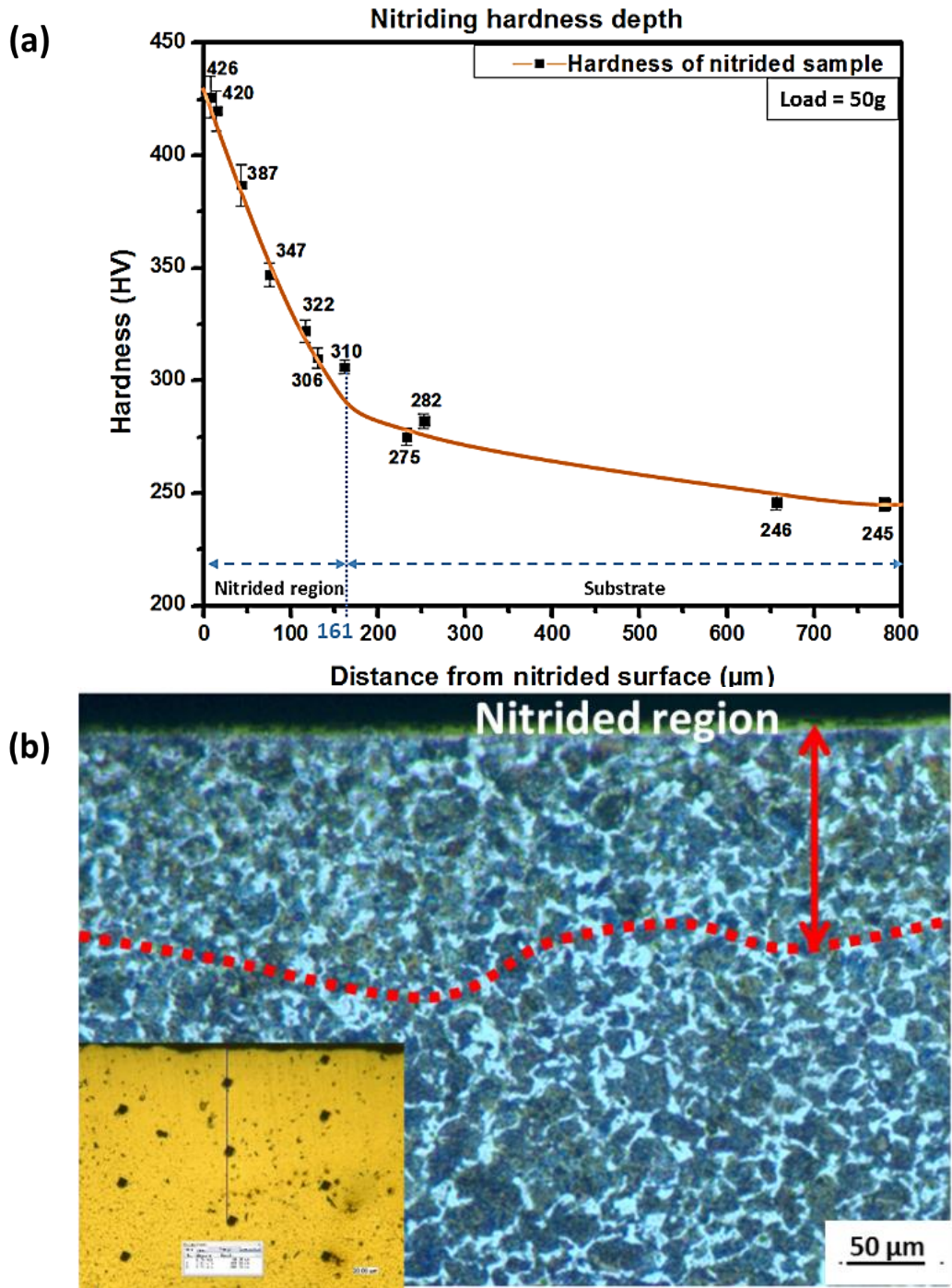
Figure 4.17 Relationship between the microhardness and the distance from nitrided surface, (a) Cross-sectional microhardness gradient, (b) metallography of nitrided region.
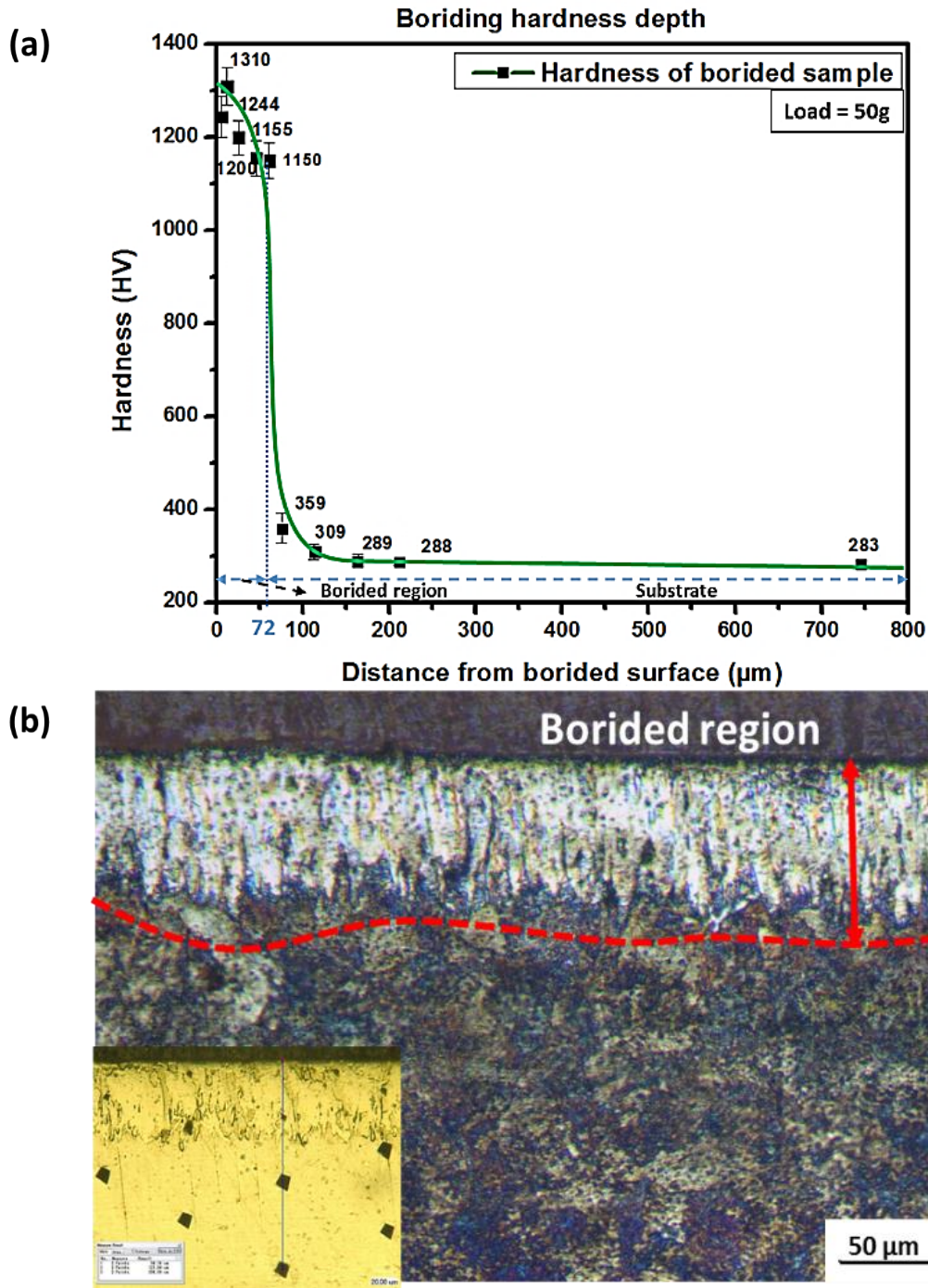
Figure 4.18 Relationship between the microhardness and the distance from borided surface,

(a) Cross-sectional microhardness gradient, (b) metallography of borided region.

4.5 Cooling curves on CCT diagram

Based on the results of hardness and microstructural investigations as shown in Table 4.2, a continuous cooling transformation diagram for AISI 1045 steel was built and is shown in Figure 4.19. It was observed that the temperature of the nose of "C" curve was around 550 °C (the temperature of beginning of the transformation to bainite) and the time to avoid the nose must be less than 5 seconds.

Table 4.1 Summary of measured and estimated hardness and microstructural transformation of induction hardened AISI 1045 steel.

Quenchants	Holding time (sec)	Vickers hardness (HV)	Phases composition	Appearance
60°C water	10	553	(81.6%)Martensite, (20.2%)retained austenite	Crack growth on the surface
280°C melt salt (40%NaOH + 60%KOH)	10	535	(7.7%)Ferrite, (13.4%)bainite, (76.2%)martensite	No crack formed
160°C quenching oil	15	521	(8.6%)Ferrite, (19.5%)bainite，(71.9%)martensite	No crack formed

Following the blue cooling curve (AISI 1045 steel quenched in water at 60 °C), the austenite directly transformed into martensite according to the discussion in section 4.2. The austenite did not completely transform into martensite due to the cooling curve across the martensitic phase region between M_s and M_f (M_s represents the beginning of the transformation to martensite and M_f represents the end of the transformation to martensite). At the end of the blue curve, the microstructure of the water-quenched sample consisted of 81.6±2.1 % martensite and 20.2±1.8 % retained austenite. Similar trends were observed on the orange line (AISI 1045 steel quenched in salt bath at 280 °C) and the green line (AISI 1045 steel quenched in oil at 160 °C), but these two curves passed four different regions of microstructure. The transformation began from ferrite, then to pearlite and bainite, and finally ended at martensite. Accordingly, the microstructures of these samples consisted of bainite, martensite, ferrite and pearlite. The oil-quenched sample contained more bainite

(~19.5 %) and the less martensite compared with the salt-quenched sample, as indicated in Section 4.2.2.
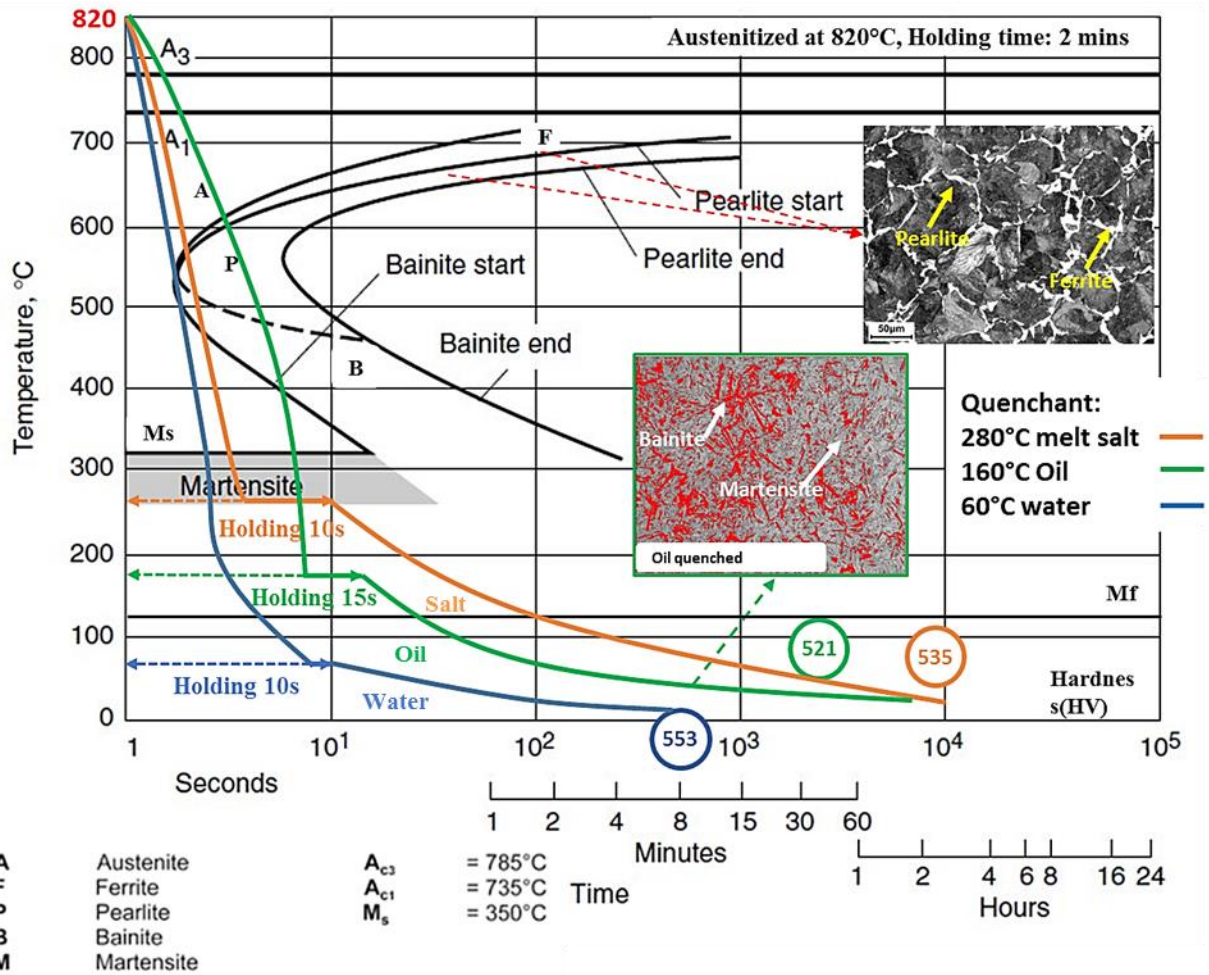
Figure 4.19 Continuous cooling transformation diagram combined with cooling curves for induction hardened AISI 1045 steel – austenitized at 820°C for 2 minutes and quenched in 280°C salt, 160°C oil and 60°C water.

4.6 Summary

The heat treatments were designed and conducted for AISI1045 steel; All induction hardened samples went through the microstructure transformation from pearlite and ferrite to the martensite and bainite. Induction heating at 820 °C for 2 minutes and then quenching in the following modes: i) a salt bath composed of 60% KOH and 40% NaOH at 280 °C holding for 10 seconds; and ii) quenching oil at 160 °C holding for 15 seconds both improved the hardness of AISI 1045 steel to over 500HV without the formation of thermal cracks. The second quenching method, i.e. the oil quenching, resulted in highest bainitic percentage (~19.5 %) consisting of both lower bainite and upper bainite.

The microhardness data were collected and plotted against surface hardened depth. The borided region had the highest hardness values ranging between 1100 HV and 1300 HV compared with hardness values ranging between 310 HV and 430 HV measured in the nitrided region and hardness values ranging between 540 HV and 560 HV measured in the heat treated samples. As the bainite content increased, the hardness values of the induction hardened samples decreased. The hardness data indicated the bainite transformation status, since the hardness is directly related to the volume or quantity of bainitic microstructure transformed. The hardness value decreased with more volume of bainite transforming according to the salt quenched sample show higher hardness (535 HV) and lower bainitic percentage (~13.4 %) compared with the oil quenched sample. The average nitrided layer thickness on the surface for the gas nitriding process is 161 μm, which was more than double the borided layer (72 μm). The oil and salt quenched samples were subjected to sliding wear tests to evaluate the wear resistance and study the wear mechanism compared with nitrided and borided samples as described in Chapter 5.

CHAPTER 5

SLIDING WEAR BEHAVIOUR OF HEAT TREATED 1045 STEEL, IN COMPARISON WITH NITRIDED AND BORIDED SURFACES

In this chapter, results of sliding wear tests are presented and a tribological analysis of the wear mechanisms of steel pulley bores was conducted to investigate the sliding damage processes in AISI 1045 steel treated in comparison with with gas nitriding, electrochemical boriding and induction hardening. The purpose of these investigations was to understand how wear occurred on steel pulley bores with different surface treatments on a microscopic scale. Block-on-ring sliding wear tests were used to evaluate their tribological properties with a constant velocity of 1m/s and load 44.48 N under dry, lubricated and relative humidity conditions. Measurable mass loss value was 0.01 mg with the balance used to determine the volumetric wear rates. Surface profilometer and scanning electron microscopy (SEM) with energy dispersive X-ray spectroscope (EDS) were employed to measure and observe the worn surfaces compositions and cross-sections below worn surfaces (subsurfaces). The results were analyzed, discussed, and then summarized.

5.1 Sliding wear behaviour of induction hardened 1045 steel

As discussed in Chapter 4, one typical heat treated bainitic sample need be selected to investigated in more details to compare their wear performance with nitrided and borided samples. The dry and lubricated sliding wear tests were firstly conducted on heat treated bainitic samples to evaluate their wear resistance compared with untreated 1045 steel.

The heat treated 1045 samples described in Chapter 4 were tested using block-on-ring sliding wear tests at a constant load of 44.48 N and a speed of 1 m/s with three different sliding distances, i.e., 1,000 m, 3,000 m, 5,000 m under dry and lubricated conditions. According to the initial wear behaviour of the samples, additional tests with higher and shorter sliding distance were carried out later. For simplicity, the hardened samples by quenching in 160 °C oil and 280 °C molten salt were referred thereafter as HT-Oil and HT-Salt, "HT" signifying heat treated, "oil" and "salt" represent the quchant.

The dry wear volumetric losses were calculated according to Equation (5) and from the mass loss of samples. The lubricated wear volume losses were measured by the surface profilometer, the profiles of the wear track were measured and the section areas were calculated by the Vision and Origin softwares, then the volume loss was calculated using Equation (6) as discussed in section 3.3.3. The results are summarized in Table 5.1, and the relationship between volume loss and sliding distance is shown in Figure 5.1, which reveals that a near linear relationship exists between the volume loss and the sliding distance. The volumetric losses were found to increase with increasing sliding distance under both dry and lubricated conditions. The wear rate was obtained by calculating the slope of the fitted lines in Figure 5.1, and the corresponding data are listed in Table 5.2.

Table 5.1 Dry and lubricated wear loss of induction hardened 1045 steel after different sliding distance (1000m, 3000m, 5000m). (lubricant: Peerless LLG)

Distance(m)	Dry Volumetric Wear loss(mm³)			Peerless LLG Lubricated Volumetric Wear loss(mm³)	
	HT-Oil	HT-Salt	Untreated	HT-Oil (Q)	HT-Salt
1000	0.02127	0.02548	0.76108	0.00151	0.00125
3000	0.02675	0.02887	1.20932	0.00575	0.00954
5000	0.03401	0.12187	1.50393	0.01264	0.01921

Table 5.2 Summary of wear rate and wear coefficient of induction hardened 1045 steel

Sample condition	Surface Hardness (HV)	Dry Wear test		Lubricated Wear test	
		Wear Rate (mm³/m)	Wear rate Coefficient K, (mm³/N-m)	Wear Rate (mm³/m)	Wear rate Coefficient K, (mm³/N-m)
Untreated	242.64	3.40×10^{-4}	6.51×10^{-6}	2.17×10^{-5}	4.88×10^{-7}
HT-Oil	520.73	7.76×10^{-6}	1.72×10^{-7}	2.33×10^{-6}	5.24×10^{-8}
HT-Salt	535.18	2.06×10^{-5}	4.52×10^{-7}	3.6×10^{-6}	8.09×10^{-8}
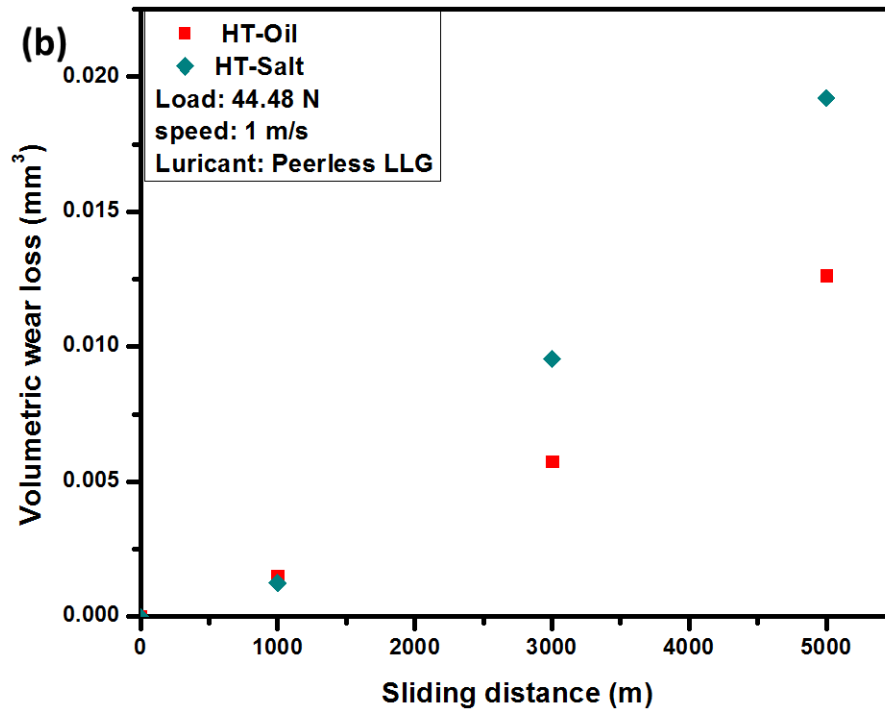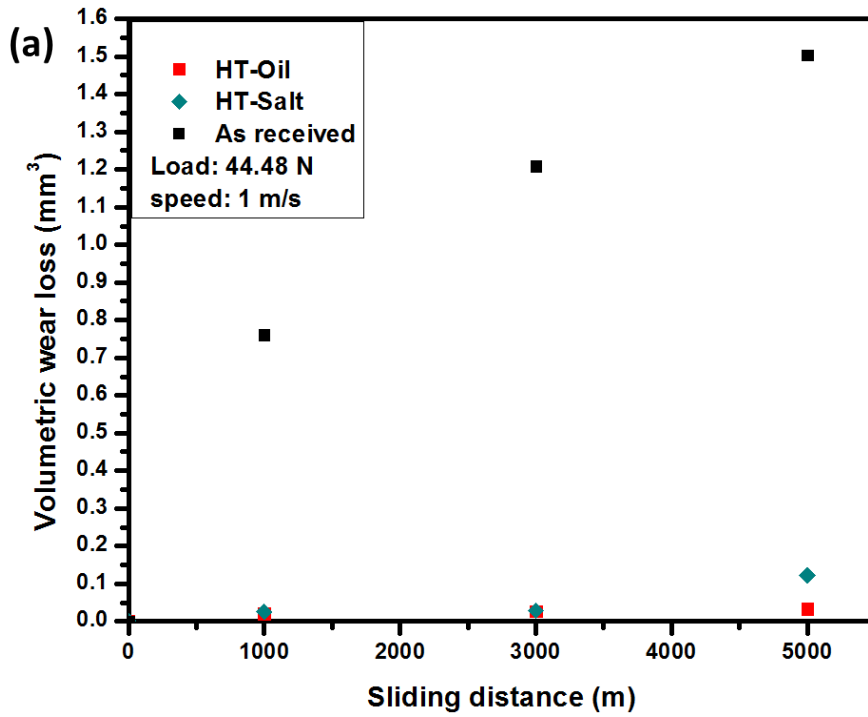
Figure 5.1. Wear volumetric losses against sliding distance curves for induction hardened 1045 steel in different environments, (a) dry, (b) lubricated.

It can be clearly seen that the volumetric wear loss of heat-treated samples was over one order of magnitude lower than that of the untreated sample after different sliding distance; the HT-Oil sample showed the lowest wear rate which indicated the lowest wear coefficient K as well in both dry and lubricated condition. The wear coefficient K of samples in different conditions were calculated based on the transition of equation (8):

$$K = \frac{WH}{P} \tag{10}$$

Where W is the wear rate; P is the applied load; H is the hardness of the material. K is a dimensionless constant determined by wear conditions and contact materials to characterize and correlate the wear of materials. The K of heat treated samples was one order of magnitude lower than that of the untreated samples.

The wear track of the counter-face 52100 steel ring was shown in Figure 5.2, and Figure 5.3 to 5.7 illustrated the optical images of the wear tracks, from which we can see that the wear tracks of the untreated sample were the widest compared to that of the heat treated samples after sliding at different distances. In addition, the wear tracks of the salt quenched samples were wider and deeper than those of the oil quenched samples. The material transfer from the counter-face ring to the block sample surfaces also can be observed in the wear tracks of untreated and heat treated samples.

It was observed that oil quenched sample contains more bainite as the fraction of 19.5%, while salt quenched sample contains 13.4% bainite but relatively higher content of martensite due to the higher hardness as discussed in Sections 4.2.2. Thus, it is possible that the increasing bainite content lead to wear rate reduction. Therefore, the wear resistance of 1045 steel is improved greatly by the induction hardening, and the oil quenched sample with higher bainite content that exhibits the better wear performance is chosen for the further study compared with nitrided and borided samples.
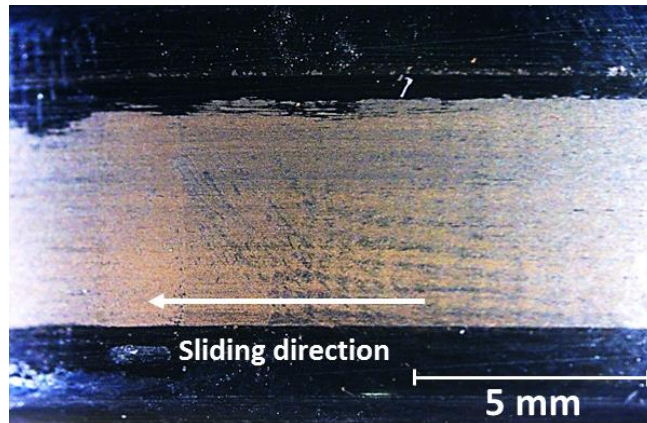
Figure 5.2 Dry wear track of counterface 52100 steel ring

Figure 5.3 Dry wear tracks of untreated AISI 1045 steel sample tested to different sliding distances, (a) 1000m, (b) 3000m, (c) 5000m.

Figure 5.4 Dry wear track of oil quenched AISI 1045 steel sample with different sliding distance, (a) 1000m, (b) 3000m, (c) 5000m

Figure 5.5 Dry wear track of salt bath quenched AISI 1045 steel sample with different sliding distance, (a) 1000m, (b) 3000m, (c) 5000m
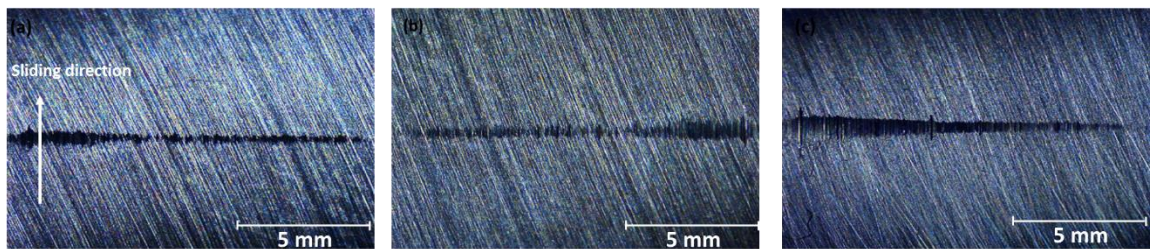
Figure 5.6 Lubricated wear track of 1045 steel sample quenched in salt bath at 280 °C with different sliding distance (Lubricant: Peerless LLG), (a) 1000m, (b) 3000m, (c) 5000m.
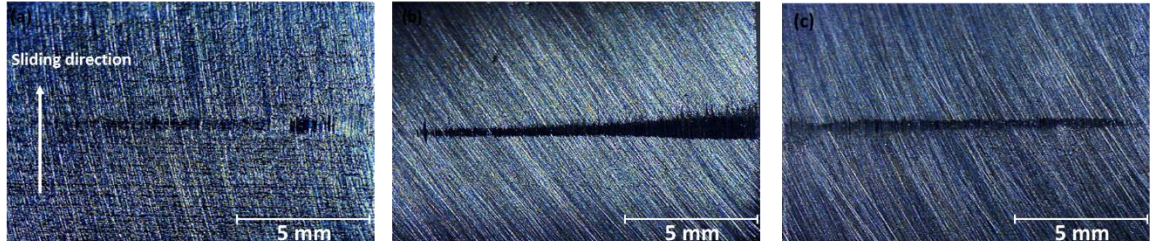
Figure 5.7 Lubricated wear track of 1045 steel sample quenched in oil at 160 °C with different sliding distance (Lubricant: Peerless LLG), (a) 1000m, (b) 3000m, (c) 5000m.

5.2 Dry sliding wear behaviour of surface treated 1045 steel

5.2.1 Wear volume loss

As observed earlier in Section 5.1, the wear resistance of oil quenched sample was relatively high compared to salt quenched sample in dry and lubricated sliding wear tests. The same experiments conducted on the nitrided and borided samples, with block sample sliding against 52100 ring at 1 m/s speed, 44.45 N load and the results were used to make a comparison with oil quenched sample to further validate the wear performance of heat treated samples. The samples were tested for 500 m, 1000 m, 3000 m, and 5000 m sliding distance and the wear loss results are presented in Table 5.3 and plotted in Figure 5.8.

It can be seen in Figure 5.8, the wear curves for untreated, nitrided, borided and oil quenched 1045 steel after dry sliding tests could be divided into two sections:

1) Running-in stage: determined by using the data in the region of sliding distance from 0 – 1000 m, with a large slope;

2) Steady-state stage: determined by using the data in the region of sliding distance from 1000 – 5000 m, with a small slope.

Table 5.3 Summary of wear loss for untreated, nitrided, borided and oil quenched 1045 steel after five sliding distance under dry sliding tests.

Distance(m)	Dry Volumetric Wear loss (mm^3)			
	Nitrided	Borided	HT-Oil	As-received
500	0.16264	0.18018	0.02127	0.61081
1000	0.25616	0.43456	0.02548	0.76108
3000	0.39743	0.53037	0.02675	1.20932
5000	0.62236	0.54663	0.03401	1.50393
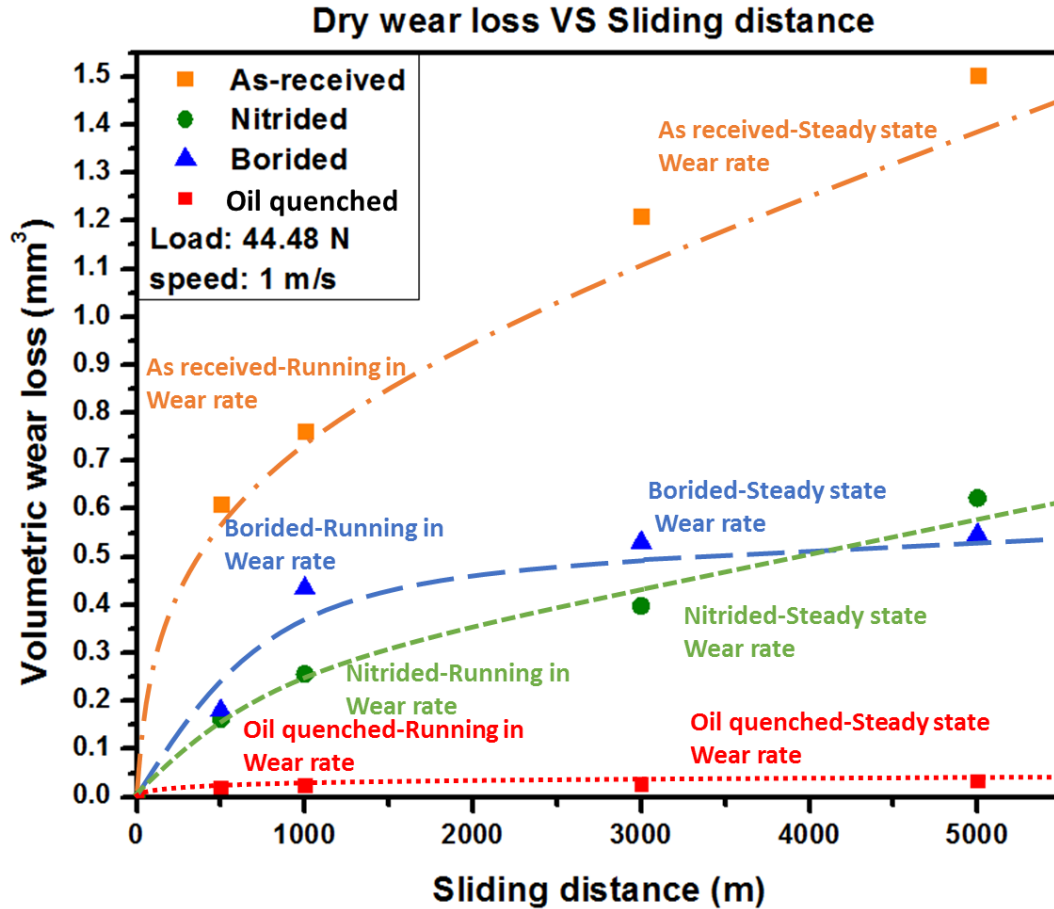
Figure 5.8 Wear volumetric losses against sliding distance curves for untreated, nitrided, borided and oil quenched 1045 steel under dry sliding test.

The wear loss of untreated, nitrided and borided samples increased relatively rapidly during the early running-in stage compared to the steady increase after 1000 m sliding distance considered to be the steady-state stage. The initial increase could be a geometrical effect of moving from a flat surface to a curved surface where wear rates can reach an equilibrium. The wear rate of the steady state stage was derived from the data where a linear relation between volume loss and sliding distance occurred, and the results are listed in Table 5.4. The wear rate of the running-in stage was one order of magnitude higher than that of the steady-state stage. The Oil quenched sample still showed the lowest wear rate both at running-in stage (2.55×10^{-5} mm^3/m) and steady-state stage (2.13×10^{-6} mm^3/m), while the wear rates of nitrided and borided samples were one order of magnitude higher than them. Although there is a rapid rise of wear loss of borided sample in the initial

running-in stage, the wear rate tends to stabilize at 2.80×10^{-5} mm^3/m and the trend of the volumetric wear loss curve was close to that of oil quenched sample.

Table 5.4 Summary of wear rate for untreated, nitrided, borided and oil quenched 1045 steel.

Sample condition	Wear Rate (mm³/m)		Hardness (HV)
	Running-in state	Steady state	
Untreated	7.61×10^{-4}	1.86×10^{-4}	243
Nitrided	2.56×10^{-4}	9.16×10^{-5}	419
Borided	4.35×10^{-4}	2.80×10^{-5}	1155
Oil quenched	2.55×10^{-5}	2.13×10^{-6}	521

5.2.2 Observation of Worn Surfaces

Figures 5.9 - 5.12 show the optical images of the wear tracks after 1000 m, 3000 m and 5000 m, where we can observe that the wear tracks of the nitrided and borided samples are relatively smoother and flatter than those of the oil quenched samples. However, the wear tracks of the untreated and nitrided samples are much wider and deeper than those of borided and oil quenched samples.

Figure 5.13 shows the typical SEM micrographs of dry wear track morphologies of untreated, nitrided and oil quenched samples after 5000 m sliding test, in which, the surface was ground and the accumulation of the wear debris can be observed. The white curve marked the boundary of the wear track where some shallow grooves parallel to the sliding direction were generated. There was no evidence of craters or cavities for untreated and nitrided samples, However, some patches indicated some shearing were observed on the oil quenched sample.
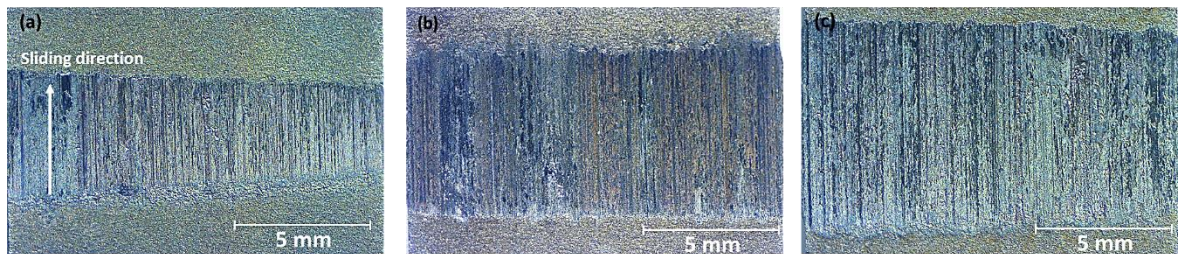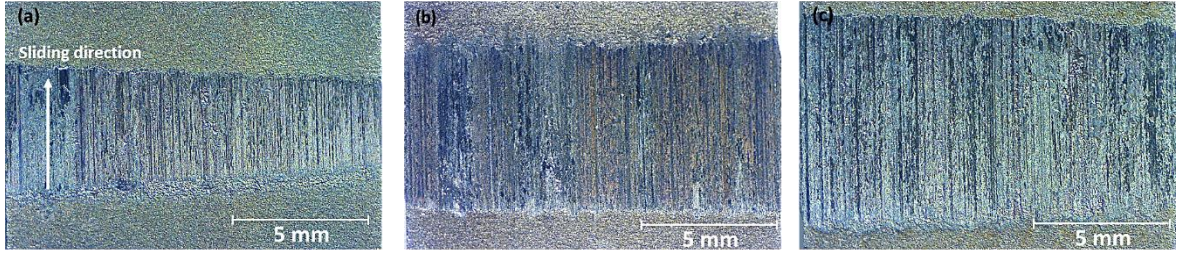
Figure 5.9 Dry wear tracks of untreated AISI 1045 steel sample tested to different sliding distances, (a) 1000m, (b) 3000m, (c) 5000m.
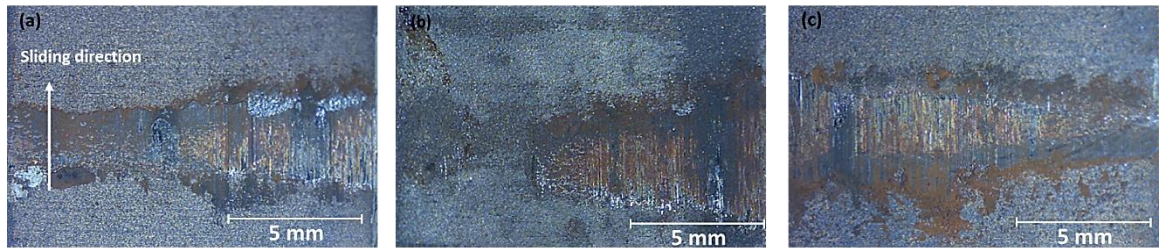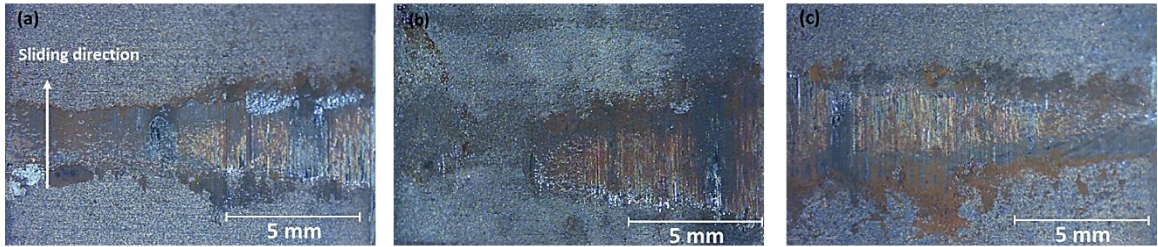

Figure 5.10 Dry wear track of oil quenched AISI 1045 steel sample with different sliding distance, (a) 1000m, (b) 3000m, (c) 5000m
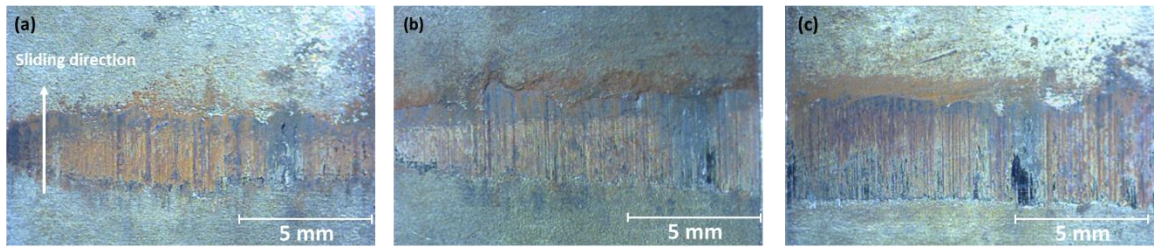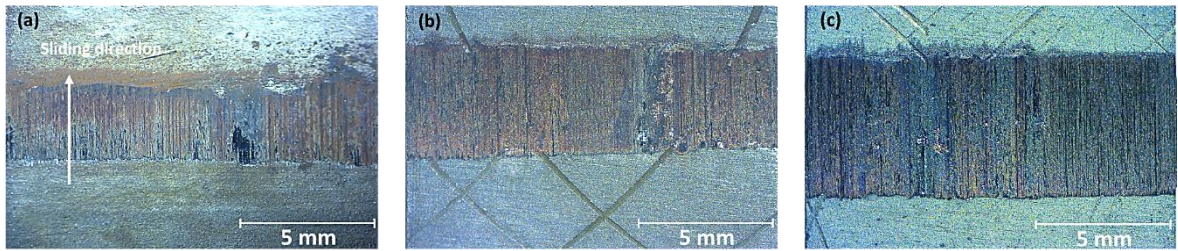

Figure 5.11 Dry wear tracks of nitrided AISI 1045 steel sample tested to different sliding distances, (a) 1000m, (b) 3000m, (c) 5000m
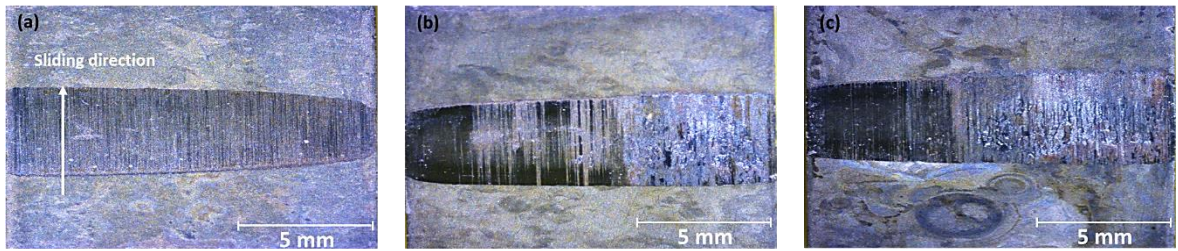
Figure 5.12 Dry wear track of borided AISI 1045 steel sample with different sliding distance, (a) 1000m, (b) 3000m, (c) 5000m
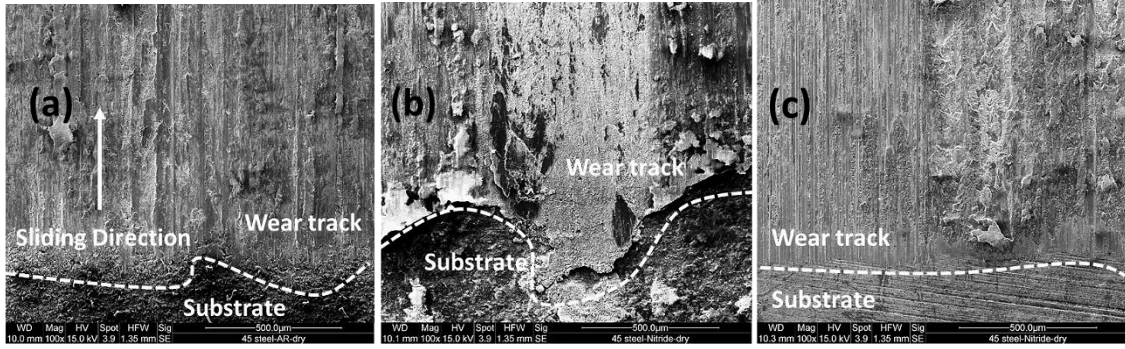
Figure 5.13 SEM micrographs of wear tracks on different surface treated 1045 steel after 5000 m of dry sliding test, (a) untreated, (c) oil quenched, (b) nitrided. The dotted line marks the boundary between the wear track, and the white arrow indicates the sliding direction.

In order to further study, the worn morphology of the hardened layer, the higher magnification SEM morphological photographs with EDS mapping of untreated, oil quenched, nitrided, and borided samples are presented in Figure 5.13. The chemical composition of the wear debris and smooth region were determined by EDS, which demonstrated that the worn surface mainly consisted of deposited oxide and the smooth region exposed was the matrix of the steel. As the sliding tests progressed, a scaly texture was formed along the direction of wear as shown in Figure 5.13(a).

It can be seen in Figure 5.14 (b), a large amount of iron oxide formed on the worn surface of untreated sample. The oxidation is attributed to the friction heat generated in the vicinity of the contact surface that considerably increased the temperature. However, there was one important difference found that the worn surface of oil quenched sample was not oxidized to the same extent as the untreated sample, although it also exhibited oxidational wear. The oxidation the on worn surface of nitrided and borided samples was also detected as shown in Figure 5.14 (f) and (h), but the generation of oxides needs to be further studied to identify whether the tribolayer transformed from the conterface steel ring, or the matrix 1045 steel oxidized after the nitrided and borided layers wore off in the dry sliding wear tests.

93
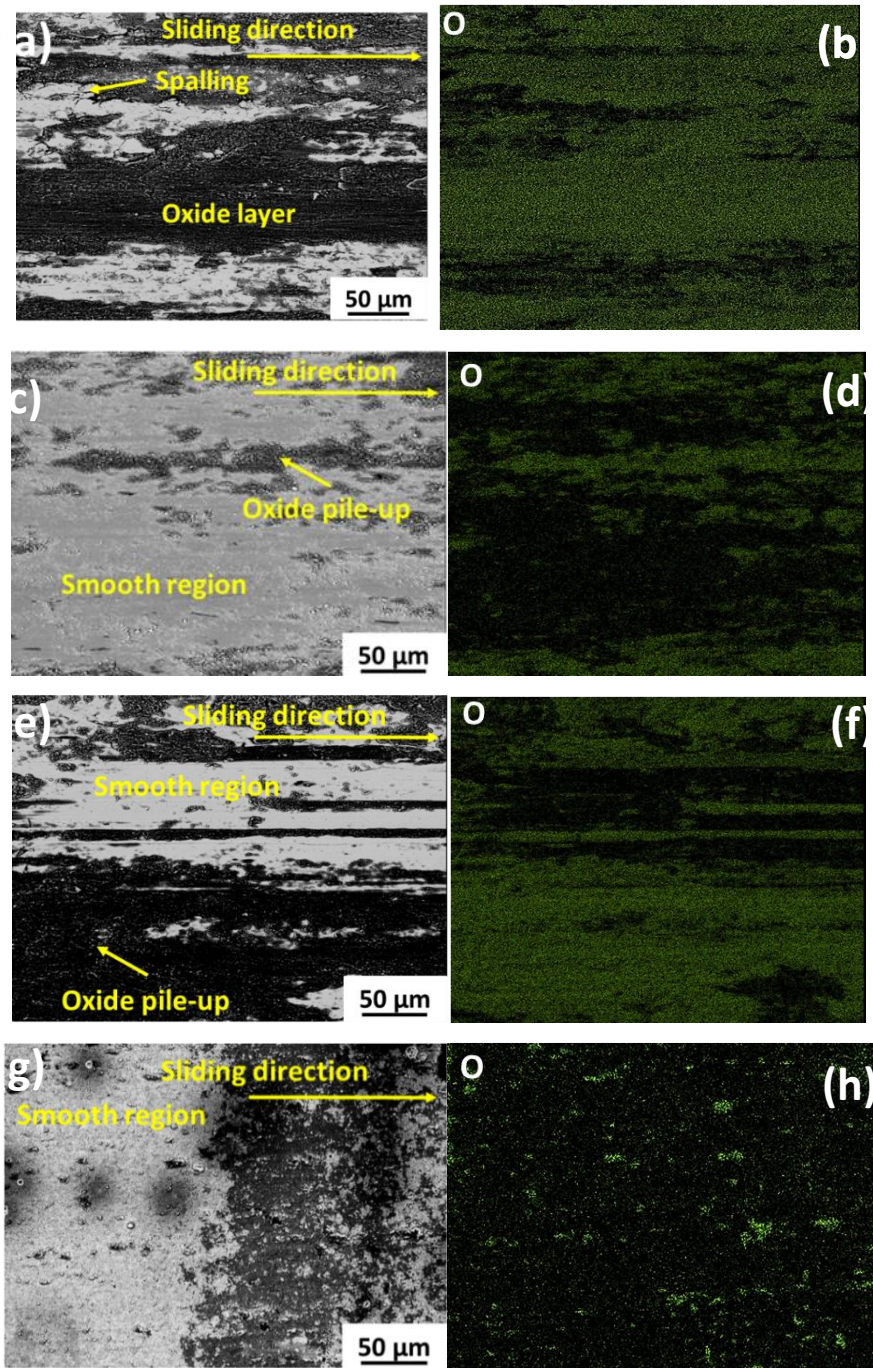
Figure 5.14 SEM images of showing worn surface morphologies of 1045 steel after 5000 m sliding test with EDS mapping images showing the distribution of oxide, (a)(b) untreated, (c)(d) oil quenched, (e)(f) nitrided, (g)(h) borided.
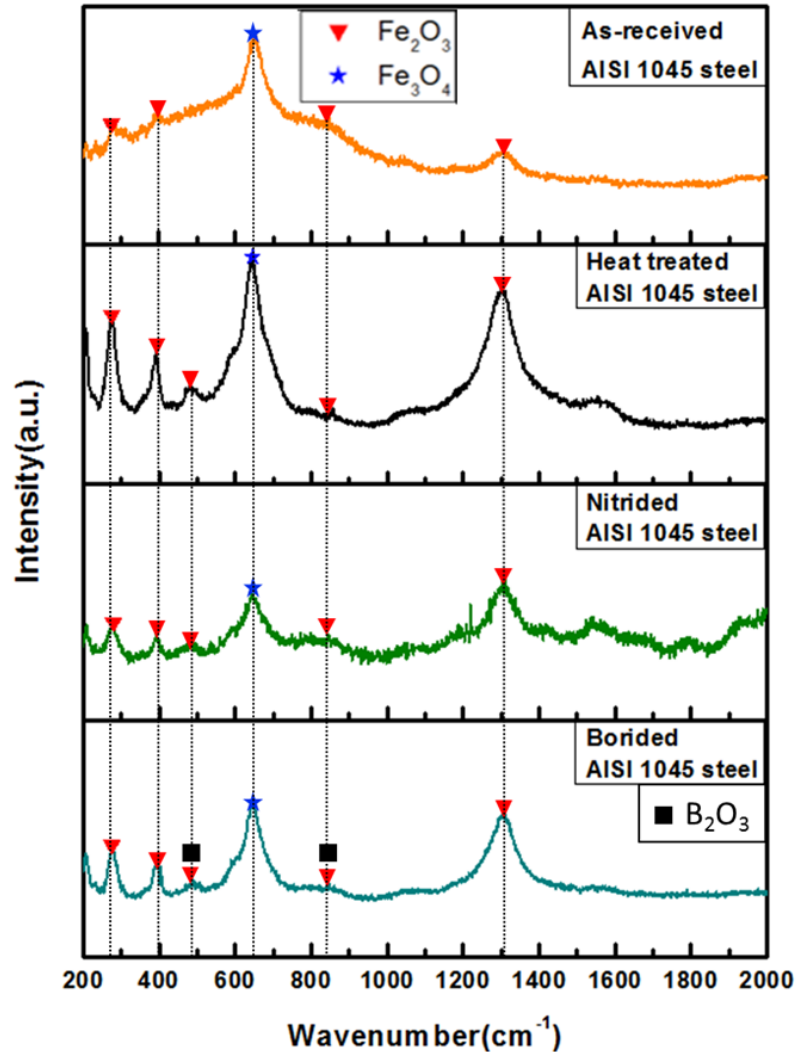
Figure 5.15 Micro-Raman spectra taken from wear tracks formed on untreated, oil quenched, nitrided, borided 1045 steel under dry condition after 5000 m sliding test.

Raman tests were conducted on the worn surface after sliding tests to determine the evolution of oxidized tribolayers. The Raman spectrum was used to identify oxide compositions as shown in Figure 5.15. During dry sliding tests, the compositions of sliding-induced surface oxides were dominated by the mixture of Fe_2O_3 and Fe_3O_4 phases of all types of samples. Raman peaks at 219, 290, 403, 495 599, 808 and 1311 cm^{-1} indicated the formation of Fe_2O_3 phase. Fe_3O_4 phase was identified by the peaks at 301, 534 and 664 cm^{-1} [138-139]. The boric oxide B_2O_3 was possibly detected due to the peaks of boron

95

oxide, boric acid and Fe_2O_3 would appear at the same Raman peak (495 and 808 cm^{-1}) [140]. Thus, the tribolayer covered on the worn surface of untreated, heat treated bainitic samples mainly consisted of a mixture of Fe_2O_3 and Fe_3O_4 phases and the wear mechanism was mainly dominated by oxidation wear. According to some studies, the formation of oxides can cause an effective reduction in the friction coefficient, thereby slowing the wear rate [136-137].

5.2.3 Cross- Sectional Observation of Worn Subsurface

The SEM micrographs in Figure 5.16 to 5.19 provided cross-sectional views of worn surfaces after 5000 m dry sliding tests revealing a plastically deformed zone beneath the worn surfaces of untreated, nitrided, oil quenched and borided samples. The subsurface region indicates that this region is characterized by a flow pattern in which the grain boundaries are increasingly bent towards an orientation the wear direction nearly parallel to the contact surface. Subsurface microstructures reveal the level of damage in the tribolayers, and the deformation of microstructures below the tribolayers.

The morphology of the deformation layer in untreated 1045 sample exhibits a wavy shape, and the sharply deformed area with numerous voids and cracks can be observed under the contact surface as shown in Figure 5.16. It can be clearly seen at high magnification that the microstructure at the top-most layer is almost amorphous due to severe deformation at the contact surface. In this area, the typical pearlitic microstructures disappeared in the subsurface layer instead of showing extensive fragmentation, which consisted of the fractured cementite arranged along the tangential direction of the sliding direction during the severe deformation process as shown in Figure 5.16(b) [141-143]. With increasing the depth of the deformed layer, the extent of deformation gradually decreased where the thickness of the deformed zone was measured as 45 μm. Also, the shear strain decreased as the distance from the wear surface increased.
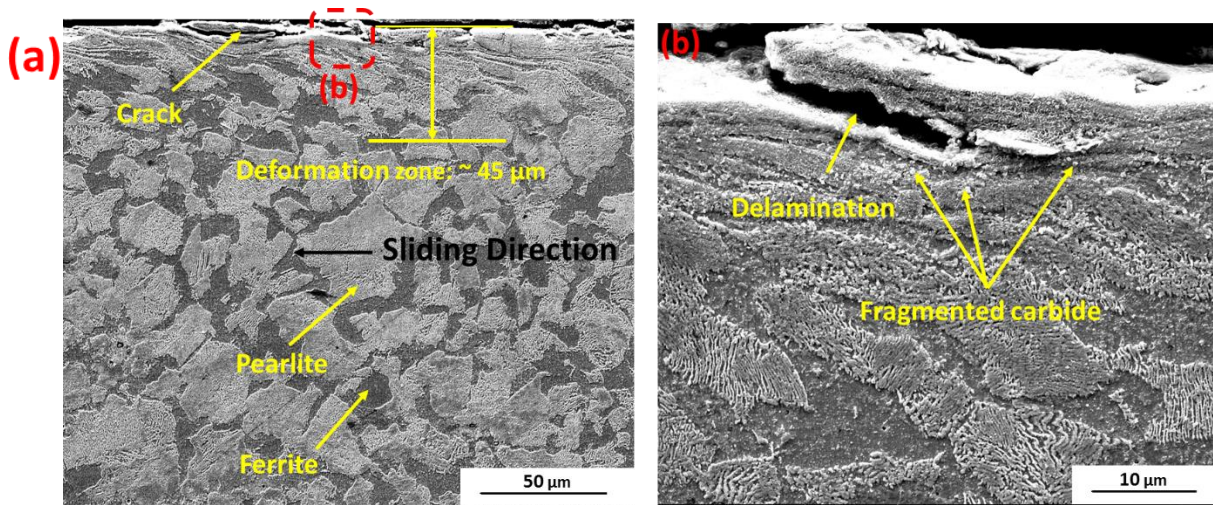
Figure 5.16 The SEM micrographs of subsurface layers below the worn surface of untreated 1045 steel after 5000 m dry sliding wear test, (b) High magnification image of the region marked as (b) in (a).

Figure 5.17 The SEM micrograph of subsurface across the depth of worn surface layers of oil quenched 1045 steel after 5000 m dry sliding wear test.

Figure 5.17 shows the morphology of the subsurface for an oil quenched sample. No obvious material delamination was found, and only a sparse distribution of sub-surface fatigue cracks or voids could be observed along a direction parallel with the subsurface. A thinner 16 μm deformed layer was found with the strained mixed microstructures of martensite and bainite as well as the finer cementite layer which contains smaller spheroidal cementite uniformly distributed in the deformed region. The layer was continuous and quite adherent to the matrix structure with limited porosity. On the one hand, some researchers indicated the cementite can partially re-dissolve into the matrix due to the accumulated deformation energy storage reduced the thermal stability of cementite during the severe deformation process [144]. Therefore, the wear rate was slowed down by the spherical layers with the spheroidisation of deformed and fractured cementite in the sub-surface.

On the other hand, the reaustenitization followed by martensitic transformation could be the reason resulted in the surface hardening around the worn surface to resist the sliding wear [159]. The bainite firstly got strained and deformed at the beginning. As the sliding continues, the temperature of the contacting surface could be increased to the austenitization temperature at the very short time ($\sim 10^{-3}$ - 10^{-4} s) by frictional heating, and then the contacting surface followed by very rapidly quenching with colder subsurface [135]. The worn surface layer was hardened in terms of the increased hardness level of austenitized layer due to the transformation of martensite. However, the produced martensitic structure was so small that only can be found within the narrow region (up to 1 μm) of the subsurface. Therefore, the better wear performance of oil quenched sample can be attributed to a possibly hardened thin layer comprising of the reaustenitized and quenched martensite and its followed work hardening by friction [159].

In addition, the presence of bainite also made a contribution to improve the wear performance. The mixture of bainite and martensite provided high hardness which naturally resists the subsurface deformation, Moreover, the finer, harder and tougher bainitic structures transformed at low temperatures devoid of brittle martensite or carbide, have been shown to resist wear better than other structures having even higher hardness due to their combination of hardness and toughness. High toughness reduced generation of

wear debris by microfracture resulting in wear rates lower than those exhibited by any of the other microstructural variants [145-147]. Under sliding wear conditions, the hardness of bainite does not correlate well with the wear resistance. Rather it is the extent of refinement of the structure in which the soft, coarse pearlitic structures was refined to a hard and fine bainitic structures that plays a major role.

Figures 5.18 and 5.19 show the subsurface microstructures of the nitrided and borided samples. It can be clearly seen in Figure 5.18(b)and Figure 5.19 (c), the nitrided compound layer and borided hardened layer were almost (but not completely) worn away after 5000 m dry sliding test. Hence the iron oxides (Fe_2O_3 and Fe_3O_4) detected in the 5.2.2 were tribolayers that transferred from the counterface (52100 steel ring) to the worn surface of nitrided and borided samples. The hard nitrided and borided surfaces can firmly retain the protective transfer layer, thereby reducing direct contact between the sample and the counter face. Therefore, the adhesive will also be considered as the wear mechanism of nitrided and borided samples.
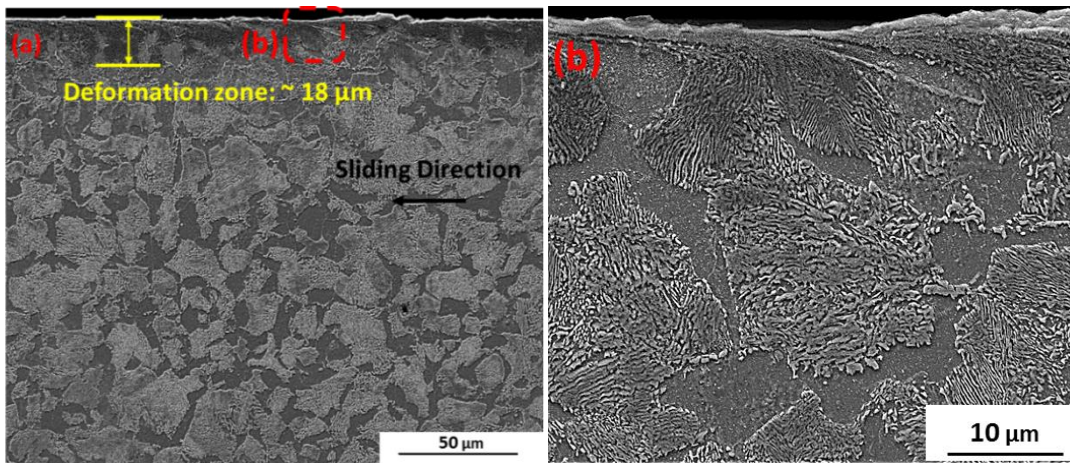
Figure 5.18 The SEM micrographs of subsurface across the depth of worn surface layers of nitrided 1045 steel after 5000 m dry sliding wear test, (b) High magnification image of the region marked as (b) in (a).
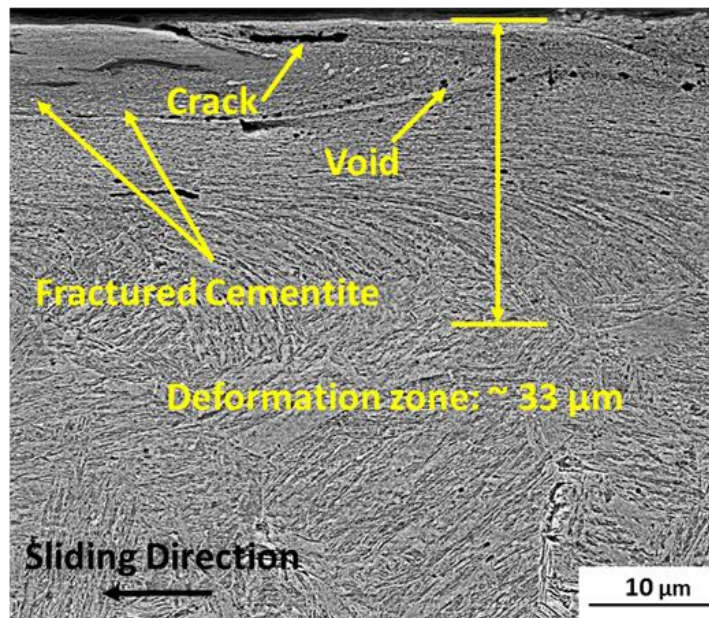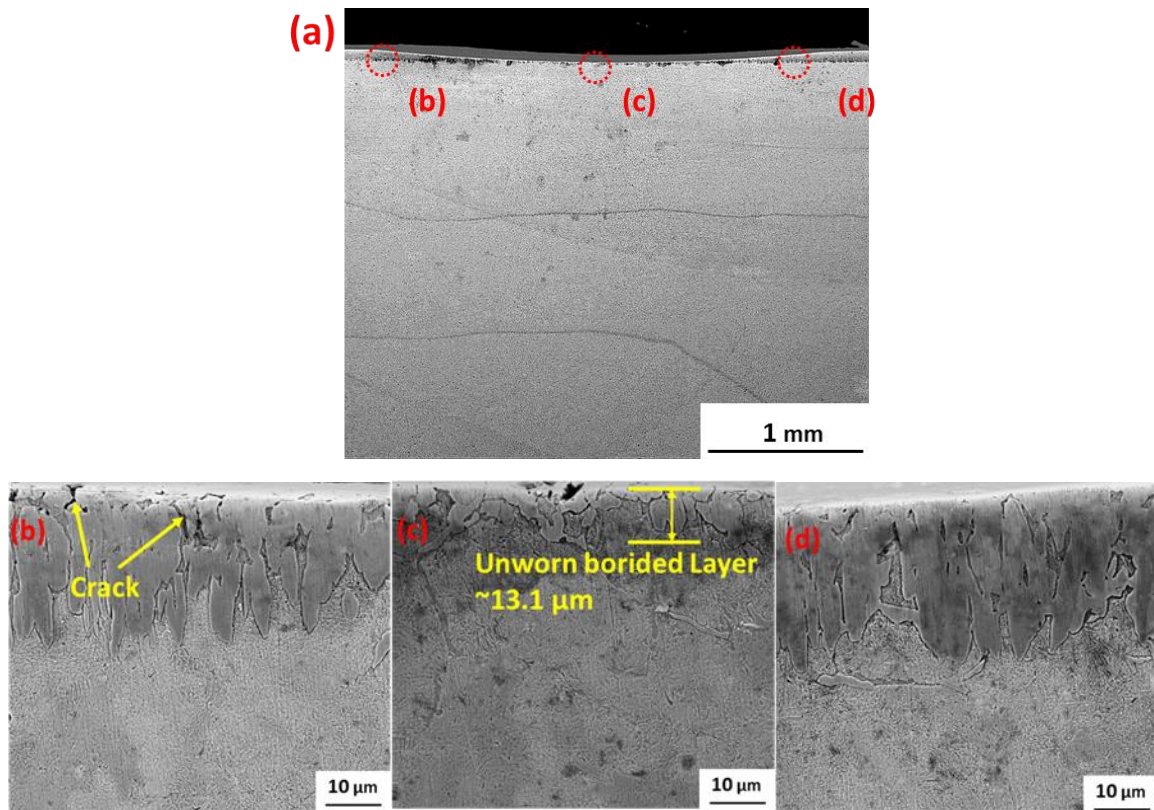
Figure 5.19 The SEM micrographs of subsurface across the depth of worn surface layers of borided 1045 steel after 5000 m dry sliding wear test, (a) overview of the wear track, High magnification images of the region marked as (b), (c), (d) in (a).

The nitrided layer was quite adherent to the matrix material, which is the reason that the delamination wear of nitrided sample was high, and the small deformation zone area was observed below the nitrided layer. The borided layers also exhibit strong bonds with the base steel matrix. After sliding, the borided layer is still not completely removed even at the deepest point of the wear track, and the residual borided layer was around 13.1 μm. According to the previous study, the borided sample exhibited the highest hardness value in the microhardness test, which was expected to show the great wear resistance in the sliding test. However, surface cracks were observed in the borided layer, which indicates a decrease in fracture toughness. Toughness is another key factor affecting the ability of withstanding more deformation without breaking during the sliding wear. It can be predicted that there will be an increase of the wear loss for borided and nitrided samples

when the surface treated layers are completely worn off at longer sliding distance such as 10000 m.

5.3 Summary of dry sliding wear

The wear resistance of AISI 1045 steel was improved greatly by the heat treatment, nitriding and boriding treatments under dry sliding conditions compared to the as received 1045 steel. The sample with higher bainite content (19.5 %) that was heated to 820 °C and 160 °C oil quenched showed the best wear performance after dry sliding wear tests. The wear rate of the oil quenched partially bainitic steel was determined as 2.13×10^{-6} mm^3/m in the steady-state wear period, which was over one order of magnitude lower than that of the nitrided and borided samples, and also much less than that of the untreated sample.

Iron oxides were detected on the worn surface of untreated, oil quenched, nitrided and borided samples, which consisted of a mixture of Fe_2O_3 and Fe_3O_4 phases generated by the friction heat. The wear was mainly dominated by oxidation wear of untreated and oil quenched samples, while the wear of nitrided and borided samples was dominated by adhesive wear since the nitrided and borided layers were both not completely worn off during dry wear sliding process. The worn surface was covered by the tribolayer that transformed from the counterface 52100 steel ring. In addition, the oxidation degree on the worn surface of oil quenched samples is lower than that of the untreated sample.

The sliding wear induced microstructural changes at the surface and subsurface layer, also the plastically deformed layer were observed below the wear tracks. Formation of a layer that consisted of fractured cementite that was observed in the subsurface of oil quenched sample. The finer and more uniform carbides distributed in this layer was considered to reduce the wear rate. By increasing the bainite volume fraction in the mixed bainite-martensite microstructures, the wear resistance improved because of the relatively higher hardness and possibly higher toughness (no quenching cracks) compared with other microstructures.

5.4 Lubricated sliding wear behaviour of heat treated nitride and borided 1045 steel with lubricant Peerless LLG.

5.4.1 Surface roughness

Surface profiles can be considered to be comprised of a certain number of peaks of varying heights and an equal number of valleys of varying depths. The apparatus used in this study was a three dimensional profilometer. The measured surface texture parameters and 3-D profilometry images of the samples prior to sliding wear tests are given in Table 5.5 and plotted in Figure 5.20, it can be seen of the untreated and induction hardened samples showed grooves with non-uniform depths. The untreated samples showed the highest value of surface roughness, the average surface roughness (Sa) of which goes to 2.46 µm, while the average surface roughness of oil quenched and salt quenched samples are around 2.2 µm. In general, the smoothest surface is observed on the nitrided sample which shows the lowest surface roughness 0.36 µm.

The number of real "peaks" is considerably less than the number of "peaks" that are recorded due to the stylus will register a "peak" even when it only traverses a shoulder of an actual "peak". The reduced peak height (Spk) was suggested to indicate the height to be readily removed during the wear process, thus the untreated sample showing the highest value of Spk is expected to experience a higher degree of wear loss compared to the other surface treated samples, which will be examined in the following sliding tests.

5.4.2 Wear performance comparison

In order to examine the lubricated wear performance of and oil quenched nitrided, borided samples sliding tests were conducted on block-on-ring tribometer at 1 m/s speed, 44.45 N load with a grease-like calcium sulphonate complex thickened lubricant (Peerless LLG). The sliding distance was extended to 15000 m to determine the long time durability of surface treated samples.

The optical profilometer images (Wyko) taken from the worn surface after lubricated sliding tests, and the wear scar geometric profiles of surface treated samples at different sliding distance are as shown in Figure 5.21. The outline curves were averaged from five profiles scan data for each sample, and the volumetric wear loss and penetration depth were measured and calculated accordingly. The wear scar width and depth of all surface treated samples increased with the prolonged sliding distance. The nitrided sample showed the largest penetration around 7.42 μm and also the widest wear track as 1.03 mm at 15000 m sliding distance, which were almost two times deeper and wider than those of the oil quenched sample. The scar depth of nitrided sample changed significantly after 3000 m, while that of the borided and oil quenched samples were relatively slightly increased.

The results of tests on samples tested for 500 m, 1000 m, 3000 m, 5000 m and 15000 m sliding distance are presented in Table 5.6 and plotted in Figure 5.22. The wear volumetric losses against sliding distance curves could be divided into running-in stage (0-1000 m) and steady-state stage (1000-15000 m), and the wear rate of each stage was derived from the data where a linear relation between volume loss and sliding distance. Figure 5.23 illustrates the results of wear rates and corresponding wear coefficient which was calculated according to Equation (10). The wear rates in the lubricated condition were one order of magnitude lower than those for the dry condition for all surface treated samples. The oil quenched sample had the highest wear resistance as it showed the lowest wear rate both in the running-in stage and steady-state stage, while the borided samples also presented good wear performance when the wear rates reached an equilibrium. The nitrided, borided and oil quenched samples all exhibited the long-time durability in this condition.

5.4.3 Observation of Worn Surfaces

Figures 5.24 to 5.26 show the optical photographs of worn surfaces of the samples tested to different sliding distances. It can be observed that the wear tracks of the nitrided and borided samples were wider than those of the oil quenched samples. Then the typical SEM micrographs of lubricated wear tracks of the nitrided, borided and oil quenched samples after 15000 m lubricated sliding test were shown Figure 5.27. The scratches on

the surface of the oil quenched sample were not as obvious as those observed on the nitrided and borided samples. The grooves were generated parallel to the sliding direction in the wear tracks of the nitrided and borided samples, whereas a large smooth area was observed without the accumulation of oxide on the worn surface of oil quenched sample.

Table 5.5. Surface texture parameters of AISI 1045 steel with different surface treated methods.

Surface condition	S_a (um)	S_q (um)	S_k (nm)	S_{pk} (nm)	S_{vk} (nm)
Untreated	2.46±0.06	3.06±0.03	8433.4±48.5	6314.4±51.4	3489.5±129.5
Nitrided	0.36±0.008	0.58±0.01	1135.3±34.5	1725.63±7.5	1220.2±46.6
HT-Oil	2.29±0.07	3.46±0.03	6246.4±22.1	3028.5±65.7	3746.3±122.3
HT-Salt	2.19±0.05	2.99±0.04	6909.8±32.3	4411.6±59.7	3339.8±107.4

Table 5.6 Summary of wear loss and penetration depth for nitrided, borided and oil quenched 1045 steel after five sliding distance under lubricated sliding tests with Peerless LLG.

Distance (m)	Peerless LLG Lubricated Volumetric Wear loss (mm³)			Peerless LLG Lubricated Wear Depth (µm)		
	Nitride	Borided	HT-Oil	Nitride	Borided	HT-Oil
500	2.52×10^{-3}	5.47×10^{-3}	9.67×10^{-4}	1.511	2.432	0.874
1000	6.51×10^{-3}	6.55×10^{-3}	1.51×10^{-3}	2.237	2.587	1.381
3000	0.013	0.0101	5.75×10^{-3}	2.976	2.775	2.624
5000	0.027	0.0124	0.013	6.043	3.564	4.929
15000	0.034	0.0174	0.017	7.421	5.512	4.969
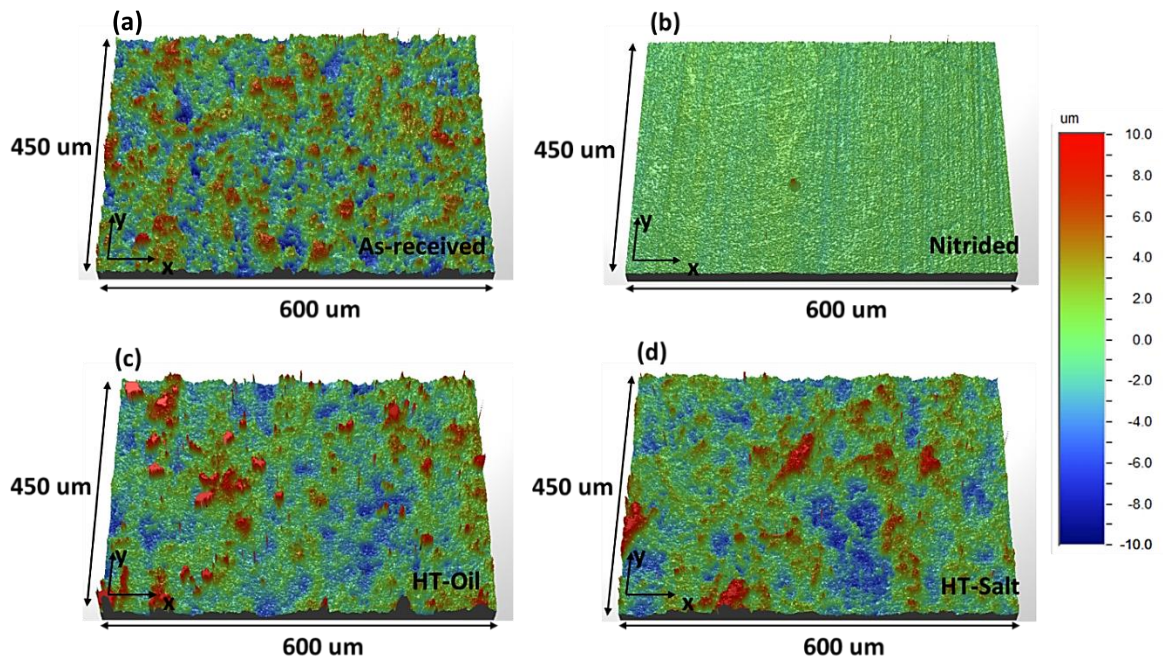
Figure 5.20 3-D optical profilometry images of different AISI 1045 steel specimens, (a) as- received, (b) nitrided, (c) quenched in oil at 160 °C, (d) quenched in salt bath at 280 °C, (e) borided.
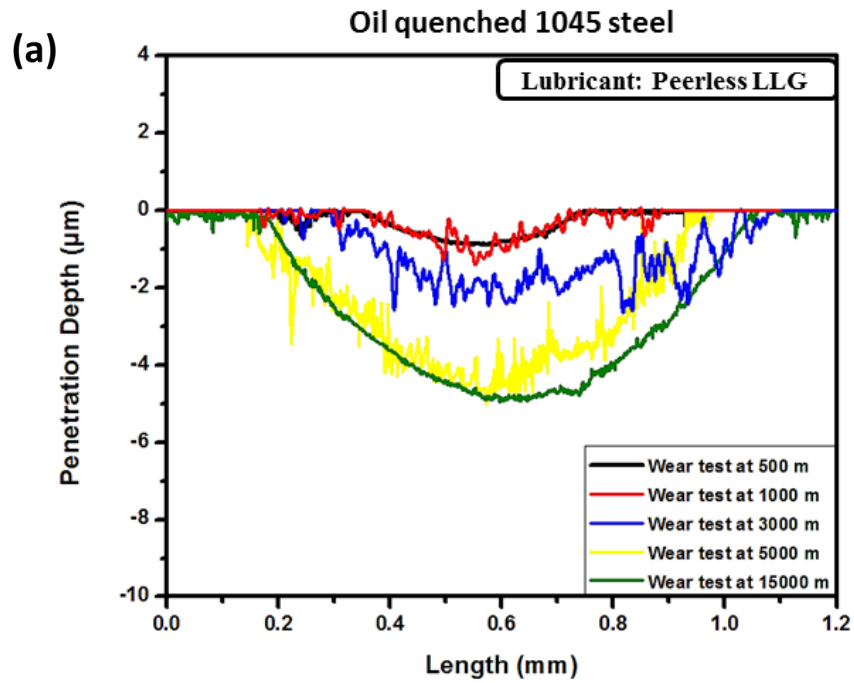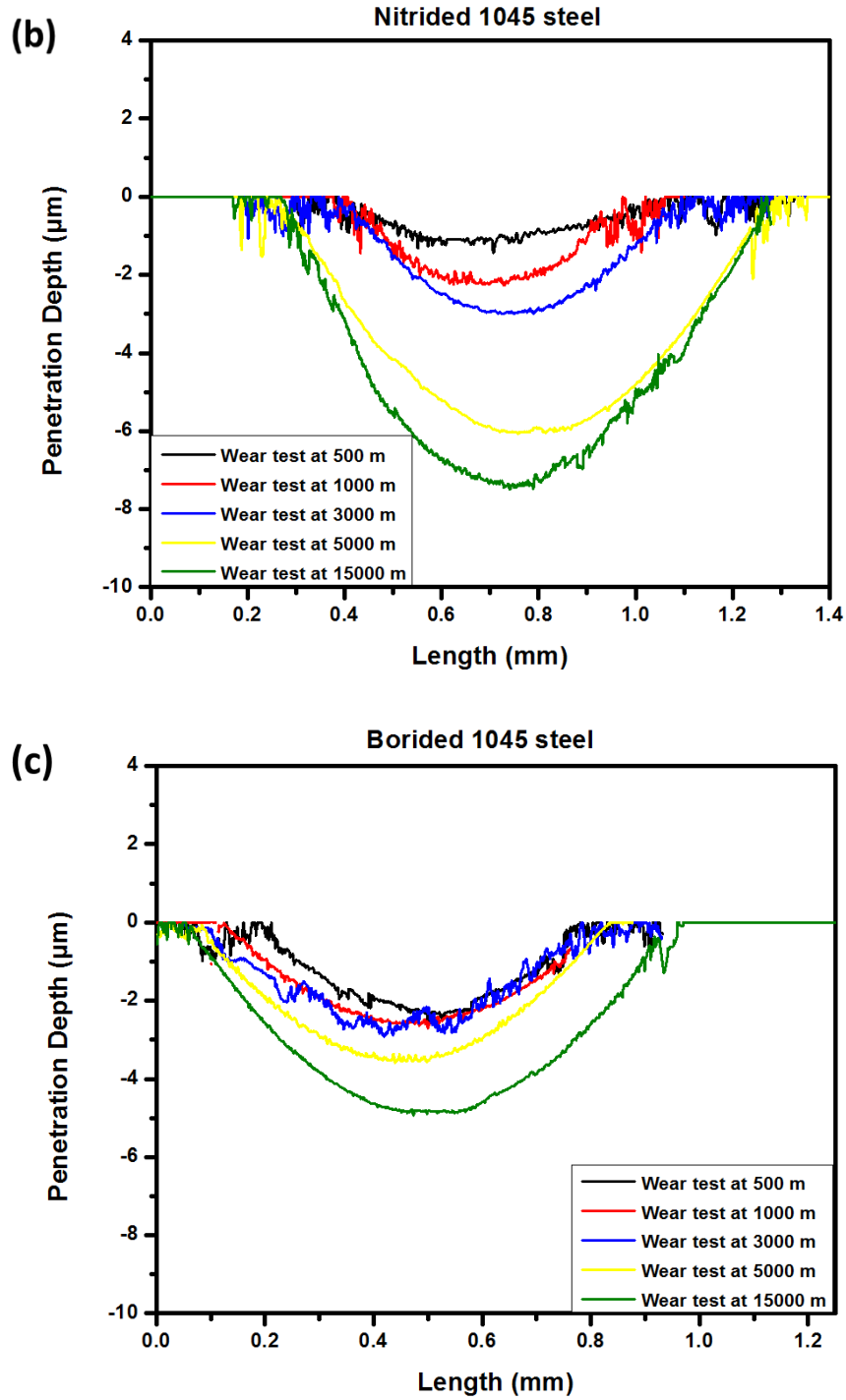
Figure 5.21 Wear scar geometric profiles of surface treated 1045 steel under lubricated sliding wear tests at different sliding distances with Peerless LLG, (a) oil quenched, (b) nitrided, (c) borided.
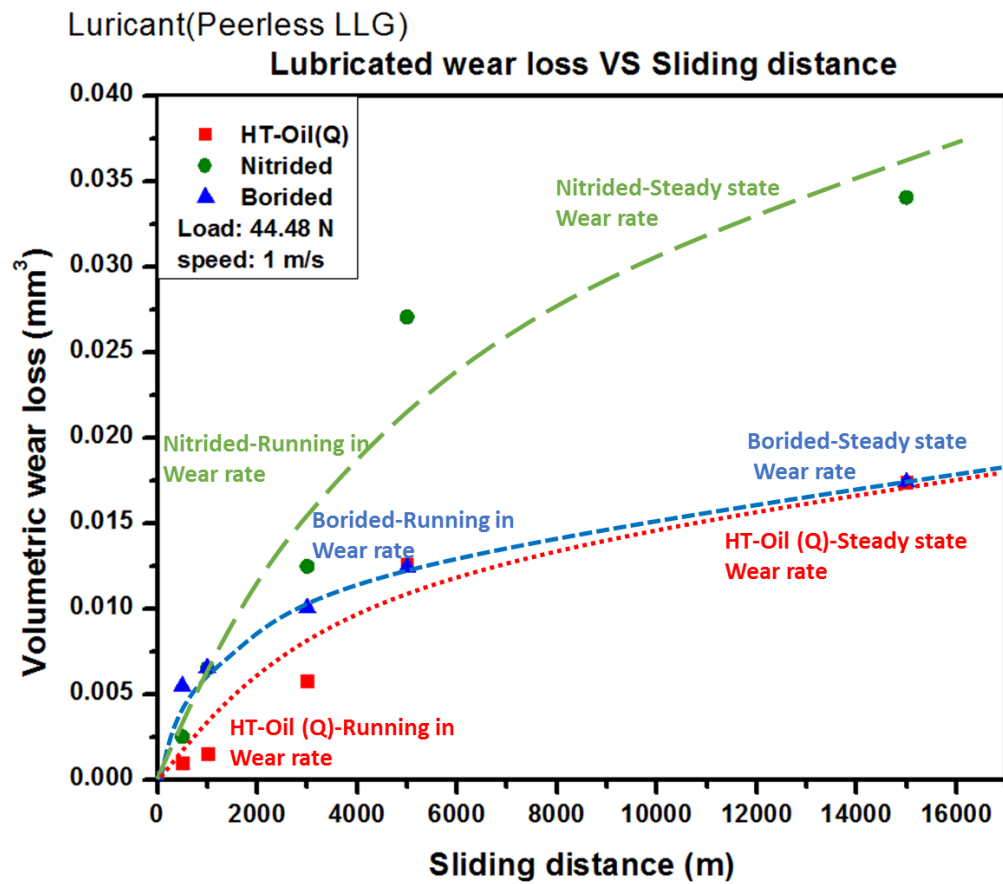
Figure 5.22 Wear volumetric losses against sliding distance curves for nitrided, borided and oil quenched 1045 steel under lubricated sliding tests with Peerless LLG.
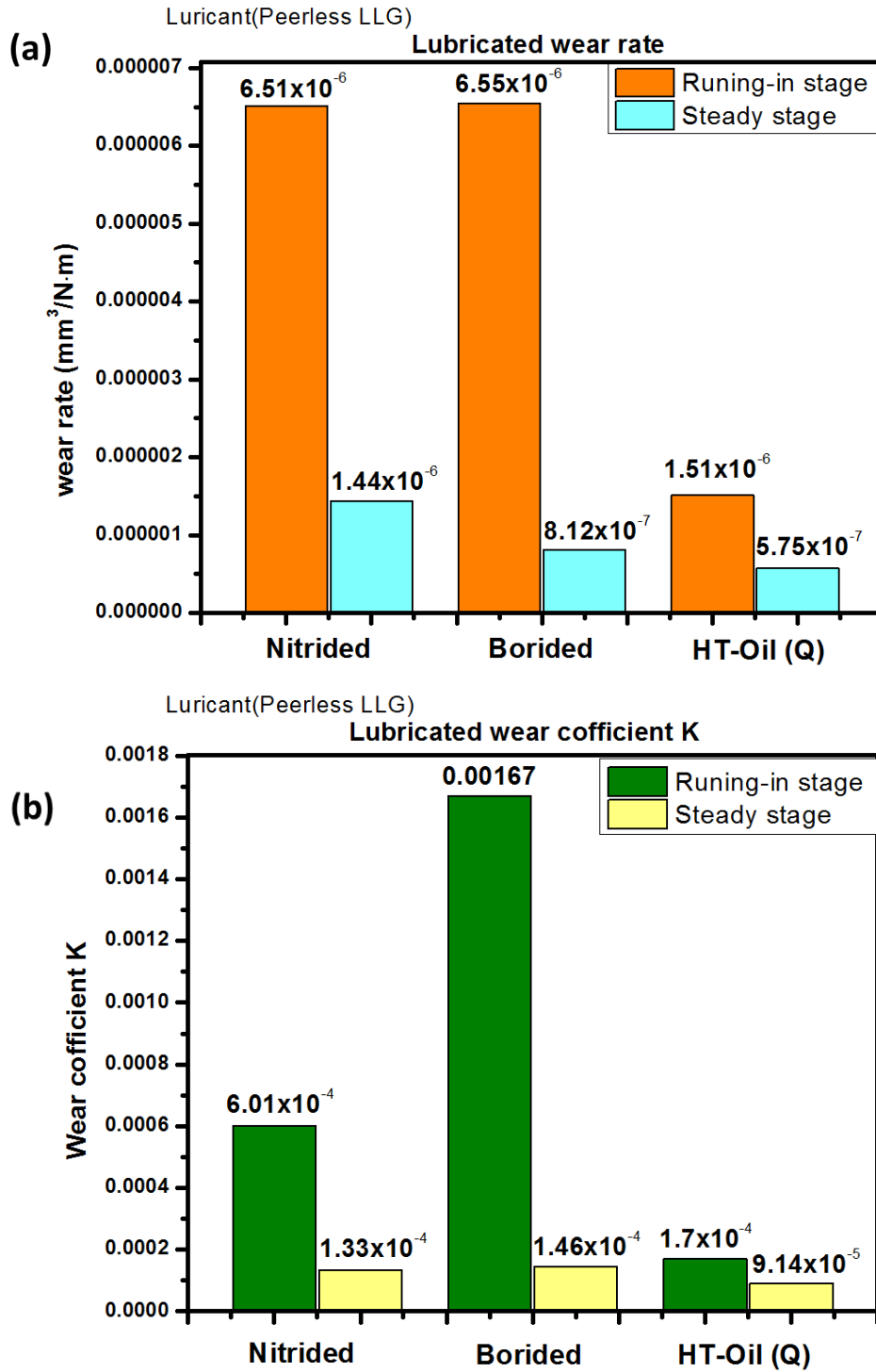
Figure 5.23 Wear rate and wear coefficient for nitrided, borided and oil quenched 1045 steel after lubricated sliding tests with Peerless LLG, (a) wear rate, (b) wear coefficient.
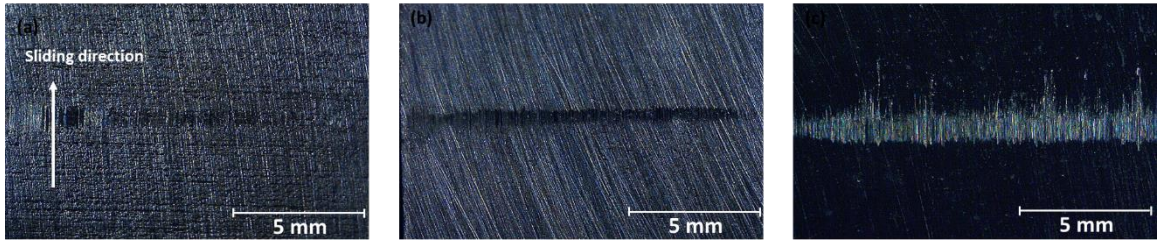
Figure 5.24 Lubricated wear track of oil quenched 1045 steel sample with different sliding distance (Lubricant: Peerless LLG), (a) 1000m, (b) 5000m, (c) 15000m.
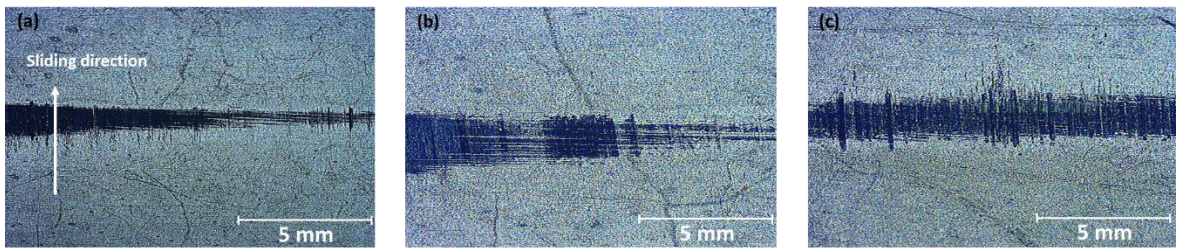
Figure 5.25 Lubricated wear track of nitrided 1045 steel sample with different sliding distance (Lubricant: Peerless LLG), (a) 1000m, (b) 5000m, (c) 15000m.
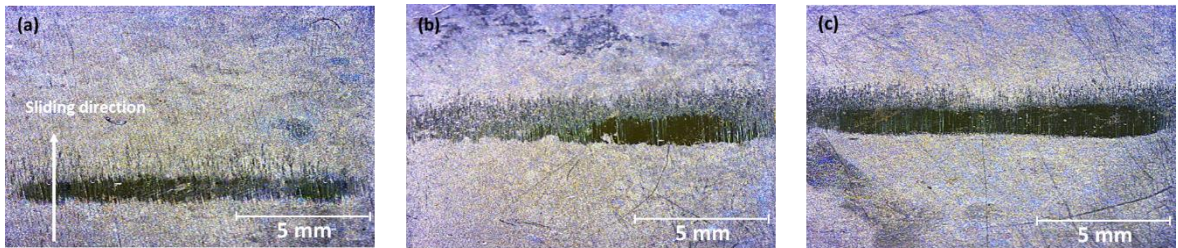
Figure 5.26 Lubricated wear track of borided 1045 steel sample with different sliding distance (Lubricant: Peerless LLG), (a) 1000m, (b) 5000m, (c) 15000m.
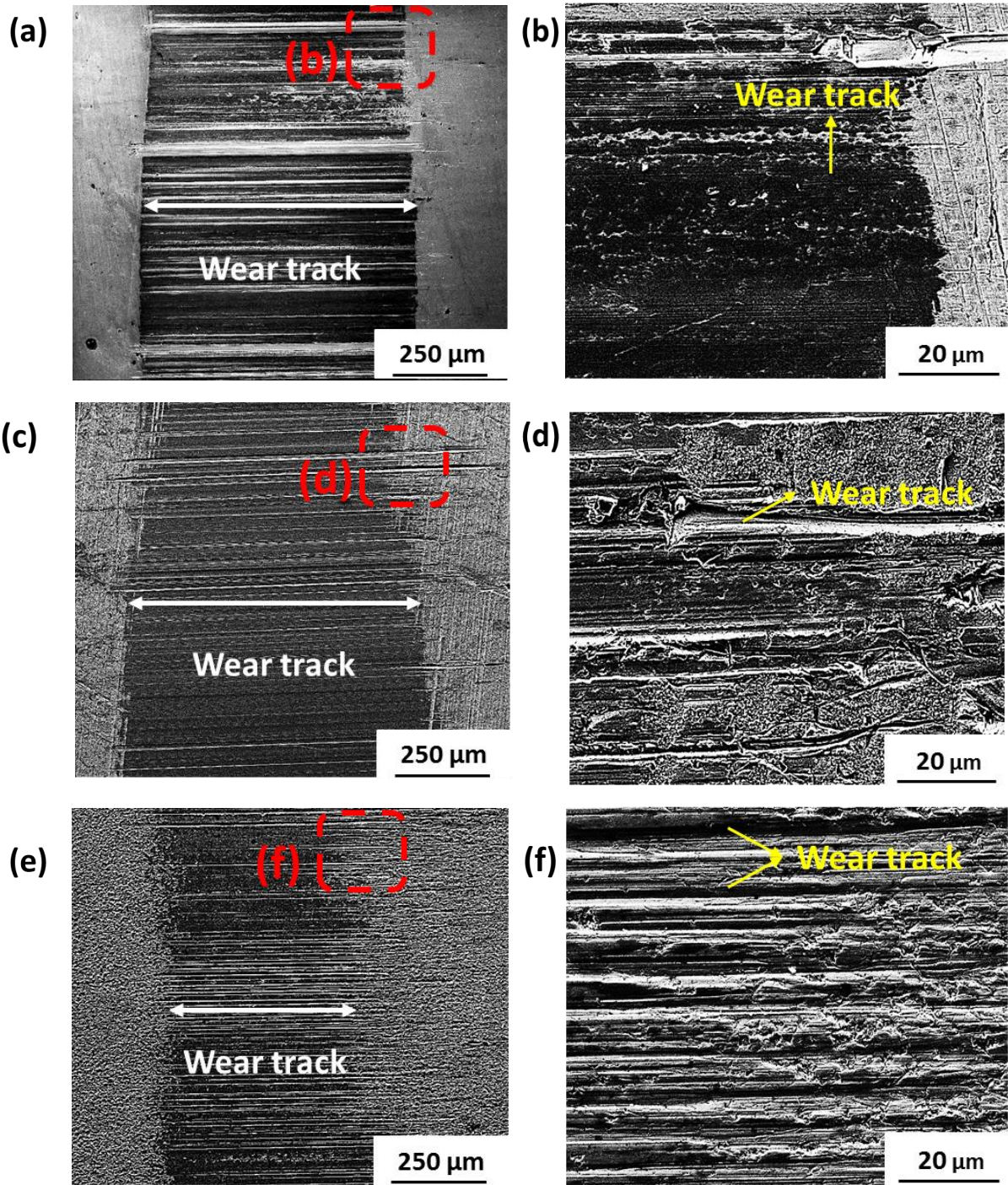
Figure 5.27 SEM micrographs of wear tracks on different surface treated 1045 steel after 15000 m lubricated sliding test, (a) oil quenched, (c) nitrided, (e) borided, high magnification image of the region marked as (b), (d), (f) in (a), (c), (e) respectively.

5.5 Effect of boric acid film on wear behaviour of borided 1045 steel

The borided 1045 steel exhibited excellent wear resistance in the dry and lubricated sliding tests (See Sections 5.2 and 5.3). In order to explore the role of the self-lubricating boric acid film (H_3BO_3) on the wear behaviour for borided steel, the dry sliding tests were conducted on the borided and SAP borided samples. Formation of a uniform film of self-lubricating boric acid (H_3BO_3) due to the spontaneous reaction between the boron oxide and relative humidity in the environment possibly results in the reduction in wear [128]. There are two criteria to form a boric acid film, one is the temperature should be over 750°C and the other is the relative humidity should be over 40% (RH). The borided sample treated with short annealing process (SAP) consisted of

1. Heating process: annealing the borided 1045 sample at 750 C for 5 minutes and then;
2. Cooling process: air cooling in a humidity controlled chamber with 40 % RH.

The boric acid film was generated by the following the two reactions [148]:

$$2B + \frac{3}{2}O_2 \rightarrow B_2O_3 \ (Heating \ process) \tag{11}$$

$$\frac{1}{2}B_2O_3 + \frac{3}{2}H_2O \rightarrow H_3BO_3 \ (Cooling \ process) \tag{12}$$
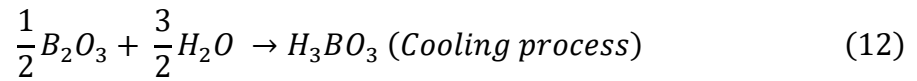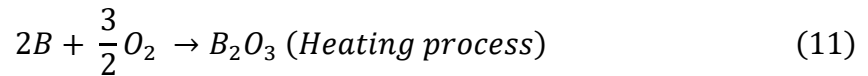
The heating process was such that the borided sample underwent oxidation at 750°C for the formation of boron oxide (B_2O_3); and the cooling process caused the boron oxide to have a reaction with hydrogen atoms to generate the (H_3BO_3) film.

The presence of the H_3BO_3 film on the surface of the boride layers was characterized by X-ray diffraction (XRD) and Raman spectroscopy. The results are shown in Figure 5.28 and 5.29 respectively. The iron boride phase, $Fe(BO_2)_2$ and ($FeO.B_2O_3$) were detected via XRD analysis (Figure 5.28). B_2O_3 and H_3BO_3 peaks and the distinct boric acid peak with the highlighted shouldering area have been identified through Raman spectroscopy analysis as shown in Figure 5.29.
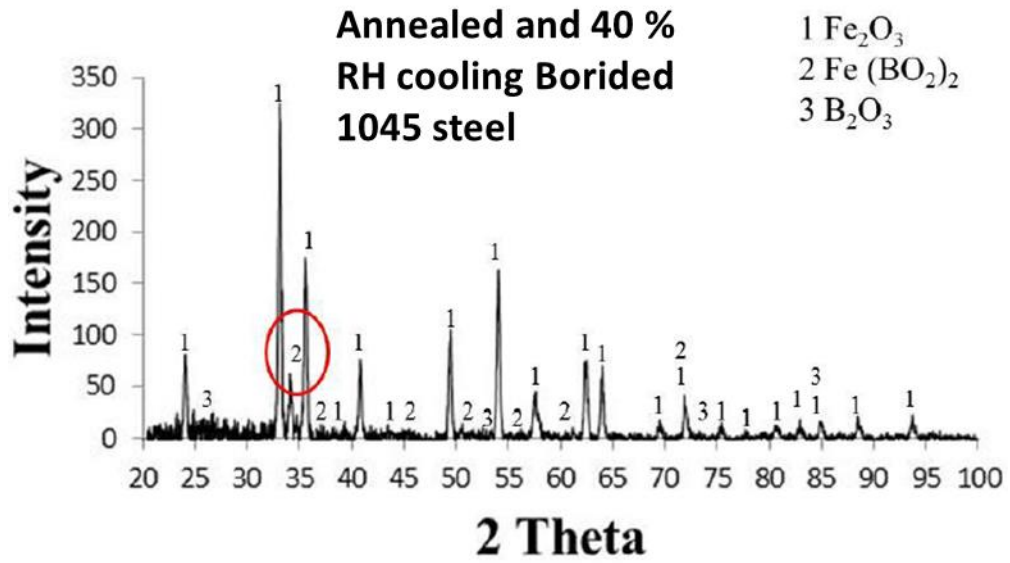
Figure 5.28 XRD spectra of borided 1045 steel after a short annealing process (SAP) and cooling in the presence of 40% of RH.
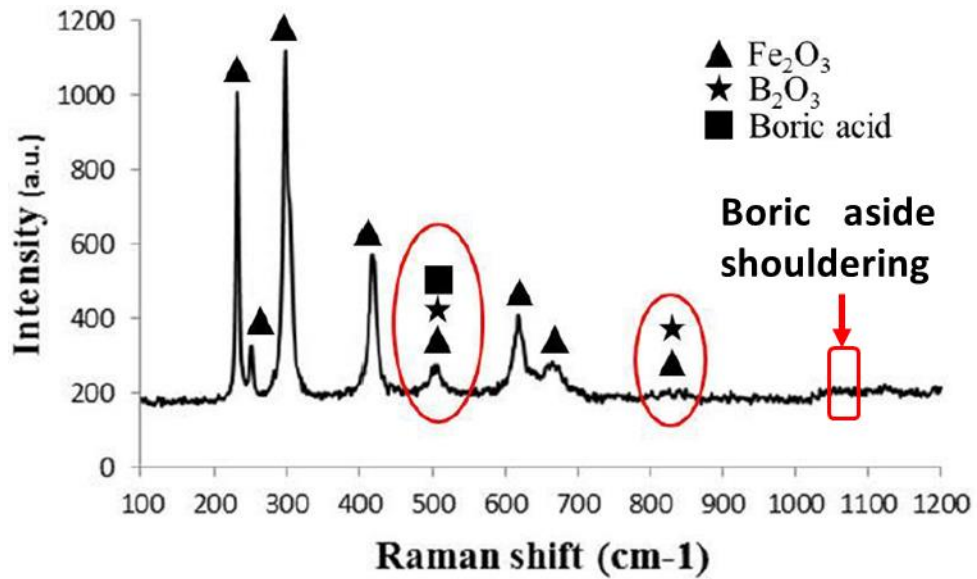
Figure 5.29 Raman spectra of annealed of borided 1045 steel samples and the H_3BO_3 (boric acid) surface film.

As the XRD and Raman results indicated, the probably phase formations during the annealing process in a humid environment could be described by the following equation between O_2 and Fe_2B:

$$6Fe_2B + 13O_3 + H_2O \rightarrow 2FeO.B_2O_3 + 5Fe_2O_3 + B_2O_3 \qquad (13)$$
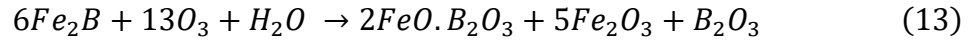
According to the results, it is possible to assume that a compact film of H_3BO_3 was formed on the surface of the SAP borided steel.

The borided and SAP treated 1045 samples were subjected to dry sliding wear test at a constant load of 44.48 N and a speed of 1 m/s under a controlled humidity atmosphere RH (25%). Figure 5.30 shows the volume losses of the borided and SAP samples after 1000 m dry sliding wear tests. The SAP sample presented a remarkably lower volume loss, namely about one order of magnitude reduction in wear compared to the borided sample that were not processed with SAP.
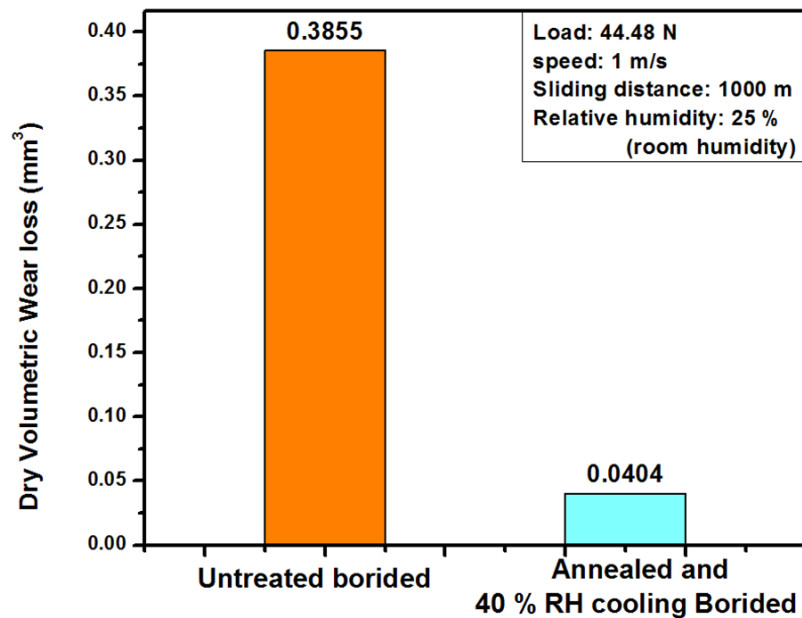
Figure 5.30 Wear volume losses of borided and SAP trated samples during block-on-ring dry sliding wear tests after 1000 m.

The Raman spectroscopy analysis was conducted on the worn surface after the sliding wear tests, and the results are shown in Figure 5.31. The boric acid layer was still detected in the SAP samples whereas the borided sample did not form such layer. This result confirmed that the generated boric acid film can be considered as a self-lubricating film that improves the ability of the surface to withstand sliding wear.
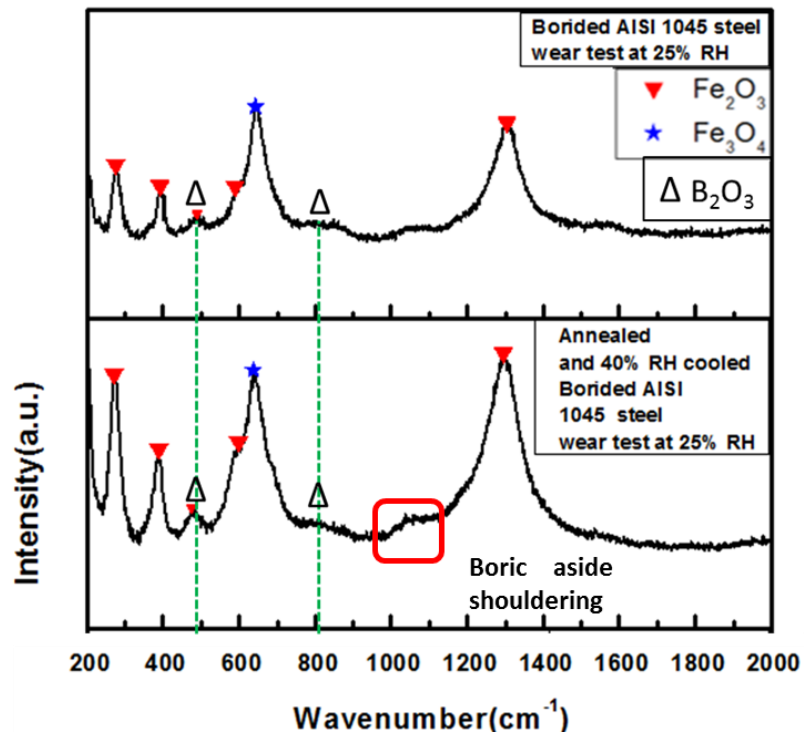
Figure 5.31 Raman spectra of the wear track for borided and SAP treated 1045 steel after 1000 m dry sliding wear tests.

CHAPTER 6

CONCLUSIONS

As mentioned in the Introduction, one of the intended applications of the heat treated 1045 steel in this research was an automotive pulley bore with a desired hardness and wear resistance. Heat treatments were conducted on AISI 1045 steel steel samples using an induction heater and three different quenching media encompassing salt, oil and water. The microstructures and wear performances of heat treated AISI 1045 steel steel were characterized after dry and lubricated sliding wear tests using a block-on-ring (AISI 52100 type steel) configuration. The wear test results were compared with those of the gas nitrided and electrochemically borided 1045 steel. The main conclusion could be summarized as follows:

1) Induction heating at 820 °C for 2 minutes and then quenching of AISI 1045 steel in the following modes: i) a salt bath composed of 60% KOH and 40% NaOH to 280 °C and holding for 15 seconds; and ii) quenching oil to 160 °C and holding for 15 seconds can both increase the hardness to over 500HV without the formation of quenching cracks. The second quenching method, i.e. the oil quenching, resulted in the highest bainite percentage (~19.5 %) consisted of lower bainitic and martensitic structures.

2) The gas nitriding process produced a compound layer thickness of 8-10 μm, a low surface roughness (0.35-0.37 μm, Ra), and the surface hardness values ranging between 310 HV-430 HV.

3) The hardened layer thickness in phase homogenization electrochemical borided (PHEB) sample was larger (72 μm), and the borided region showed the highest hardness values ranging between 1100 HV- 1300 HV.

4) Under dry and lubricated sliding wear tests, the wear resistance of AISI 1045 steel was improved greatly by the 820 °C induction heated treatments compared to the untreated 1045 steel, and the wear rates of 160 °C oil quenched sample with higher bainite content were lower than that of 280 °C salt quenched sample in both conditions.

5) The wear rate of the oil quenched partially bainitic steel in the dry sliding condition was determined as 2.13×10^{-6} mm^3/m in the steady-state wear period, which was over one order of magnitude lower than that of the nitrided and borided samples, and also much less than that of the untreated sample; the wear rate of the oil quenched bainitic steel in the lubricated sliding condition (Peerless LLG) was 5.75×10^{-7} mm^3/m, which was 50% lower than that of the nitrided sample.

6) The worn surface of untreated, oil quenched, nitrided and borided samples was covered by a tribolayer that consisted of a mixture of Fe_2O_3 and Fe_3O_4 phases generated by the friction heat. The wear was mainly dominated by oxidation wear of untreated and oil quenched samples, while the wear of nitrided and borided samples was dominated by adhesive wear. In addition, the oxidation degree on the worn surface of oil quenched samples was lower than that of the untreated sample.

7) The sliding wear induced microstructural changes at the surface and subsurface layer, (the plastically deformed layer) were observed below the wear tracks. The formation of a layer that consisted of fractured cementite was observed in the subsurface of oil quenched sample. The finer and more uniform carbides distributed in this layer were considered to reduce the wear rate.

8) By increasing the bainitic structures volume fraction in the mixed bainite-martensite microstructures, the wear resistance improved because of the relatively higher hardness and possibly higher toughness (no quenching cracks) compared with other microstructures.

9) The boric acid film generated by the SAP process (Heating at 750 °C for 5 minutes and cooling at 40 % RH) on borided 1045 steel was considered as a self-lubricated film that improves the ability to withstand sliding wear.

CHAPTER 7

RECOMMENDATIONS FOR FUTURE WORK

Based on this research, the following work is suggested to further understand the improvement of wear resistance on the surface treated 1045 steel:

1) The hardness and higher magnification SEM analysis of the fractured cementite layer should be further investigated to study the wear mechanism and examine whether the hardened layer improves the wear resistance.

2) Nanoindentation tests and TEM analysis of the possible hardened surface could be conducted to examine the bainitic structure hardened by reaustenitization at the surface with subsequent martensitic transformation.

3) The toughness of different surface treated 1045 steel could be investigated to observe how toughness correlates with wear resistance.

4) The coefficient of friction values of borided steel surface and those of the heat treated steel should be measured, which would provide further insight to the tribological properties of these surface treated steels.

5) The formation and effect of self-lubricating boric acid film should be identified on the surface of borided 1045 steel in higher relative humidity environment, i.e. 60% RH or even 80% RH. The effect of relative humidity on the tribological properties of borided and SAP borided AISI 1045 steel could be studied as well.

6) The cross-sectional SEM analysis of borided and SAP borided samples should be carried out, which can provide more information to compare the depth of abrasion and the depth of the deborided region after sliding wear tests.

7) Longer sliding distances such as 10000 m or 15000 m should be conducted on dry sliding tests to observe the wear behavior of nitrided and borided samples when the borided layer or nitrided compound layer is broken.

REFERENCES

[1] M.K. Singh. Application of Steel in Automotive Industry, International Journal of Emerging Technology and Advanced Engineering, 6(7), 2016.

[2] P. Dhanapal, S.S. Mohamed Nazirudeen. A Study of the Structure and Properties of High-Strength Bainite-Carbide Cast Iron with Globular Graphite. Metal Science and Heat Treatment, 53:578-83, 2012.

[3] D.H. Herring. A pictorial comparison of nitriding and carburizing industrial heating. [Online]. [Accessed: May. 12, 2010].

[4] H. Goto, Y. Amamoto. Improvement of wear resistance for carbon steel under unlubricated sliding and variable loading conditions. Wear, 270: 725-736, 2011.

[5] K.H. Zum Gahr. Microstructure and wear of materials, Elsevier New York, 1987

[6] S. Yuli, Z. Xiaoqian, G. Guoyou, Z. Shiquan. New technique of superplasticization of hypoeutectoid steel. Advances in Engineering Plasticity and its Applications. Elsevier, 1035-1040, 1993

[7] W. D. Callister, Jr., Materials Science and Engineering: An Introduction 7th Edition. Wiley, 2007.

[8] Classification of Carbon and Low-Alloy Steels. Key to Metals AG. [Online]. [Accessed: Nov. 6, 2018].

[9] AISI Carbon Steel Mechanical Characteristics – Yield, Tensile, Hardness. Engineers Edge. [Online]. [Accessed: Nov. 6, 2018].

[10] Materials: Carbon Steel, Coburn-Myers Fastening Systems Incorporated. [Online]. [Accessed: Nov. 6, 2018].

[11] B. Index, Carbon Steel and Mild Steel: The Basics, Reliance Foundry. [Online]. [Accessed: Nov. 6, 2018].

[12] K. Holmberg, A. Mathews. Coatings Tribology, Property, Techniques and Application in Surface Engineering, Elsevier, 1994.

[13] K.S. Narasimhan, F.J. Semel. Sintering of powder mixtures and the growth of ferrous powder metallurgy. Materials Chemistry and Physics, 67(1):56-65, 2001.

[14] K.K. Khan, M. Mehmood, M. Hassan, J. Ahmad, Z. Iqbal, T. Muddasser. Gas Nitriding of Electrodeposited Ni-W Alloys. Metal Science and Heat Treatment, 53:87-90, 2011.

[15] E.J. Mittemeijer, M. Planck. Fundamentals of Nitriding and Nitrocarburizing, ASM Handbook, 4(A), 2013.

[16] S. Abisset, F. Maury, R. Feurer, M. Ducarroir. Gas and plasma nitriding pretreatments of steel substrates before CVD growth of hard refractory coatings. Thin Solid Films, 315:179-85, 1998.

[17] A.G. Von Matuschka: Boronizing, Heyden and Son Inc., Philadelphia, PA, 23, 1980.

[18] A.K. Sinha. Heat Treating: Boriding (Boronizing) of Steels, ASM Handbook, 1991.

[19] M. Kulka, N. Makuch, P. Dziarski. Gradient boride layers formed by diffusion carburising and laser boriding. Optics and Lasers in Engineering, 67:163-175, 2015.

[20] M. Bektes, A. Calik, N. Ucar. Pack-boriding of the Fe-Mn binary alloys: Characterization and kinetics of the boride layers. Materials Characterization, 61:233-239, 2010.

[21] R. Nora, T. Mohamed Zine, K. Abdelkader, K. Youcef, O. Ali, X. Jiang. Boriding and boronitrocarburising effects on hardness, wear and corrosion behavior of AISI 4130 steel. Revista Material, 24(01), 2019.

[22] B. Matijevic. Evaluation of boride layer growth on carbon steel surfaces, Metal Science and Heat Treatment, 56: 269-273, 2014.

[23] G. Kartal, S. Timur, V. Sista, O.L. Eryilmaz, A. Erdemir, The growth of single Fe$_2$B phase on low carbon steel via phase homogenization in electrochemical boriding (PHEB), Surface & Coating Technology, 206:2005-2011, 2011.

[24] S. Güldem, V. Timur, New Environmentally-Friendly Technologies in Coating of Metal Borides, Istanbul Technical University, 2019.

[25] V. Rudnev, D. Loveless, R. Cook, M. Black. Heat Treatment of Metals 4, 97-103, 2003.

[26] D. Rodman, C. Krause, F. Nurnberger, FW. Bach, K. Haskamp, M. Kastner, E. Reithmeier. Steel. Res. Int. 82:329-336, 2011.

[27] J. Grum, V. Rudnev, Int. J. Mater. Prod. Tec. 29:1-8, 2007.

[28] D. Rodman, B. Boiarkin, F. Nurnberger, A. Dalinger, M. Schaper, Steel Res Int 85: 741-755, 2014.

[29] G. Ibrahim, Ö. Melih. Investigation of adhesion and wear properties of borided AISI steel. Materials Science and Technology, 50(2):269, 2016.

[30] R.E. Haimbaugh. Practical Induction Heat Treating, ASM International, Materials Park, OH, U.S.A., 3-284, 2001.

[31] V. Rudnev, D. Loveless, R. Cook and M. Black, Handbook of Induction heating, Marcel Dekker Inc, New York, U.S.A., 11-14, 2003.

[32] Davis JR. Cast irons. Materials Park, OH: ASM International, 1996.

[33] D.S. MacKenzie, The Time-Temperature-Transformation Curve, FASM Gear solutions, 2018.

[34] M.V. Boniardi, C. Milanino, Steel metallurgy volume I, 2017.

[35] American Society for Metals. Heat Treaters Guide Standard Practice and Procedures for Steel. Metals Park, OH: ASM International, 423-426, 1982.

[36] V. Cárdenas, E.E. Lewis, R.M. Pérez, A.I. Bernal Ponce. Characterization and wear performance of boride phases over tool steel substrates. Advances in Mechanical Engineering, 2016.

[37] H. Ohtani, S. Okaguchi, Y. Fujishiro, Y. Ohmori, Morphology and properties of low-carbon bainite, Metallurgical transactions, 21(A), 1990.

[38] B.D. Craig, G. Krauss, The structure of tempered martensite and its susceptibility to hydrogen stress cracking, Metallurgical transactions, 11(A), 1980.

[39] K. Gall, T.J. Lim, D.L McDowell, H. Sehitoglu, Y.I Chumlyakov. The Role of Intergranular Constraint on the Stress-induced Martensitic Transformation in Textured Polycrystalline NiTi. Int. J. Plasticity 16(10–11):1189–1214, 2000.

[40] V.I. Levitas. Thermomechanical Theory of Martensitic Phase Transformations in Inelastic Materials. Int. J. Solids Structures 35(9–10): 889–940, 1998.

[41] G. Krauss. Martensitic Transformation, Structure and Properties in Hardenable Steels, in Hardenability Concepts with Applications to Steel, D.V. Doane and J.S. Kirkaldy, eds., AIME, Warrendale, PA, 229-248, 1978.

[42] E. Boyle. Microstructural Effects on the Mechanical Properties of Carburized Low Alloy Steels. Mechanical, Automotive and Materials Engineering Department (Master Thesis), University of Windsor, Windsor, 4-102, 2007.

[43] J. Pacyna. Retained Austenite in the Cracking Process of Steel on the Working Rolls of the Cold Sheet Rolling Mill, Steel Research 63, 500-503.1992.

[44] A.C. Foecke, Transformation Potential Predictions for the Stress-induced Austenite to Martenite Transformation in Steel. Acta Materialia, 58:85-91, 2010.

[45] X.D. Wang, B.X. Huang, Y.H. Rong. Microstructures and Stability of Retained Austenite in TRIP Steels. Materials Science and Engineering A, 438-440:300-305, 2006.

[46] W.D. Callister. Materials Science and Engineering-An Introduction, 7th Edition, York, PA, U.S.A, John Wiley and Sons, 253-360, 2007.

[47] T. Nasir. Design of Heat Treatment for Production of Austempered Ductile Iron (ADI) with Targeted Automotive Applications, Mechanical, Automotive and Materials Engineering Department (M.A.Sc Thesis), University of Windsor, Windsor, 10-76, 2011.

[48] J. T. Burwell. Survey of possible wear mechanism. Wear, 1:119-141, 1958.

[49] K.H. Zum Gahr, Microstructure and wear of materials, Elsevier, New York, 1987.

[50] A.R. Riahi, A.T. Alpas, Wear map for grey cast iron, Wear, 255:401-409, 2003.

[51] S. Lim, M.F. Ashby, Wear mechanism maps, Acta Metall, 35:1-24, 1987.

[52] I. M. Hutchings, Tribology: friction and wear of engineering materials, London: CRC Press, 1992.

[53] J. Zhang, A.T. Alpas. Transition between mild and severe wear in aluminium alloys. Acta Mater, 45:513-528, 1997.

[54] I I. Garbar, Dry Sliding Wear Behavior of a High-Mn Austenitic Twinning Induced Plasticity (TWIP) Steel Microalloyed with Ti, Tribo. Int. 35:749-755, 2002.

[55] H. So, The mechanism of oxidational wear, Wear 184:161-167, 1995.

[56] H. So, D.S. Yu, C.Y. Chuang, D.S., Chuang, C.Y. Formation and wear mechanism of tribo-oxides and the regime of oxidational wear of steel. Wear 253:1004-1015, 2002.

[57] S.C. Lim, The relevance of wear-mechanism maps to mild-oxidational wear. Tribology International. 35:717-723, 2002.

[58] Y.C. Lin, S. W. Wang, and T. M. Chen. A study on the wear behavior of hardened medium carbon steel. Journal of Materials Processing Technology, 120:126-132, 2002.

[59] M.A. Moore. Fundamentals of friction and wear of materials. ASM international, OH, Metals Park, OH, 1981.

[60] K.H. Zum-Gahr. Microstructure and wear of materials. Elsevier, 1981.

[61] H.S. Avery. Work hardening in relation to abrasion resistance. Climax molybdenum company, Greenwich, Conn, USA, 1974.

[62] J. Yang, T.S. Wang, B. Zhang, F.C. Zhang. Sliding wear resistance and worn surface microstructure of nanostructured bainitic steel. Wear, 282:81-84, 2012.

[63] H. Mohrbacher, D. Jarreta. Technology properties and applications of niobium carbide reinforced steel and iron alloys, CBMM, IMOA and TMS, 2, 2015.

[64] N.N. Serpik and M.M. Kantor. Effect of heat treatment on abrasive resistance of steels for earth moving equipments. Metalloved. Obrab. Met., 7:46-50, 1958.

[65] T. Chandrasekaran, K.A. Natarajan, and Kishore. Influence of microstructure on the wear of grinding media. Wear, 147:267-274, 1991.

[66] Y. Wang, L. Pan, and T. C. Lei. Sliding wear behavior of pearlitic structures in eutectoid steels. Wear, 143:57-69, 1991.

[67] Y. Wang and T. Lei. Wear behavior of steel 1080 with different microstructures during dry sliding. Wear, 194:44-53, 1996.

[68] P. L. Hurricks. Overcoming industrial wear. Industrial lubrication and tribology, 345-356, October 1971.

[69] A.J. Perez-Unzueta, J.H. Beynon. Microstructure and wear resistance of pearlitic rail steels. Wear, 164:173-82, 1993.

[70] U.P. Singh, R. Singh. Wear investigation of wheel and rail steels under conditions of sliding and rolling-sliding contact with particular regard to microstructural parameters. Wear, 170:93-9, 1993.

[71] A.P.G Chaves. Railway wheels: analysis, microstructure and improvement proposals [dissertation]. São Paulo: Polytechnic School, University of São Paulo, 2017.

[72] K.C. Barker. The development of abrasive-corrosive wear resistance of steels by microstructural control. PhD thesis, University of Cape Town, 1988.

[73] D.E. Diesburg and F. Borik. Optimizing abrasion resistance and toughness in steel and irons for the mining industry. In Materials for the Mining Industry, Ann Arbor, MI, 14-41, 1974.

[74] J. Suchanek and V. Kuklik. Inuence of heat and thermochemical treatment on abrasion resistance of structural and tool steels. Wear, 267:2100-2108, 2009.

[75] N. Prasad and S.D. Kulkarni. Relations between microstrcuture and abrasive wear of plain carbon steel. Wear, 63:329-338, 1980.

[76] S. Denis, S. Sjostrom, A. Simon. Coupled temperature, stress, phase transformation calculation model numerical illustration of the internal stresses evolution during cooling of a eutectoid carbon steel cylinder. Metallurgical and Materials Transactions A, 18(A):1203, 1987.

[77] R.C.D. Richardson. The wear of metals by hard abrasives. Wear, 10:291-309, 1967.

[78] L. Xu and N. F. Kennon. A study of the abrasive wear of carbon steels. Wear, 148:101-112, 1991.

[79] P. L. Hurricks. Overcoming industrial wear. Industrial lubrication and tribology, 345-356, 1971.

[80] A. Misra, I. Finnie. A review of the abrasive wear of metals." Journal of Engineering Materials and Technology 104, 2:94-101, 1982.

[81] L.Q. Xu. Abrasive wear of ferrous alloys, 1991.

[82] J. Lefevre, and K.L. Hayrynen. Austempered materials for powertrain applications. Journal of materials engineering and performance 22, 7:1914-1922, 2013.

[83] M.A. Moore. The relationship between the abrasive wear resistance, hardness and microstructure of ferritic materials. Wear 28, 1: 59-68, 1974.

[84] F.G. Caballero, C. Capdevila, J. Chao. The microstructure of continuously cooled tough bainitic steels. Materials Science and Technology, 2012

[85] H.K.D.H Bhadeshia. New bainitic steel by design. The Minerals, Metals and Materials Society, PA USA, 69, 1998.

[86] H.K.D.H Bhadeshia. Nanostructured bainite. Proc Royal Society, London, A466:3, 2010.

[87] H.K.D.H Bhadeshia. The nature, mechanism and properties of strong bainite. ISIJ, proceedings of the 1st International Symposium on the Steel Science, 2007.

[88] C.Y. Chen, C.C. Chen, J.S. Lin. Morphology feature of nanostructure bainitic steel after tempering treatment. International Journal of Chemical and Molecular Engineering, 8, 2014.

[89] M.M. Khruschov. In Conference on Lubrication and Wear, 655, 1957.

[90] M.M. Khrushchov and M.A. Babichev. Friction and wear in machinery, Translated from the Russian, American Society of Mechanical Engineers, (12):5, 1960.

[91] M.M. Khruschov. Principles of abrasive wear. Wear, 28:69-88, 1974.

[92] M.M. Khruschov and M.A. Babichev. Investigations into the wear of metals. USSR Academy of Sciences (in Russian), 1960.

[93] E. Rabinowicz, L.A. Dunn, and P.G. Russel. A study of abrasive wear under three-body conditions. Wear, 4:345-355, 1961.

[94] J. Goddard, H.J. Harker, and H. Wilman. A theory of the abrasion of solids such as metals. Nature, 184:333-335, 1959.

[95] P.L. Hurricks. Overcoming industrial wear. Industrial lubrication and tribology, 345-356, 1971.

[96] S.M. Nahvi, P.H. Shipway, and D.G. McCartney. Particle motion and modes of wear in the dry sand-rubber wheel abrasion test. Wear, 267:2083-2091, 2009.

[97] J.G. Chacon-Nava, A. Martinez-Villafane, F. Almeraya-Calderon, J.A. Cabral-Miramontes, and M.M. Stack. Some remarks on particle size effects on the abrasion of a range of Fe based alloys. Tribology International, 43:1307-1317, 2010.

[98] B.W.E. Avient, J. Goddard, and H. Wilman. An experimental study of friction and wear during abrsion. Proceedings of the Royal Society London A, 258:159, 1960.

[99] J. Larsen-Badse. The abrasion resistance of some hardened and tempered carbon steels. Transactions of the Metallurgical Society AIME, 236:1461, 1966.

[100] A. Sundstrom, J. Rendon, and M. Olsson. Wear behaviour of some low alloyed steels under combined impact/abrasion contact conditions. Wear, 250:744-754, 2001.

[101] R. Rybiak, S. Fouvry, B. Bonnet, Fretting wear of stainless steels under variable temperature conditions: introduction of a composite wear law, Wear, 268: 413–423, 2010.

[102] T. Kayaba, A. Iwabuchi, The fretting wear of 0.45% C steel and austenitic stainless steel from 20 to 6501C in air, Wear, 74:229–245, 1981.

[103] M. Lou, D.R. White, A. Banerji, A.T. Alpas, Dry and lubricated friction behaviour of thermal spray low carbon steel coatings: Effect of oxidational wear, Wear, 432–433, 2019.

[104] O.P. Modi, B.K. Prasad, A.K. Jha, R. Dasgupta, and A.H. Yagneswaran. Low-stress abrasive wear behaviour of a 0.2% C steel: influence of microstructure and test parameters. Tribology Letters, 15:249-255, 2003.

[105] P.L. Hurricks, Fretting wear of mild-steel from room-temperature to 2001 °C, Wear 19:207–229, 1972.

[106] P.L. Hurricks, Fretting wear of mild-steel from 2001 °C to5001 °C, Wear, 30:189–212, 1974.

[107] W.T. Clark, C. Pritchard, J.W. Midgley, Mild wear of unlubricated hard steels in air and carbon dioxide, Proceedings of the Institution of Mechanical Engineers, Conference Proceedings 182:97–105, 1967.

[108] R.T. Foley, M.B. Peterson, C. Zapf, Frictional characteristics of cobalt, nickel, andiron as influenced by their surface oxide films, ASLE Transactions 6:29–39, 1963.

[109] H. Tian, N. Saka, N.P. Suh. Boundary lubrication studies of undulated titanium surfaces. Tribol Trans 32:289–96, 1989.

[110] G.W. Stachowiak, A.W. Batchelor, Engineering Tribology; Lubricants and Their Composition, Butterworth–Heinemann, Boston, 2001.

[111] R.A. Saravanan, J.M. Lee, S.B. Kang, Dry sliding wear behavior of A356-15Pct SiCp composites under controlled atmospheric conditions. Metallurgical and Materials Transactions A, 30:2523–2538, 1999.

[112] B. K. Yen, and T. Ishihara. Effect of humidity on friction and wear of Al–Si eutectic alloy and A1–Si alloy-graphite composites. Wear, 198:169-175, 1996.

[113] W.A. Brainard, D.H. Buckley, Dynamic-scanning-electron-microscopy study of friction and wear, NASA Technical Note TN D-7700, (National Aeronautics and Space Administration), 1974.

[114] N.P. Gravier, E.C. Cutiongo, Y.W. Chung, Effect of testing environments on friction and bidirectional material transfer during dry sliding of 3004-aluminum against H13 steel. Tribol. Trans. 38:168–172, 1995.

[115] H. Goto, K. Uchijo. Wear mechanism of Al–Si alloy impregnated graphite composite under dry sliding. Wear, 259: 613–619, 2005.

[116] P.A. Thornton, V.J. colangelo. Fundamentals of Engineeing materials, 1985.

[117] G.K. Sireli, P. Ozkalafat, S. Timur. Surface modification of chromium-silicon martensitic steel by forming hard borides, Surface & Coatings Technology, 326:18-27, 2017.

[118] Y. Pan, B. Wang, G.C. Barber, Study of bainitic transformation kinetics in SAE52100 steel, Journal of Materials Research and Technology, 8(5):4569-4576, 2019.

[119] D.M. Stefanescu. ASM Handbook VI Properties and selection: Irons, Steels and high performance alloys 10th edition ASM international Materials Park, OH, 255:1166, 1992.

[120] V. Rudnev, D. Loveless, R. Cook, M. Black, Heat Treatment of Metals, 4:97-103 2003.

[121] D. Rodman, C. Krause, F. Nurnberger, FW. Bach, K. Haskamp, M. Kastner, E. Reithmeier, Steel. Res. Int. 82:329-336, 2011.

[122] J. Grum, V. Rudnev, Int. J. Materials and Product Technology. 29:1-8, 2007.

[123] D. Rodman, B. Boiarkin, F. Nurnberger, A. Dalinger, M. Schaper, Steel Res Int. 85:741-755, 2014.

[124] D. Rodman, F. Nurnberger, A. Dalinger, M. Schaper, C. Krause, M. Kastner, E. Reithmeier, Steel. Res. Int. 85:415- 425, 2014.

[125] A. Çalik, Effect of cooling rate on hardness and microstructure of steels, International Journal of Physical Sciences, 4(9):514-518, 2009.

[126] Trzaska J. Calculation of critical temperature by empirical formulas. Arch. Metall. Mater, 61(2B):981, 2016.

[127] L.C.F. Canale, L. Albano, G.E. Totten, L. Meekisho, Thermal Engineering of Steel Alloy Systems, Comprehensive materials processing, 12:39-37. 2014.

[128] E. Hernández-Sanchez, A. Chino-Ulloa, J.C. Velazquez, Effect of Relative Humidity on the Tribological Properties of Self-Lubricating H_3BO_3 Films Formed on the Surface of Steel Suitable for Biomedical Applications. Advances in Materials Science and Engineering, 2015.

[129] A. Erdemir, C. Bindal, C. Zuiker, and E. Savrun, Tribology of naturally occurring boric acid films on boron carbide. Surface and Coatings Technology, 86-87(2):507–510, 1996.

[130] S. Ray. MTech dissertation. Indian Institute of Technology, Kanpur, 1969.

[131] J.F. Archard, W. Hirst, The Wear of Metals Under Unlubricated Conditions, Proceedings of the Royal Society of London, 236:397-410, 1956

[132] M.A.Y. Gonzalez, Modelling the Microstmcture and Mechanical Properties of Austempered Ductile Irons, in Department of Materials Science and Metallurgy (PhD Thesis), University of Cambridge, Cambridge, 5-183, 2001.

[133] V.F. Zackay and H.I. Aaronson: Decomposition of Austenite by Diffusional Processes, Interscience Publishers, New York, 1962.

[134] D. Quidort and Y.J.M. Brechet. Isothermal growth kinetics of bainite in 0.5% C steels, Acta Mater., 49, 4161–4170, 2001.

[135] T. F. J. Quinn, Role of oxidation in the mild wear of steel. British Journal of Applied Physics, 13:33-37, 1962.

[136] S.M. Shariff, T.K. Pal, G. Padmanabham, et al. Comparative study on dry sliding wear behavior of various railroad steels. J Tribol. 133(2):021602, 2011.

[137] R. Rementeria, I. Garcia, M.M. Aranda, et al. Reciprocating-sliding wear behavior of nanostructured and ultra-fine high-silicon bainitic steels. Wear. 338-339:202-209, 2015.

[138] R.J. Thibeau, C.W. Brown, R.H. Heidersbach. Raman Spectra of Possible Corrosion Products of Iron. Applied Spectroscopy, 32:532-535, 1978.

[139] D.L.A. De Faria, S.V. Silva, M.T. De Oliveira, Journal of Raman Spectroscopy, 28:873-878, 1997.

[140] G. Zheng, Y. Yao, S. Zhang, S. Wan. Structural studies of a $Li_2O_4B_2O_3$ melt by high temperature Raman spectroscopy and density functional theory, Royal society of chemistry, 19:5695-5816, 2017.

[141] H. Chen, C. Zhang, W. Liu, et al. Microstructure evolution of a hypereutectoid pearlite steel under rolling/sliding contact loading. Mat Sci Eng A. 655:50-59, 2016.

[142] C.M. Bae, W.J. Nam, S.L. Chong. Effect of microstructural features on ductility in hypo-eutectoid steels. ScrMater, 41(6):605–610, 1999.

[143] M. Wang, J. Shan, C. Zheng, et al. Effects of deformation and addition of aluminium on spheroidisation of high-carbon-bearing steel. Mater Sci Technol, 34(2):161–171 2018.

[144] M. Wang, C. Zhang, D. Sun, Z. Yang and F. Zhang. Wear behaviour and microstructure evolution of pearlitic steels under block-on-ring wear process. Materials Science and Technology, 35(10):1149–1160, 2019.

[145] N. Jin and P. Clayton. Effect of microstructure on rolling/sliding wear of low carbon bainitic steels. Wear, 202:202-207, 1997.

[146] P. H. Shipway, S. J. Wood, and A. H. Dent. The hardness and sliding wear behaviour of a bainitic steel. Wear, 203-204:196-205, 1997.

[147] P. Clayton and N. Jin. Unlubricated sliding and rolling/sliding wear behavior of continuously cooled low/medium carbon bainitic steels. Wear, 200:74-82, 1996

[148] A. Erdemir, M. Halter, and G. R. Fenske. Preparation of ultralow-friction surface films on vanadium diboride. Wear, 205(1-2):236–239, 1997.

[149] H. Kuhn, D. Medlin. ASM Handbook: mechanical testing and evaluation. ASM International, 8, 2000.

[150] J.K. Odusote, T.K. Ajiboye, B. Rabiu. Evaluation of Mechanical Properties of Medium Carbon Steel Quenched in Water and Oil. J. Miner. Mater. Charact. Eng., 11(09):859, 2012.

[151] P.P. Ikubanni, A.A. Adediran, A.A. Adeleke, K.R. Ajao, O.O. Agboola. Mechanical Properties Improvement Evaluation of Medium Carbon Steels Quenched in Different Media. Int. J. Eng. Res. Africa, 32:1–10, 2017.

[152] R. Karimbaev, S. Choi, Y.S. Pyun and A. Amanov. Mechanical and Tribological Characteristics of Cladded AISI 1045 Carbon Steel. Materials, 13:859, 2012.

[153] B. Podgornik, J. Vizintin, O. Wanstrand, M. Larssons. Tribological properties of plasma nitrided and hard coated AISI 4140 steel. Wear, 249:254-259.

[154] B. Santosh, K. Hari. Tribology of nitrided-coated steel-a review. Archives of Mechanical Technology and Materials. 37:50-57, 2017.

[155] H. Kato, T.S. Eyre, B. Ralph. Wear mechanism map of nitrided steel. Acta Metallurgica et Materialia, 42(5):1703-1713,1994.

[156] W.T. Clark, C. Pritchar, J.W. Midgley, Proceedings of the Institution of Mechanical Engineers, 182:97-106, 1967-68.

[157] S.R. Pearson, P.H. Shipway, J.O. Abere, R.A.A. Hewitt. The effect of temperature on wear and friction of a high strength steel in fretting. Wear, 303:622-631, 2013.

[158] J. Vetter, G. Barbezat, J. Crummenauer, J. Avissar. Surface treatment selections for automotive applications. Surface and Coatings Technology, 200(5–6): 1962-1968, 2005.

[159] D. Bakshi. Wear of fine pearlite, nanostructured bainite and martensite, Department of Materials Science and Metallurgy Darwin College (Doctoral thesis), University of Cambridge, 2017.

APPENDICES

Industrial interests: Lubricated sliding wear behaviour of surface treated 1045 steel with lubricant Krytox.

In order to compare tribological compatibility between two lubricants, the nitrided and oil quenched samples was selected to conduct the lubricated wear tests with a new type of lubricant, perfluoropolyether (PFPE) grease (Krytox). The samples were tested with the same condition at 1 m/s speed, 44.45 N load and the lubricated volumetric wear loss with Krytox was shown in Figure A.1 and the corresponding data are listed in Table A.1.

The use of lubricant Krytox showed lower wear losses on both the nitrided and the oil-quenched samples compared with the use of lubricant Peerless LLG. The wear rate of nitrided sample was over one order of magnitude lower than that of previous lubricated wear test with lubricant Peerless LLG, and the wear rate of oil quenched sample was five times lower as well. It can be seen in Figure A.1, the wear loss increased rapidly during the early running-in stage and then grew steadily after 5000 m sliding distance at the steady-state stage. As mentioned previously, the wear rate of the oil quenched samples still lower than that of nitrided sample both at running-in stage and steady-state stage. The wear rates and the wear coefficients of the samples under different conditions were calculated and the results are listed in Table A.2. According to the results, it is obvious that the wear resistance of oil quenched sample showed enhanced wear resistance compared with the untreated, borided and nitrided samples at both dry and lubricated conditions.

The degree of wear can be clearly characterized by the scar outline of the wear track. Figures A.2 to A.3 show the 3-D profilometry images that combined with 2-D surface profiles of surface damage on the nitride and oil-quenched samples after lubricated sliding wear tests. In Peerless LLG lubricated wear tests, the width of wear track on these two specimens changed slightly and also the penetration depth of wear track became deeper with increasing the sliding distance. The nitrided samples showed the largest penetration depth around 4.74 μm at 15000 m sliding distance, while the oil quenched sample had the lowest penetration depth, 2.56 μm. It can be observed that the width of wear track did not

change significantly but the penetration depth kept growing on the nitrided sample, whereas on the oil-quenched sample the penetration depth stabilized at 2.5 µm after 10,000 m sliding distance in Krytox lubricated wear tests. The wear depth was plotted against the sliding distance and is shown in Figure A.4. At the same sliding distance, the samples with lubricant Krytox had lower penetration depths compared with those obtained in the wear tests using lubricant Peerless LLG.

The microstructure significantly affects the scratches characteristics of the worn surfaces. When the friction pairs pass through the surface of the sample, the steel was removed and leaving the wear track. The optical photographs of worn surfaces of the nitride and oil quenched samples tested at different sliding distances with Krytox are shown in Figures A.5 and A4.6. It can be seen that the morphologies of wear tracks changed slightly for both borided and nitrided samples with the increasing of the sliding distance, and the scratches on the surface were not as obvious as those observed after the wear tests using lubricant Peerless LLG.
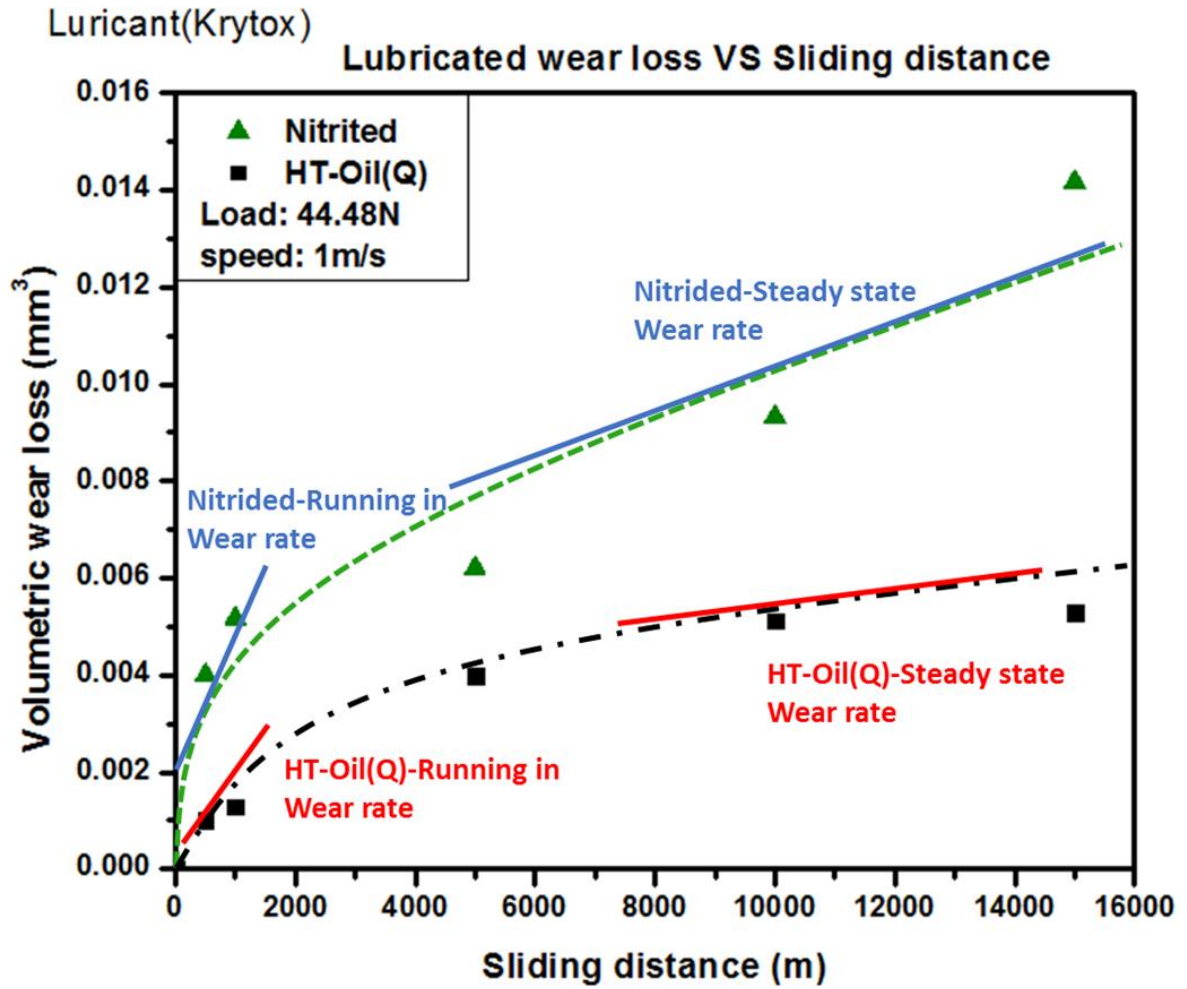
Figure A.1 Wear volumetric losses against sliding distance curves for nitrided and oil quenched 1045 steel under lubricated sliding tests with Krytox.

Table A.1 Summary of wear loss and penetration depth for nitrided and oil quenched 1045 steel after five sliding distance under lubricated sliding tests with Krytox.

Distance(m)	Krytox Lubricated Volumetric Wear loss (mm³)		Lubricated Wear Depth (µm)	
	HT-Oil (Q)	Nitride	HT-Oil (Q)	Nitride
500	1.01×10^{-3}	4.01×10^{-3}	0.712	1.736
1000	1.29×10^{-3}	5.18×10^{-3}	1.341	2.577
5000	3.99×10^{-3}	6.22×10^{-3}	1.817	2.628
10000	5.12×10^{-3}	9.34×10^{-3}	2.491	2.835
15000	5.29×10^{-3}	0.014	2.556	4.746

Table A.2 Summary of wear rate for nitrided and oil quenched 1045 steel after lubricated sliding tests with Krytox.

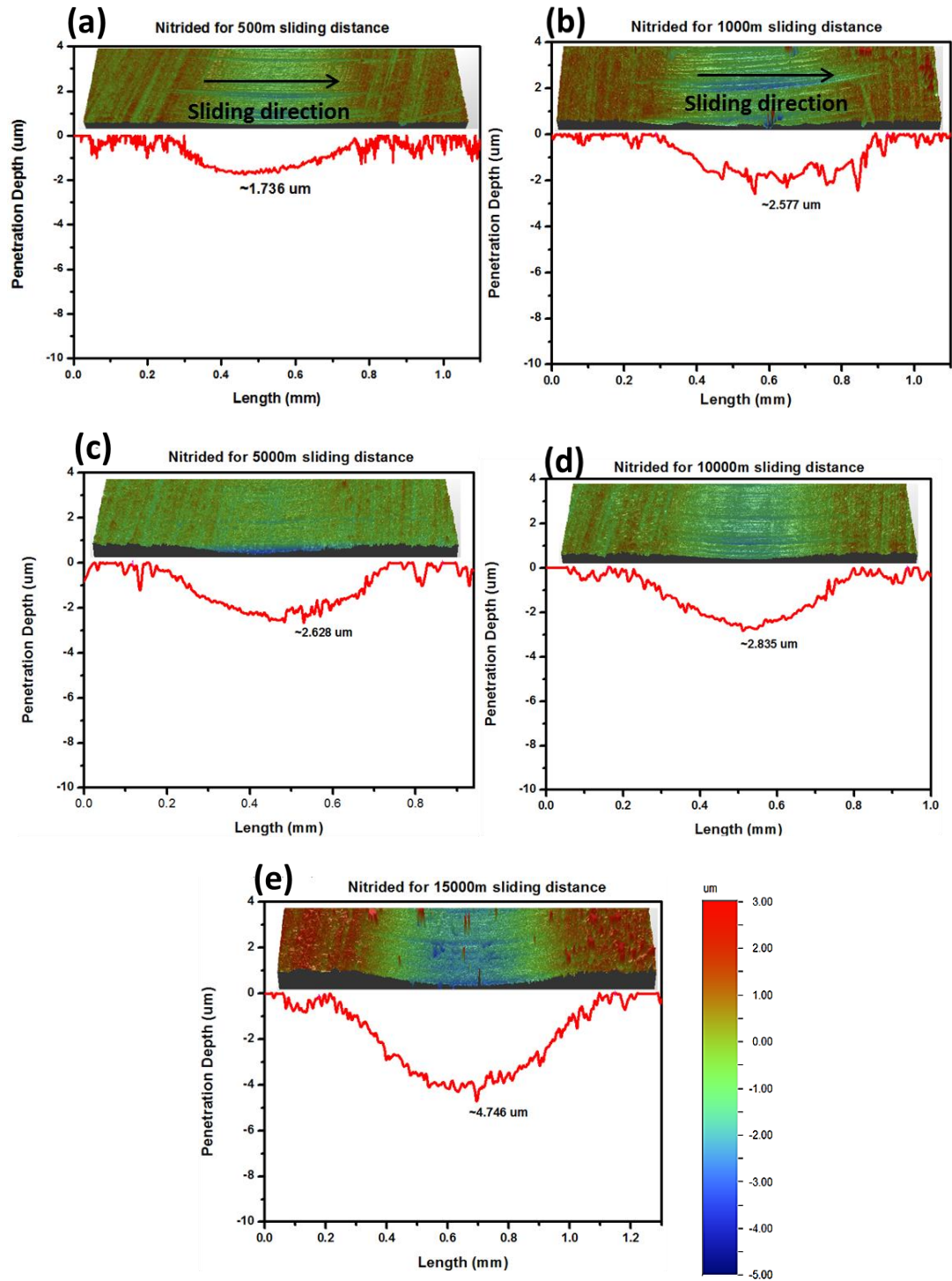| Sample condition	Surface Hardness		Lubricated Wear test(Krytox)	
			Wear Rate (mm³/m)	Wear rate Coefficient K
Nitrided	418.72 (HV)	4106 (Mpa)	(R) 5.75×10^{-6}	(R) 5.31×10^{-4}
			(S) 7.96×10^{-7}	(S) 7.35×10^{-5}
HT-Oil	520.73 (HV)	5109 (Mpa)	(R) 1.44×10^{-6}	(R) 1.62×10^{-4}
			(S) 1.30×10^{-7}	(S) 1.46×10^{-5}

Figure A.2 Lubricated wear penetration depth for nitrided AISI 1045 steel sample (Lubricant: Krytox) with different sliding distance, (a) 500 m, (b) 1000 m, (c) 5000 m, (d) 10000 m, (e) 150000 m.
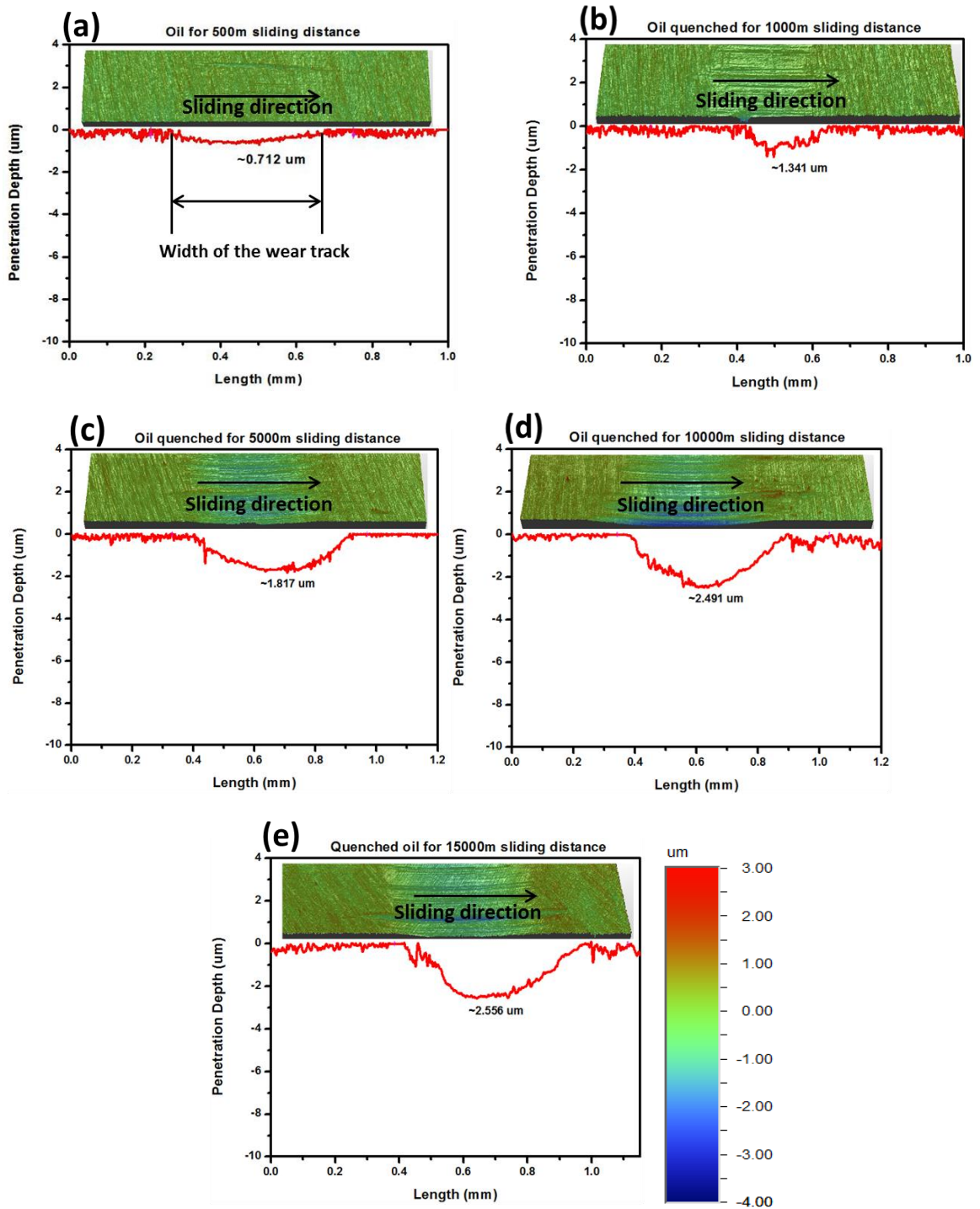
Figure A.3 Lubricated wear penetration depth for AISI 1045 steel quenched in oil at 160 °C (Lubricant: Krytox) with different sliding distance, (a) 500 m, (b) 1000 m, (c) 5000 m, (d) 10000 m, (e) 150000 m.
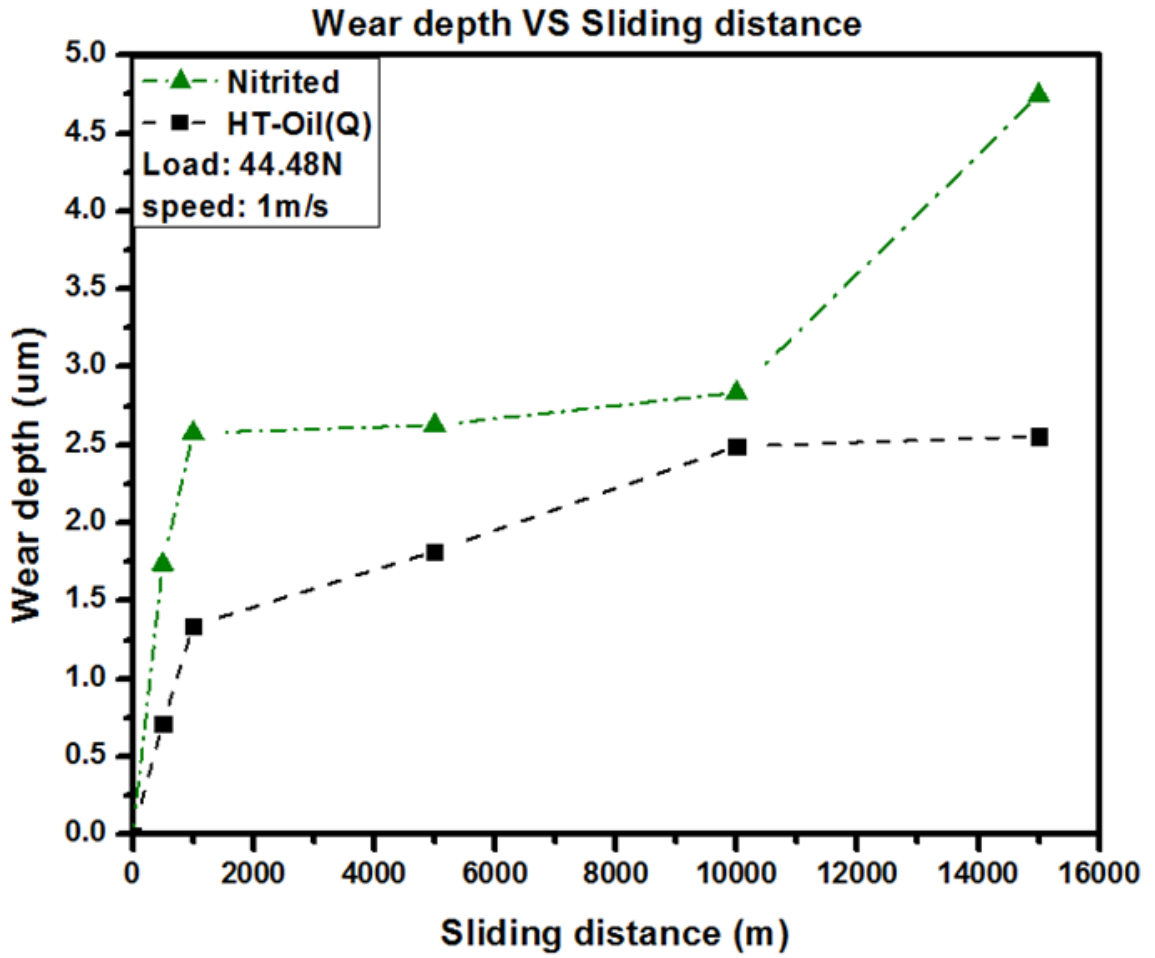
Figure A.4 Average lubricated wear penetration depth against sliding distance for nitrided and quenched in oil at 160 °C AISI 1045 steel sample at an applied load of 44.48 N with Krytox.
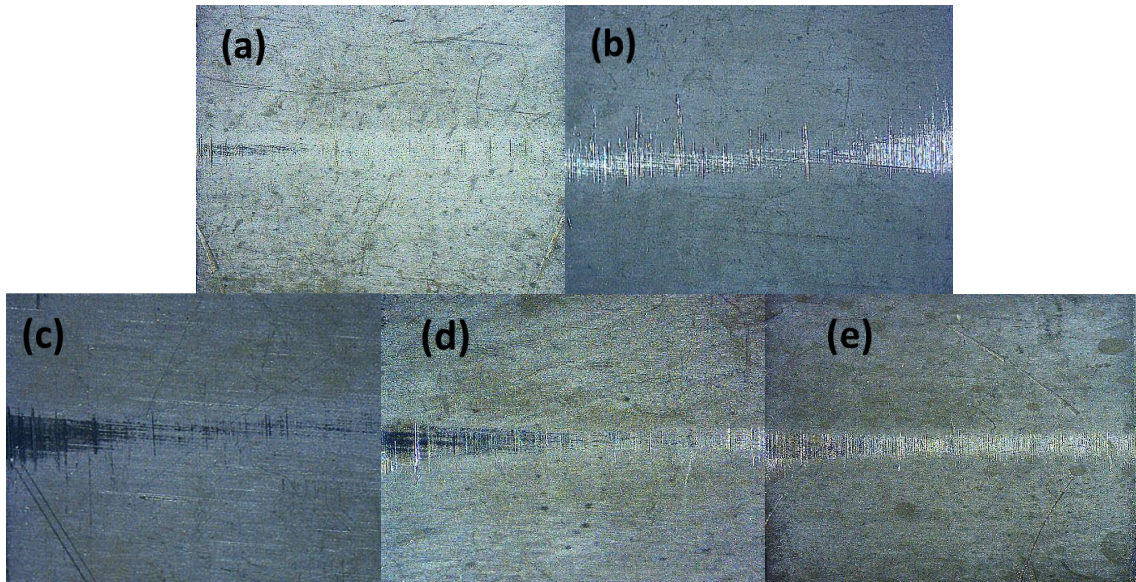
Figure A.5 Lubricated wear track of nitrided AISI 1045 steel sample with different sliding distance (Lubricant: Krytox), (a) 500m, (b) 1000m, (c) 5000m, (d) 10000m, (e) 150000m.
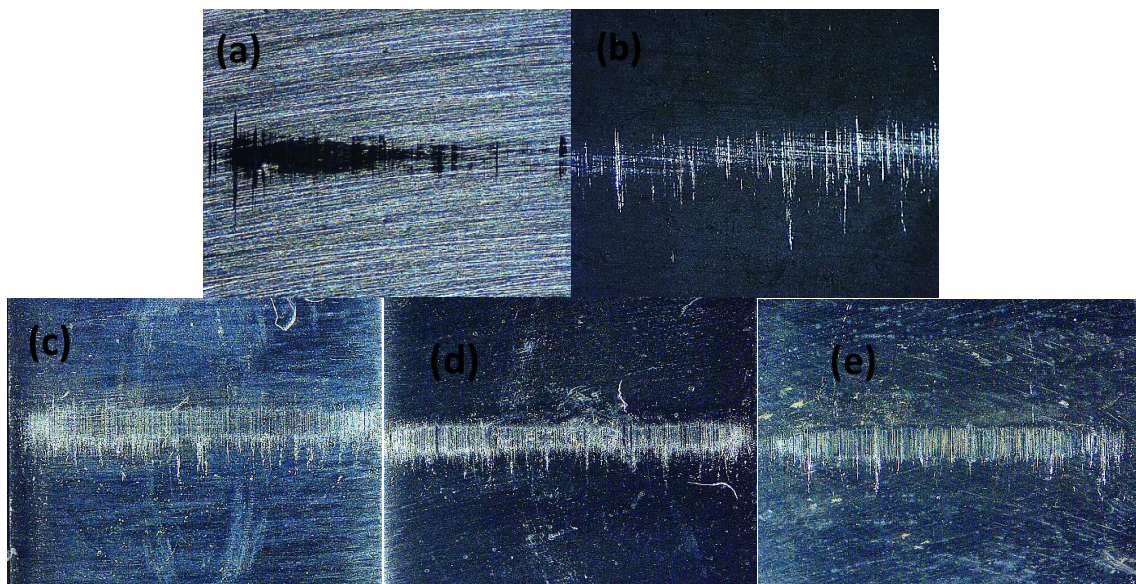

Figure A.6 Lubricated wear track of AISI 1045 steel sample quenched in oil at 160 °C with different sliding distance (Lubricant: Krytox), (a) 500m, (b) 1000m, (c) 5000m, (d) 10000m, (e) 150000m.

VITA AUCTORIS

NAME: Mingxiao Yang

PLACE OF BIRTH: Deyang, Sichuan, China

YEAR OF BIRTH: 1995

EDUCATION: Deyang No.5 High School, Deyang, Sichuan, China, 2013

Lanzhou University of Technology, B.E., Lanzhou, Gansu, China, 2017

University of Windsor, M.A.Sc., Windsor, ON, 2020